

Development of Terahertz Quantum-Cascade Lasers as Sources for Heterodyne Receivers

DISSERTATION

zur Erlangung des akademischen Grades

Doctor rerum naturalium (Dr. rer. nat.)
im Fach Physik

eingereicht an der
Mathematisch-Naturwissenschaftlichen Fakultät I
Humboldt-Universität

von

Dipl.-Phys. Martin Wienold

Präsident der Humboldt-Universität:

Prof. Dr. Jan-Hendrik Olbertz

Dekan der Mathematisch-Naturwissenschaftlichen Fakultät I:

Prof. Dr. Andreas Herrmann

Gutachter:

1. Prof. Dr. H. Riechert
2. Prof. Dr. W. T. Masselink
3. Prof. Dr. J. Faist

Tag der mündlichen Prüfung: 21.03.2012

Abstract

This thesis presents the development and optimization of terahertz quantum-cascade lasers (THz QCLs) as sources for heterodyne receivers. A particular focus is on single-mode emitters for the heterodyne detection of the important astronomic oxygen (OI) line at 4.75 THz. Various active-region designs are investigated. High-output-power THz QCLs with low operating voltages and emission around 3 THz are obtained for an active region, which involves phonon-assisted intersubband transitions. While these QCLs are based on a GaAs/Al_xGa_{1-x}As heterostructure with $x = 0.15$, similar heterostructures with $x = 0.25$ allowed for very low threshold current densities. By successive modifications of the active-region design, THz QCLs have been optimized toward the desired frequency at 4.75 THz. To obtain single-mode operation, first-order lateral distributed-feedback (DFB) gratings are investigated. It shows that such gratings allow for single-mode operation in combination with high continuous-wave (cw) output powers. A general method is presented to calculate the coupling coefficients of lateral gratings. In conjunction with this method, the lasers are well described by the coupled-mode theory of DFB lasers with two reflective end facets. Single-mode operation within the specified frequency bands at 4.75 THz is demonstrated. Stable operation of THz QCLs is often in conflict with the occurrence of a negative differential resistance (NDR) regime at elevated field strengths and the formation of electric-field domains (EFDs). Stationary EFDs are shown to be related to discontinuities in the cw light-current-voltage characteristics, while non-stationary EFDs are related to current self-oscillations and cause a temporal modulation of the output power. To model such effects, the nonlinear transport equations of weakly coupled superlattices are adopted for QCLs by introducing an effective drift velocity-field relation.

Zusammenfassung

Die vorliegende Arbeit beschäftigt sich mit der Entwicklung und Optimierung von Terahertz-Quantenkaskadenlasern (THz-QCLs) für die Anwendung als Lokaloszillator in THz-Heterodyndetektoren, insbesondere für die Detektion der astronomisch wichtigen Sauerstoff (OI) Linie bei 4.75 THz. Hierfür wurden zunächst unterschiedliche QCL-Heterostrukturen untersucht. Basierend auf einer Heterostruktur, welche schnelle Intersubbandübergänge über Streuung an Phononen ausnutzt, konnten QCLs mit hoher Ausgangsleistung und niedriger Betriebsspannung bei 3 THz erzielt werden. Während diese Laser auf dem Materialsystem GaAs/Al_xGa_{1-x}As mit $x = 0.15$ basieren, führt die Erhöhung des Al-Anteils auf $x = 0.25$ für ähnliche Strukturen zu sehr niedrigen Schwellstromdichten. Durch schrittweise Optimierungen gelang es, QCLs zu realisieren, die bei 4.75 THz emittieren. Mit Hilfe von lateralen Gittern erster Ordnung für die verteilte Rückkopplung (DFB) konnten Einzelmoden-Dauerstrichbetrieb mit hoher Ausgangsleistung, sowie Einzelmoden-Betrieb innerhalb des spezifizierten Frequenzbereichs bei 4.75 THz erzielt werden. Eine allgemeine Methode zur Bestimmung der DFB-Kopplungskonstanten erlaubt eine gute Beschreibung der Laser innerhalb der etablierten Theorie der gekoppelten Moden für DFB-Laser mit reflektiven Endfacetten. Oft steht das Auftreten negativer differentieller Leitfähigkeit bei höheren Feldstärken und die damit verbundenen Bildung von elektrischer Felddomänen (EFDs) im Konflikt mit einem stabilen Betrieb der THz-QCLs. Es wird gezeigt, dass stationäre EFDs mit Diskontinuitäten in der statischen Licht-Strom-Spannungskennlinie verbunden sind, während Selbstoszillationen, verursacht durch nicht-stationäre EFDs, eine zeitliche Modulation der Ausgangsleistung bewirken. Mit Hilfe einer effektiven Driftgeschwindigkeit für QCLs lassen sich viele der beobachteten Phänomene durch die nichtlinearen Transportgleichungen für schwach gekoppelte Übergitter beschreiben.

Contents

1	Introduction	1
2	Basic principles of THz QCLs	3
2.1	GaAs/(Al,Ga)As semiconductor heterostructures	3
2.2	Electronic states in planar heterostructures	4
2.3	Intersubband transitions	6
2.3.1	Optical intersubband transitions	6
2.3.2	Electronic transport	8
2.3.3	Miniband transport	9
2.4	Optical properties of GaAs and (Al,Ga)As in the THz range	10
2.5	Waveguides and resonators of THz QCLs	13
2.6	Basic concepts of the QCL active region	18
2.7	Intrinsic linewidth of QCLs	20
3	Design, fabrication and characterization	21
3.1	Heterostructure design	21
3.2	Epitaxial growth	23
3.3	Post-growth fabrication	24
3.4	Characterization	25
4	Low-voltage, high-power THz QCLs emitting around 3 THz	29
4.1	Active-region design and QCL characteristics	29
4.2	Influence of growth variations on the lasing characteristics	34
4.3	Conclusions	35
5	Low-threshold THz QCLs based on GaAs/Al_{0.25}Ga_{0.75}As heterostructures	37
5.1	Influence of the barrier composition on the electronic transport	37
5.2	Experimental results and discussion	39
5.3	Conclusions	42
6	THz QCLs for emission above 4 THz	45
6.1	Basic active-region design for emission above 4 THz	45
6.1.1	Experimental results of a doping series	47
6.1.2	Discussion	49
6.2	Design modifications	50
6.2.1	Impact of local modifications of the barrier thicknesses	51
6.2.2	Design modifications based on a double injection barrier	52
6.2.3	Design modifications based on a single injection barrier	53
6.3	Variation of the laser parameters across a wafer	55

Contents

6.4	Frequency trend of the operating temperature	57
7	THz QCLs with lateral distributed-feedback gratings	59
7.1	A brief survey of the coupled-mode theory of DFB lasers	60
7.2	Calculation of the coupling coefficients for lateral DFB gratings	62
7.3	Experimental results and discussion	65
7.4	Single-mode emission at specified target frequencies	69
7.5	Conclusions	70
8	Nonlinear transport effects related to electric-field domains in THz QCLs	73
8.1	Stationary electric-field domains	73
8.1.1	Experimental results	75
8.1.2	Modeling of QCLs in the presence of stationary EFDs	77
8.1.3	Discussion	80
8.2	Self-oscillations due to non-stationary electric-field domains	81
8.3	Conclusions	85
9	Summary and outlook	87
	Appendix: Nominal layer sequences	89
	Bibliography	91
	Publications	103
	Acknowledgement	105

Abbreviations

AR	active region
CBO	conduction band offset
<i>C-V</i>	capacitance-voltage
cw	continuous-wave
DFB	distributed feedback
EFD	electric-field domain
FTIR	Fourier transform infrared spectrometer
FWHM	full width at half maximum
IB	injection barrier
<i>I-V</i>	current-voltage
IDFB	lateral distributed feedback
<i>L-I-V</i>	light-current-voltage
LO	longitudinal optical
MBE	molecular beam epitaxy
MIR	mid infrared
MM	metal-metal
NDR	negative differential resistance
PDR	positive differential resistance
PE	polyethylene
QCL	quantum-cascade laser
SEM	scanning electron microscopy
SI	semi-insulating
SP	single-plasmon
TE	transverse electric
THz	terahertz
TM	transverse magnetic
TO	transverse optical

Frequently used symbols

c	speed of light in vacuum
d	period length of superlattice or active-region
d_0	nominal period length
e	electron charge
E	energy
\mathbf{E}	electric field vector
g	gain
\tilde{g}	differential gain
g_{peak}	peak gain
g_{th}	threshold gain
h	Planck's constant
\hbar	reduced Planck's constant
f_i	Fermi factor
f_{ij}	oscillator strength
F	average electric field strength
I	current
J	current density
J_{th}	threshold current density
J_{max}	current density at the output power maximum
\mathbf{k}	wavevector
k	imaginary part of the refractive index
k_B	Boltzmann's constant
K	index coupling coefficient
K_g	gain coupling coefficient
L	cavity or ridge length
m	electron mass
m_0	free electron mass
n	real part of the refractive index
$n_{2\text{D}}$	sheet carrier density
$n_{3\text{D}}$	volume carrier density
n_{dop}	sheet doping density
n_{eff}	effective refractive index
n_g	group refractive index
n_i	subband population
N_p	number of periods
n_r	bulk refractive index
P	optical power
P_{cw}	continuous-wave output power
P_{peak}	maximum output power divided by duty cycle
P_{pulse}	output power divided by duty cycle
R	reflectance
R_{th}	thermal resistance

T	temperature
T_{\max}	maximum operating temperature
T_0	characteristic temperature
v	forward drift velocity
v_d	effective drift velocity
V	voltage
V_c	conduction band offset
V_{el}	potential due to applied electrical bias
V_{op}	operating voltage
V_{th}	operating voltage at threshold
z_{ij}	dipole matrix element
α	absorption coefficient
α_m	mirror losses
α_w	waveguide losses
χ	dielectric susceptibility
Δ	miniband width
ε	dielectric function
ε_0	vacuum dielectric constant
ε_∞	high-frequency dielectric constant
η_i	injection efficiency
γ	damping parameter
γ_{IB}	inhomogeneous broadening parameter
γ_{ij}	FWHM width of transition
γ_c	nonparabolicity parameter
γ_E	energy-dependent scattering rate
Γ	confinement factor
Γ_p	confinement factor per period
Λ	grating period
λ_B	Bragg wavelength
ϕ_F	facet phase
ω	angular photon frequency
μ	effective electron mass in units of m_0
ν	photon frequency
ν_L	LO phonon frequency
ν_T	TO phonon frequency
ψ	envelope wavefunction
σ	transition cross-section
σ_c	contact conductance
σ_s	standard deviation
τ	scattering time
τ_i	total lifetime in subband i
τ_{ij}	transition lifetime

1 Introduction

Many spectroscopic and imaging applications in the terahertz (THz) or far-infrared range of the electromagnetic spectrum rely on artificial emission sources with suitable properties. Such an application in the field of astronomy is the heterodyne spectroscopy of the emission of cold interstellar gases. Examples for particular important emission lines are the fine-structure transitions of molecular deuterated hydrogen at 2.68 THz and neutral atomic oxygen (OI) at 4.75 THz, where the latter is believed to be one major coolant channel of the interstellar medium. Heterodyne detection requires local oscillators, which emit within a few GHz of the particular transition frequency. Promising sources for local oscillators above 2 THz are THz quantum-cascade lasers (QCLs), which are electrically driven semiconductor lasers based on intersubband transitions. The first proposals for such intersubband lasers reach back to the 1970's [1]. However, an intersubband laser was not demonstrated until 1994 [2]. The first intersubband laser, named quantum-cascade laser by its inventors, operated at 4.3 μm and started the development of mid-infrared (MIR) QCLs, which emit at frequencies above the phonon absorption band of the semiconductor. Another eight years later, in 2002, the first QCL operating below the phonon absorption band was demonstrated [3], starting the development of THz QCLs.

In contrast to interband semiconductor lasers, in which electron-hole pairs recombine radiatively, QCLs are unipolar devices based on intersubband transitions in the conduction band. In such a laser, a quantum-well heterostructure provides a well-defined confinement for the electrons, and, by a proper design of this structure, a population inversion between two subband states can be achieved. Due to the absence of recombination, the number of electrons is a conserved quantity in QCLs, and a single electron can undergo several lasing transitions in a vertically stacked cascade of active-region periods. Note that in this work the term *active-region period* refers to a single period of the QCL heterostructure, while the term *active region* refers to the sum of all periods. The emission frequency of a QCL is determined by the design of the active-region period and independent of the semiconductor bandgap. Both types, MIR and THz QCLs, rely on the same principle of operation. However, the waveguides, which confine the optical mode, are different for THz and MIR QCLs due to the different wavelength ranges.

In contrast to MIR QCLs, which operate today mostly at room temperature or above, the operation of THz QCLs is restricted to temperatures below 200 K. This imposes a severe challenge for any application, since the laser has to be integrated in a cryogenic operation environment. Since the size and cost of such a cooling system scale with the thermal power, which has to be dissipated at low temperatures, a small electrical driving power of the THz QCL is of major importance. In recent years, many record values for particular properties of THz QCLs have been reported, such as the highest temperature for pulsed operation [4], the highest output power [5], and the lowest operating frequency [6]. The focus of the present work is on the development of THz QCLs, which combine

1 Introduction

several beneficial properties in order to be suitable as local oscillators for THz heterodyne spectroscopy and further applications. Ideally, a THz QCL for use as local oscillator operates with mW optical power in continuous-wave (cw) mode, a Gaussian beam profile, and a single-mode emission spectrum. Heterodyne receivers based on THz QCLs as local oscillators have been proposed and also demonstrated within the recent years [7, 8, 9, 10, 11, 12]. However, the realization of heterodyne detectors based on THz QCLs for astronomically important emission lines such as the OI line at 4.75 THz has remained an open challenge.

Another aim of this work is a better understanding of the nonlinear transport effects in THz QCLs, which are related to the presence of negative differential resistance (NDR) and the formation of electric-field domains (EFDs). These effects are important since they are usually in conflict with a stable operation of THz QCLs. It shows that the observed phenomena are very similar to those found for semiconductor superlattices including discontinuities in the current-voltage characteristics and current self-oscillations. For weakly coupled superlattices, the different nonlinear transport phenomena are covered by a set of nonlinear transport equations describing the system. In this work, these equations are adopted for THz QCLs by introducing an effective drift velocity.

In the following chapter, the basic principles of THz QCLs are discussed. The used fabrication and characterization techniques are explained in Chapter 3. Chapters 4 discusses THz QCLs based on a GaAs/Al_{0.15}Ga_{0.85}As active-region heterostructure for emission around 3 THz. Chapter 5 deals with low-threshold THz QCLs based on GaAs/Al_{0.25}Ga_{0.75}As heterostructures. Results on the development of THz QCLs for emission above 4 THz are summarized in Chapter 6. Chapter 7 is about THz QCLs with lateral distributed feedback (DFB) gratings for single-mode, continuous-wave operation in combination with high output powers. Chapter 8 discusses nonlinear transport effects, which are related to electric-field domains, and Chapter 9 summarizes the thesis.

2 Basic principles of THz QCLs

In this chapter, basic principles of THz QCLs are discussed. Starting with the semiconductor heterostructures, aspects of the involved intersubband physics, the optical properties of semiconductors in the THz range, THz waveguides, and basic concepts of the active-region design are presented.

2.1 GaAs/(Al,Ga)As semiconductor heterostructures

The vast majority of THz QCLs, including those investigated in this work, are based on planar GaAs/(Al,Ga)As heterostructures grown on GaAs substrates. Due to the rather small lattice mismatch of $\text{Al}_x\text{Ga}_{1-x}\text{As}$ with respect to GaAs, the barrier height, which is determined by the Al content x , is a degree of freedom in this system. GaAs-based THz QCLs benefit further from the well-understood, high-quality planar growth of GaAs/(Al,Ga)As and the availability of semi-insulating substrates, which are highly transparent in the far-infrared spectral region. Other III-V heterosystems grown on InP substrates have been proposed such as lattice-matched (In,Ga)As/(In,Al)As [13, 14] and (In,Ga)As/ Ga(As,Sb) [15]. However, no significant improvements as compared to GaAs-based THz QCLs have been obtained.

For GaAs/ $\text{Al}_x\text{Ga}_{1-x}\text{As}$ heterostructures, the barrier height for electrons equals the conduction band offset (CBO) at the Γ point for values of $x < 0.4$, while for values $x > 0.4$ the barrier height is determined by the smaller CBO of the indirect X and L valleys. Due to this Γ -(X,L) crossing, the maximum Al content for GaAs-based MIR QCLs is usually set to $x = 0.4$. The CBO can be calculated by the difference in the bandgaps of the two materials and the splitting ratio between valence and conduction band offsets. According to the review of Vurgaftman *et al.* [16], the following formula for the CBO at the Γ point has been used throughout this work:

$$\Delta E_c(x) = (1.109x - 0.934x^2 + 0.851x^3) \text{ eV} . \quad (2.1)$$

This relation is obtained for the bandgap parameters at $T = 0$ K including the bowing parameters for the ternary alloy and a splitting ratio of 35:65 between valence and conduction band offset.

Related to the requirement of a low-loss THz waveguide, the thickness of the active region for THz QCLs is usually at least 10 μm . This practically limits the average Al content, which can be used without exceeding the critical thickness for strain relaxation. For an estimate of this limit, the active-region heterostructure is considered as a single $\text{Al}_x\text{Ga}_{1-x}\text{As}$ layer with the average Al content of the heterostructure. Figure 2.1 depicts the critical thickness $h_c(x)$ for the formation of misfit dislocation in such a layer according to the theory of Matthews and Blakeslee [17]. Since the difference between the lattice constants of GaAs and AlAs decreases with increasing temperature [16], h_c is significantly

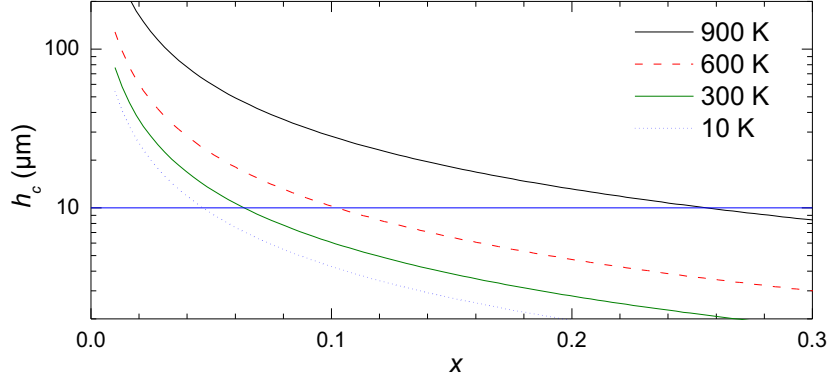


Figure 2.1: Dependence of the critical thickness h_c on the Al content of an $\text{Al}_x\text{Ga}_{1-x}\text{As}$ layer on GaAs for different substrate temperatures according to Ref. [17]. The horizontal line indicates a typical active-region thickness of 10 μm .

larger at the usual growth temperature of about 900 K as compared to room temperature. The average Al content is typically around 2% for the THz QCLs investigated in this work, for which the usual active-region thickness of 10–11 μm is well below h_c . However, in the case of optically pumped THz emitters such as the one proposed by Waldmueller *et al.*[18], the average Al content is significantly larger [19]. It has been found during this work that GaAs/ $\text{Al}_x\text{Ga}_{1-x}\text{As}$ heterostructures can be grown with a thickness of 11 μm and an average Al content of 8% without detectable relaxation. According to Fig. 2.1, this thickness is still below h_c for a growth temperature of 900 K but already above h_c at 300 K. While misfit dislocations might be energetically preferable, their formation requires an activation energy, which is not present at low temperatures.

2.2 Electronic states in planar heterostructures

QCLs are based on planar heterostructures, in which the electrons are confined in the growth direction by quantum wells. The electronic dispersion of the bulk crystal splits into subbands, which are characterized by discrete energy levels in the growth direction and a free-electron dispersion in the plane of the quantum wells.

In the envelope function approximation, the wavefunctions are separated into a rapidly varying Bloch term related to the Hamiltonian of the bulk crystal and a slowly varying envelope function $\Psi(\mathbf{r})$, which is governed by the heterostructure [20]. Due to the in-plane translation symmetry, the envelope function can be further separated as $\Psi(\mathbf{r}) = \psi_{xy}\psi_z$ with the in-plane component ψ_{xy} being a plane wave $\psi_{xy} \sim \exp[i(k_x x + k_y y)]$. If only conduction band states are considered, the z -component of the envelope function has to satisfy the following Schrödinger equation

$$\left(-\frac{\hbar^2}{2m_0} \frac{\partial}{\partial z} \frac{1}{\mu(z)} \frac{\partial}{\partial z} + V_c(z) + V_{\text{el}}(z) \right) \psi_z = E\psi_z. \quad (2.2)$$

2.2 Electronic states in planar heterostructures

Here, m_0 denotes the free electron mass, $V_c(z)$ the conduction band offset, $V_{\text{el}}(z)$ the electrical potential due to an applied electric field, and E the energy. The bulk dispersion of the layer materials enters as an effective electron mass $\mu(z)$ in units of m_0 (the electron mass in SI units is given by $m = \mu m_0$). In the case of a parabolic band, the effective mass does not depend on energy, and Eq. (2.2) has the form of an eigenvalue equation. However, a parabolic dispersion is only a good approximation close to the Γ -point of the Brillouin zone. The nonparabolicity of the bulk dispersion can be taken into account by an energy-dependent effective electron mass

$$\mu(E) = \mu_0 + \gamma_c E \quad (2.3)$$

with μ_0 denoting the effective electron mass at the Γ point and γ_c the nonparabolicity parameter. In this case, an eigenvalue problem is obtained for a quasi two-band $\mathbf{k}\cdot\mathbf{p}$ approach for the envelope function [21, 22]:

$$\begin{pmatrix} V_c(z) + V_{\text{el}}(z) & \frac{i\hbar}{\sqrt{2m_0\gamma_c}} \frac{\partial}{\partial z} \\ \frac{i\hbar}{\sqrt{2m_0\gamma_c}} \frac{\partial}{\partial z} & -\mu_0(z)/\gamma_c + V_{\text{el}}(z) \end{pmatrix} \begin{pmatrix} \psi_1(z) \\ \psi_2(z) \end{pmatrix} = E \begin{pmatrix} \psi_1(z) \\ \psi_2(z) \end{pmatrix}. \quad (2.4)$$

The two bands involved are the conduction band and a pseudo valence band, which does not have a direct physical equivalent, since the bandgap is determined by the external parameter γ_c (for $\gamma_c \rightarrow 0$, the two bands decouple and a parabolic dispersion is obtained for both). The envelope states are found by diagonalizing the resulting Hamiltonian matrix for given discrete potential distributions V_c and V_{el} and a discrete representation of the momentum operator $-i\hbar\partial/\partial z$.

If the carrier concentration is negligible, the electric field $\partial V_{\text{el}}/\partial z$ is constant and determined by the applied bias and the thickness of the structure. In case of periodic structures such as QCLs, wavefunctions with the center of mass in consecutive periods have to obey a translation symmetry similar to the Wannier-Stark states of a superlattice. If $\psi_i^{(k)}$ is the set of wavefunctions with the center of mass in period i , the condition becomes

$$\psi_i^{(k)}(z) = \psi_{i+1}^{(k)}(z + d), \quad (2.5)$$

with energy eigenvalues

$$E_{i+1}^{(k)} = E_i^{(k)} + Fd, \quad (2.6)$$

where F denotes the average electric-field strength and d the period length. This symmetry, called periodic voltage drop (PVD) in the following, facilitates the simulation of QCL structures, since only few periods (typically 3–4) have to be taken into account. The PVD condition is usually considered to be valid also for the case of a local screening of the electric field by mobile carriers, resulting in a dipole formation in each period. In this case, the Schrödinger equation has to be solved self-consistently together with the Poisson equation and a model of the electronic transport, and F becomes in general different from the local field strength $\partial V_{\text{el}}/\partial z$. While this approach yields often reasonable results, it fails in the case of non-periodic space charge distributions, i.e. if charge accumulation and depletion regions are located in different periods of the structure. This subject is further discussed in Chapter 8.

2.3 Intersubband transitions

Intersubband transitions in the conduction band of planar heterostructures are the basis for devices such as quantum-well infrared detectors (QWIPs) and QCLs. Besides optical intersubband transitions, non-optical transitions play a major role for the electronic transport.

2.3.1 Optical intersubband transitions

In the following, the (linear) interaction of photons with subband states is discussed in order to derive expressions for the transition cross-section and the optical gain (for a detailed derivation see Ref. [23]). Assuming that the envelope function can be separated as $\psi(\mathbf{r}) = \psi_{xy}\psi_z$ with the in-plane component ψ_{xy} , the matrix element for two states ψ and ψ' is given by

$$M = \langle \psi' | H_{\text{rad}} | \psi \rangle = \langle \psi'_z | H_{\text{rad}} | \psi_z \rangle \delta_{k_{xy}k'_{xy}} \quad (2.7)$$

with H_{rad} denoting the interaction Hamiltonian with the radiation field. For a non-vanishing matrix element, the in-plane momenta of the envelope functions have to be equal ($\delta_{k_{xy}k'_{xy}} = 1$). This is due to the polarization selection rule for intersubband transitions: only photons polarized perpendicular to the xy -plane, i.e. p -polarized photons, cause intersubband transitions [21]. The matrix element can be written as

$$M = e \left(\frac{\phi \hbar \omega}{2 \varepsilon_0 n_r c} \right)^{1/2} \sin(\theta_p) \langle \psi'_z | z | \psi_z \rangle \delta_{k_{xy}k'_{xy}}, \quad (2.8)$$

where e denotes the electron charge, ϕ the photon flux, $\hbar\omega$ the photon energy, n_r the refractive index, c the speed of light, ε_0 the vacuum dielectric constant, θ_p the angle between the electric-field vector and the xy -plane, and $\langle \psi'_z | z | \psi_z \rangle$ the dipole matrix element. Using Fermi's golden rule

$$W(\hbar\omega) = \frac{2\pi}{\hbar} \sum_{i,j} |M|^2 (f_i - f_j) \delta(E_j - E_i - \hbar\omega), \quad (2.9)$$

the total transition rate $W(\hbar\omega)$ is obtained by summing over all initial and final states, where f_i , f_j , E_i , and E_j are the Fermi factors and energies for the initial (i) and final (j) states, respectively. The corresponding transition cross-section is given by $\sigma = W/\phi$, and the absorption/gain coefficient α in units of the inverse length is given by $\alpha = \sigma n_{3D}$ with n_{3D} being the volume carrier density. In the case of a partially confined waveguide mode, α has to be multiplied with the confinement factor Γ , which determines the overlap of the optical mode with the transition. For a finite broadening, the δ -function becomes a Lorentzian:

$$\delta(E_i - E_j - \hbar\omega) \rightarrow \frac{1}{\pi} \frac{(\gamma_{ij}/2)}{(\hbar\omega - \hbar\omega_{ij})^2 + (\gamma_{ij}/2)^2}, \quad (2.10)$$

where γ_{ij} denotes the full width at half maximum (FWHM) of the transition and $\hbar\omega_{ij}$ the transition energy. Considering only a single intersubband transition, the absorption

coefficient is given by

$$\alpha = \sigma n_{3D} = \frac{e^2 \omega}{\varepsilon_0 n_r c} \sin^2(\theta_p) |z_{ij}|^2 (f_i - f_j) n_{3D} \frac{(\gamma_{ij}/2)}{(\hbar\omega - \hbar\omega_{ij})^2 + (\gamma_{ij}/2)^2} \quad (2.11)$$

with the dipole matrix element $z_{ij} = \langle \psi_j | z | \psi_i \rangle$. z_{ij} is related to the oscillator strength f_{ij} via $f_{ij} = (2m\omega/\hbar) |z_{ij}|^2$. f_{ij} fulfills the sum rule $\sum_j f_{ij} = 1$. In the limit of weak absorption and for low temperatures, the Fermi factors become $f_i = 1$ and $f_j = 0$, and the absorption efficiency can be written as $\eta = \alpha l$, where l is the interaction length, i.e. the length the light passes within the quantum well. In the case of oblique incidence, the result becomes

$$\eta = \frac{e^2 \omega}{\varepsilon_0 n_r c} \frac{\sin^2(\theta_p)}{\cos(\theta_p)} |z_{ij}|^2 n_{2D} \frac{(\gamma_{ij}/2)}{(\hbar\omega - \hbar\omega_{ij})^2 + (\gamma_{ij}/2)^2} \quad (2.12)$$

with n_{2D} denoting the sheet carrier density. Equations (2.11) and (2.12) are useful to estimate for instance the pumping efficiency of optically pumped intersubband emitters for different coupling geometries. Such an emitter has been proposed by Waldmueller *et al.*, who suggested the generation of THz radiation by exploiting an external MIR pump laser *et al.* [18]. In their proposal, the MIR pump field is resonantly coupled to an MIR intersubband transition. According to Eqs. (2.11) and (2.12), the pumping efficiency scales with the square of the dipole matrix element and the inverse of the transition broadening γ_{ij} of the MIR intersubband transition. However, the realization of such a structure has proven challenging due to the presence of negative differential resistance and the formation of electric-field domains [19].

According to Eq. 2.11, intersubband gain occurs for a population inversion between two subbands ($f_j > f_i$). In a QCL, this is achieved by electrical pumping. Assuming that the populations of the upper and lower laser level are n_3 and n_2 , respectively, the gain maximum ($E_{32} = \hbar\omega$) for p -polarized light ($\theta_p = 90^\circ$) becomes

$$g_{\text{peak}} = \frac{e^2 \omega}{\varepsilon_0 n_r c} \frac{|z_{32}|^2}{\gamma_{32}/2} (n_3 - n_2). \quad (2.13)$$

The dipole matrix element z_{32} and the population of the laser levels depend on the field strength and the design of the particular heterostructure.

Due to the Kramers-Kronig relation, not only the imaginary, but also the real part of the dielectric function is affected by the presence of intersubband transitions. The imaginary part of the linear dielectric susceptibility $\chi = \chi_1 + i\chi_2$ is given by

$$\chi_2 = n_r \frac{c\alpha}{\omega}, \quad (2.14)$$

where χ_1 and χ_2 are connected by the Kramers-Kronig relation — if the imaginary parts of two susceptibility functions are equal, also the real parts equal each other. With the approximation $2\omega(\omega - \omega_{ij}) \approx \omega^2 + \omega_{ij}^2$ in Eq. (2.11), which is reasonable for small broadening parameters, χ_2 (and hence also χ_1) become that of a classical damped oscillator. In analogy to a classical ensemble of oscillators with a low density, i.e. if the electric field is not significantly screened by the dipoles, the intersubband susceptibility for multiple transitions can be written as

$$\chi_{\text{ISB}} = \frac{n_{3\text{D}}}{\varepsilon_0} \sum_{ij} \alpha_{ij}^P (f_i - f_j), \quad (2.15)$$

where the microscopic polarizability α_{ij}^P caused by the transition $i - j$ is given by

$$\alpha_{ij}^P = \frac{e^2}{m} \frac{f_{ij}}{\omega_{ij}^2 - \omega^2 - i\gamma_{ij}\omega} = \frac{2e^2}{\hbar} \frac{|z_{ij}|^2 \omega}{\omega_{ij}^2 - \omega^2 - i\gamma_{ij}\omega}. \quad (2.16)$$

Eventually, the dielectric function is given by $\varepsilon = 1 + \chi_{\text{bg}} + \chi_{\text{ISB}}$, where χ_{bg} subsumes other contributions to the linear susceptibility such as phonon and interband terms.

A quantum mechanical derivation of the linear susceptibility within the framework of semiconductor Bloch equations can be found in Ref. [24]. Having a slightly different mathematic form, the results are quantitatively very similar to Eq. (2.15).

2.3.2 Electronic transport

Electrically driven intersubband devices such as QCLs are governed by electronic inter- and intrasubband transport. In contrast to the previously discussed photon-assisted dipole transitions, the treatment of non-optical intersubband scattering can be rather complex. Various approaches with different levels of approximation exist to deal with this issue. The simplest approach, and the one which allows for analytic results, is to assume constant scattering times and solve a rate equation system for the population of the different subbands [25]. In principle, the scattering times can be obtained by Fermi's golden rule for a particular set of subband wavefunctions and a particular in-plane carrier distribution. However, the wavefunctions in a QCL change with field strength and so do the scattering times. This restricts the validity of constant-scattering-time approaches to small intervals of interest such as around the lasing threshold of the QCL. For the purpose of a full device transport simulation, the scattering times have to be calculated self-consistently with the field distribution and the wavefunctions for a certain applied bias.

The electronic transport in intersubband devices is affected by inelastic and elastic scattering [26]. Inelastic scattering includes scattering on acoustic and optical phonons as well as electron-electron scattering. While the latter is an elastic process in a strict sense, it can be treated as an effective inelastic scattering process in a one-particle picture (Hartree approximation). Elastic scattering includes scattering on impurities and interface roughness and is connected to a dephasing of the electronic wavefunctions. It has been shown that this effect can play a role for resonant tunneling of electrons from the injector into the upper laser level of the QCL [27]. Since dephasing is a many-particle effect, a consistent treatment requires a many-particle picture. Dephasing is often treated within a density matrix approach assuming constant scattering times [27, 28].

The non-equilibrium Green's function theory (NEGF) [29, 30] provides in principle a consistent method to calculate the full inter- and intrasubband quantum transport, but at the cost of a huge computational time. Until now, only simple structures have been calculated with this method. The numerical expense of including quantum coherence and dephasing in transport simulations can be understood by the $N^2 \times N^2$ nature of the Liouville equation for the density matrix, i.e., the numerical expense scales with the fourth power of the number N of subbands, which are considered.

For the numerical simulations in this work, a rather simple rate-equation model is applied, assuming energy-dependent, but momentum-independent scattering rates [22]. This allows for a fast, self-consistent solution of the Schrödinger and Poisson equations without additional external parameters such as particular scattering rates.

2.3.3 Miniband transport

In the presence of many strongly coupled subbands, the electronic transport might be treated in the limit of miniband transport, characterized by a continuous dispersion along the growth direction within each miniband. In the tight-binding limit, the dispersion relation for the lowest miniband of a superlattice becomes [31]

$$E(\mathbf{k}) = \frac{\hbar^2 k_{xy}^2}{2m} + \frac{\Delta}{2}(1 - \cos[k_z d]). \quad (2.17)$$

The first term is related to the free in-plane electron motion, while the second term is related to the electron confinement in the growth direction. The parameters are Δ , denoting the width of the miniband (at zero bias), and d , denoting the superlattice period. Analytic expressions for the miniband transport in the relaxation time approximation, which are derived within a density matrix approach, can be found in Refs. [31, 32]. Assuming that only the lowest miniband is populated, the scattering-induced intraminiband current density becomes [31]

$$J = \frac{en_{2D}\Delta}{2\hbar\tau} \frac{\Omega_B}{\Omega_B^2 + 1/\tau^2} \frac{I_1[\Delta/(2k_B T)]}{I_0[\Delta/(2k_B T)]}, \quad (2.18)$$

where τ denotes the intraminiband relaxation time, $\Omega_B = eFd/\hbar$ the Bloch frequency of the superlattice, and k_B Boltzmann's constant. I_1 and I_0 are the modified Bessel functions of first and zeroth order, respectively. For low temperatures ($k_B T \ll \Delta$), the current density depends linearly on the miniband width ($J \sim \Delta$), while in the high temperature limit ($k_B T \gg \Delta$), a quadratic dependence ($J \sim \Delta^2$) is found. Note that the temperature enters Eq. (2.18) only via the distribution function for the electrons. In case of many QCLs, strongly coupled subbands form a *so-called* extraction/injection quasi-miniband, which connects consecutive optical transition regions. As a consequence of the strong dependence of the current density on Δ for miniband transport, the width of such a quasi-miniband has to be sufficiently large to avoid transport bottlenecks.

2.4 Optical properties of GaAs and (Al,Ga)As in the THz range

The optical properties of bulk III-V semiconductors in the THz range are determined by the interaction of photons with shallow impurities, free carriers, and phonons [33]. The latter cause the phonon absorption or reststrahlen band between about 6.5 and 10 THz in GaAs. Below the phonon absorption band and in the absence of dopants, semiconductors such as semi-insulating GaAs (SI GaAs) become highly transparent. Considering phonons and free carriers, the dielectric function can be expressed as a sum of the different contributions to the (linear) susceptibility and the high-frequency dielectric constant ε_∞ :

$$\varepsilon = (n + ik)^2 = 1 + \chi_\infty + \chi_{\text{phonon}} + \chi_{\text{FC}}. \quad (2.19)$$

Here, χ_{phonon} and χ_{FC} denote the susceptibility terms caused by phonons and free carriers, respectively, and $\chi_\infty = \varepsilon_\infty - 1$ subsumes the high-frequency terms such as interband contributions, which are treated to be constant in the THz range. The phonon term for GaAs can be approximated by an oscillator model of the form [33, 34]

$$\chi_{\text{phonon}}(\nu) = \varepsilon_\infty \frac{\nu_L^2 - \nu_T^2}{\nu_T^2 - \nu^2 - i\gamma\nu} \quad (2.20)$$

with the parameters ν_L and ν_T denoting the longitudinal optical (LO) and transverse optical (TO) phonon frequencies, respectively, and γ the damping parameter. In the case of an $\text{Al}_x\text{Ga}_{1-x}\text{As}$ alloy, GaAs- and AlAs-like phonons contribute to the dielectric function. The full dielectric function in this case has been discussed in Ref. [35]. For small Al contents, the change of the dielectric function is mainly caused by the change of $\varepsilon_\infty(x)$, and Eq. (2.20) can still be applied using $\varepsilon_\infty(x) = \varepsilon_\infty(\text{GaAs}) - ax$ with a proportionality coefficient a .

The phonon frequencies and the damping parameter of the oscillator term depend also on temperature. The measured transmittance spectra of a semi-insulating GaAs substrate, exhibit a temperature dependence between 150 K and room temperature, while below 100 K no significant dependence on temperature is found. Hence, to a good approximation, temperature-independent parameters can be used for the oscillator model at low temperatures. The parameters used in this work for the oscillator term of the dielectric function of $\text{Al}_x\text{Ga}_{1-x}\text{As}$ are summarized in Tab. 2.1. A calculation based on the low-temperature parameters is compared to a measured transmittance spectrum of a semi-insulating GaAs substrate in Fig. 2.2. A good quantitative agreement is found for frequencies below the phonon absorption band. The deviations in amplitude at higher

	ε_∞	ν_L (cm ⁻¹)	ν_T (cm ⁻¹)	γ (cm ⁻¹)
$T = 300$ K	$10.89 - 2.77x$	292.1	268.7	2.4
$T \leq 100$ K	$10.69 - 2.66x$	293.8	271.2	0.7

Table 2.1: Parameters used for the oscillator term of the dielectric function of GaAs and $\text{Al}_x\text{Ga}_{1-x}\text{As}$ at 300 K and at low temperatures [34, 36]. The values for ν_L and ν_T correspond to GaAs.

2.4 Optical properties of GaAs and (Al,Ga)As in the THz range

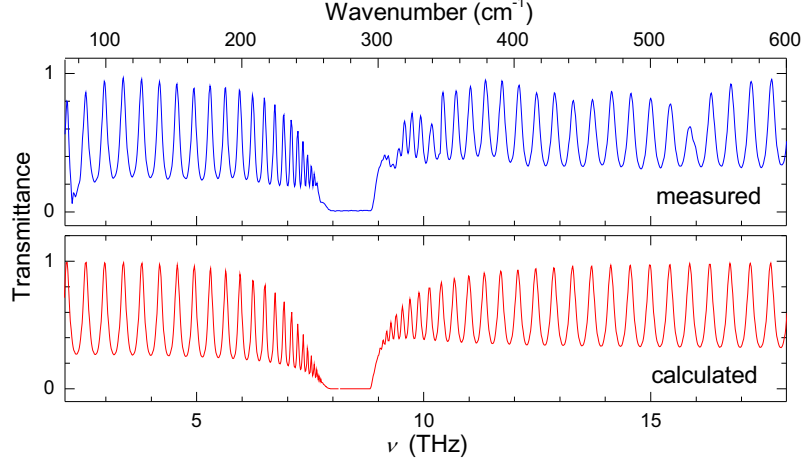


Figure 2.2: Measured and calculated far-infrared transmittance spectra for a 100 μm thick semi-insulating GaAs substrate at 10 K. The calculation is based on the transfer matrix method as described in Ref. [37].

frequencies are related to two-phonon absorption, which is not covered by the simple oscillator model.

The contribution of free-carrier absorption to the dielectric function below the phonon absorption band can be described by a plasma term [33]. In the parabolic-band approximation (Drude model), χ_{FC} is given by

$$\chi_{\text{FC}}(\omega) = -\frac{e^2 n_{3\text{D}}}{\epsilon_0 m(\omega^2 + i\omega/\tau)} \quad (2.21)$$

with $n_{3\text{D}}$ denoting the density of mobile carriers, τ the mean scattering time for electrons, and $\omega = 2\pi\nu$ the angular frequency.

Figure 2.3 shows the calculated absorption coefficient $\alpha = 4\pi\text{Im}(\sqrt{\epsilon})\nu$ of GaAs for different doping densities in the range 1.5–6 THz (50–200 cm^{-1}). The assumed Drude scattering time is 0.1 ps, the same as used in Ref. [38]. Except for undoped GaAs, the absorption and dielectric function are strongly affected by free-carrier absorption. Depending on $n_{3\text{D}}$, α ranges over several orders of magnitude. The strong dependence of the dielectric function on the doping density is exploited in single-plasmon THz QCLs, for which the optical mode is confined in the vertical direction by the top contact metal and a highly doped GaAs layer underneath the active region. In such a highly doped layer, the optical properties are determined by the mobile carriers.

Figure 2.4 depicts the real and imaginary part of the dielectric function and the refractive index for highly n -doped GaAs in the range 1.5–6 THz (50–200 cm^{-1}). The real and imaginary part of the dielectric function differ strongly from that for undoped GaAs, with the real part being negative. This causes a large imaginary part of the refractive index. As a consequence, highly n -doped GaAs behaves similar to a metal in the THz range. A quantitative uncertainty arises from the scattering time in this model, which is not precisely known. By THz time domain transmission measurement, a Drude scattering

2 Basic principles of THz QCLs

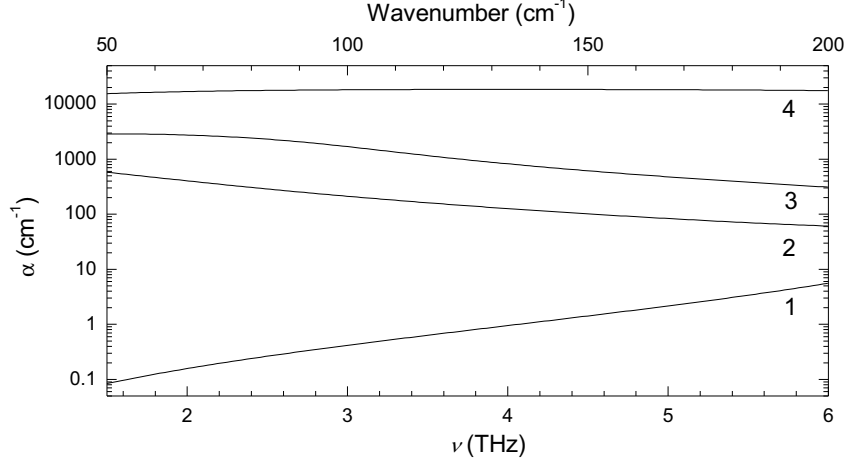


Figure 2.3: Calculated far-infrared absorption coefficient of GaAs for different doping densities at low temperatures. The doping densities from 1 to 4 correspond to $n = 0$, 2×10^{16} , 1×10^{17} , and $2 \times 10^{18} \text{ cm}^{-3}$. The assumed Drude scattering time is $\tau = 0.1 \text{ ps}$.

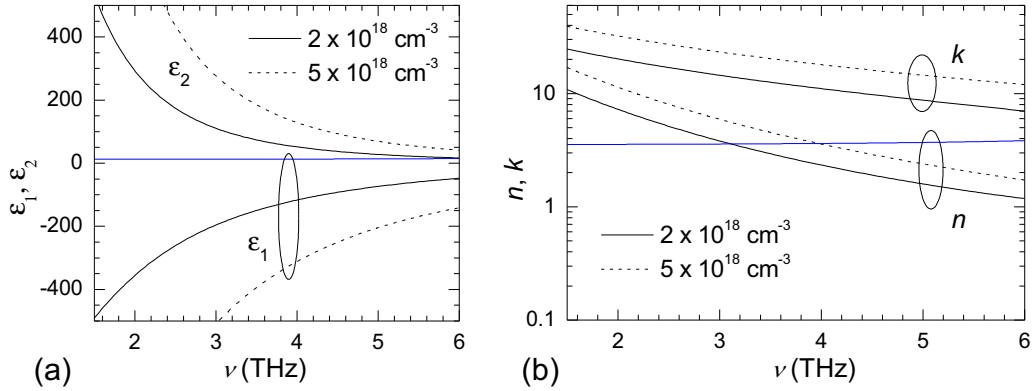


Figure 2.4: Calculated (a) dielectric function $\epsilon_1 + i\epsilon_2$ and (b) refractive index $n + ik$ for highly n -doped GaAs [logarithmic scale in (b)]. The solid blue lines in (a) and (b) indicate the corresponding values of ϵ_1 and n for undoped GaAs.

time of 0.09 ps has been confirmed for a highly n -doped ($2 \times 10^{18} \text{ cm}^{-3}$) GaAs layer with an error margin of 20% [39]. By a temperature-dependent Hall measurement for a highly doped GaAs layer ($n = 2.7 \times 10^{18} \text{ cm}^{-3}$), we found a dc scattering time of 0.06 ps, almost independent of temperature. However, the value at THz frequencies likely deviates from the dc value. Since in THz waveguides typically only a rather small part of the optical mode is confined within the highly doped layer, waveguide simulations as discussed in the following section yield very similar results in terms of the waveguide mode profile and the effective refractive index for values of τ in the range 0.05–0.3 ps.

In the case of electrons confined to quantum wells of a planar heterostructure such as a QCL, the Drude model of free-carrier absorption is valid only for transverse electrically (TE) or *s*-polarized light, i.e. light, which is polarized in the plane of the layers. For light which is transverse magnetically (TM) or *p*-polarized, i.e. perpendicular to the plane of the layers, the dielectric function is determined by discrete intersubband transitions. According to Agranovich [40], the dielectric tensor for a layered heterostructure is given by

$$\varepsilon_{xy} = \frac{1}{\sum l_i} \sum_i \varepsilon_i l_i, \quad (2.22)$$

$$\varepsilon_z^{-1} = \frac{1}{\sum l_i} \sum_i \frac{l_i}{\varepsilon_i}, \quad (2.23)$$

with ε_{xy} denoting the in-plane component of the dielectric tensor, ε_z the component in growth direction, and l_i and ε_i the thickness and dielectric function of layer i , respectively. For electrons which are confined in discrete subbands, Eq. (2.23) can strictly be applied only to the background dielectric function, i.e. without the carrier contribution. Due to the small Al content in the active region of THz QCLs, ε_z exhibits approximately the value of bulk $\text{Al}_x\text{Ga}_{1-x}\text{As}$, with x being the average Al content in the active region.

2.5 Waveguides and resonators of THz QCLs

In addition to the active-region heterostructure, a THz QCL is defined by the type of the resonator and the waveguide. The simplest type of a resonator is the Fabry-Pérot cavity, which consists of a waveguide with cleaved mirror facets. There exist two basic waveguide concepts for THz QCLs. In a metal-metal (MM) waveguide, the optical mode is confined between two metallic layers. In a single-plasmon (SP) waveguide (also called semi-insulating surface-plasmon waveguide), the optical mode is confined between a top metal layer and a highly doped GaAs bottom layer. Figure 2.5 shows a sketch of the cross-section for both waveguides and the vertical intensity profile of the guided mode.

For MM and SP waveguides, the confined optical mode is partly plasmonic, since the plasma frequencies of the metal and the highly doped GaAs layers are well above the frequency of the THz QCL. The term *single-plasmon* was introduced by Rochat *et al.* [41] for comparing properties of this type of waveguides with a similar concept based on highly doped substrates, which was called double-plasmon waveguide. However, the concept of SP waveguides had already been described in the pioneering paper of Köhler *et al.* [3]. Indeed, the first THz QCL was based on this type of waveguide.

A main difference between MM and SP waveguides is the confinement factor Γ of the guided mode, which is a measure of the overlap of the optical mode with the active region. For TM polarized modes, the magnetic field oscillates in the transversal direction, i.e. in the plane of the quantum wells, while the electric field oscillates (to a good approximation) in the growth direction, $\mathbf{E} \approx E_z \mathbf{e}_z$. For a given intensity profile of the waveguide mode, the confinement factor can be written as

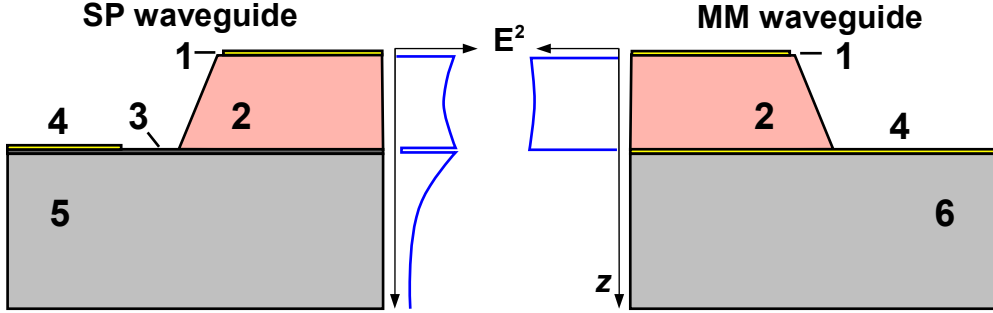


Figure 2.5: Cross-section of single-plasmon (SP) and metal-metal (MM) waveguides and intensity distribution of the fundamental laser mode. 1: top contact metal, 2: GaAs/(Al,Ga)As active region, 3: n^+ -GaAs layer, 4: lower contact metal, 5: semi-insulating GaAs substrate, 6: semi-insulating or n^+ -GaAs substrate. Typical dimensions are 10 μm for the height of the active region, 0.7 μm for the thickness of the highly doped lower contact layer, 50–200 μm for the width of the waveguide, and 20 μm for the gap between the bottom of the ridge and the lower contact metal.

$$\Gamma = \frac{\int_{\text{AR}} |E_z|^2 dA}{\int |E_z|^2 dA}, \quad (2.24)$$

where the integration is performed over the area of the active region (AR) in the numerator and over the whole waveguide area in the denominator. A stronger confinement is beneficial in terms of the threshold gain given by

$$g_{\text{th}} = \frac{\alpha_w + \alpha_m}{\Gamma}, \quad (2.25)$$

where α_w and α_m denote waveguide and mirror losses, respectively. g_{th} is related to the threshold current density J_{th} by

$$J_{\text{th}} = \frac{g_{\text{th}}}{\tilde{g}} = \frac{\alpha_w + \alpha_m}{\tilde{g}\Gamma} \quad (2.26)$$

with \tilde{g} denoting the differential gain (or gain factor), i.e. the increase of the gain with increasing current density below the lasing threshold. While for MM waveguides the confinement factor Γ is nearly unity and independent of the frequency, the optical mode extends significantly into the substrate with a frequency-dependent Γ ranging between about 0.2 and 0.5 in the case of SP waveguides. For that reason, the substrate for SP waveguides has to be semi-insulating to avoid free-carrier absorption. For both types of waveguides, the waveguide losses α_w are mainly caused by free-carrier absorption in the highly doped contact layers, the active region and, to a small amount, by absorption in the metallic layers and by residual phonon absorption.

A further difference between Fabry-Pérot cavities based on MM and SP waveguides is related to the mirror losses α_m , which can be written as

2.5 Waveguides and resonators of THz QCLs

Layer	Thickness (μm)	$n_{3\text{D}}$ (cm^{-3})
Top metallization (Au)	0.3	5.9×10^{22}
Top contact layer (GaAs:Si)	0.08	5×10^{18}
Active region ($\text{Al}_{0.02}\text{Ga}_{0.98}\text{As}$)	10	5×10^{15} or 0
Lower contact layer (GaAs:Si)	0.7	2×10^{18}
SI GaAs substrate	150–350	0

Table 2.2: Vertical scheme of SP waveguides as used for waveguide simulations. The dielectric functions of GaAs and (Al,Ga)As are discussed in Section 2.4. Used dielectric function for Au: $\varepsilon_{Au} = \varepsilon_{\infty} - n_{3\text{D}}e^2/[\varepsilon_0 m_0(\omega^2 + i\omega/\tau)]$ with $\varepsilon_{\infty} = 13$, $\tau = 0.014$ ps (best fit to data of [34]). A Drude scattering time of 0.1 ps has been used for the highly doped GaAs layers and 1 ps for the active region (cf. Ref. [38]).

$$\alpha_m = -\frac{1}{2L} \ln(R_1 R_2) \quad (2.27)$$

with L denoting the cavity length and R_1 and R_2 the reflectance of the front and back facet, respectively. For SP Fabry-Pérot cavities, the facet reflectance is approximately given by Fresnel's formula $R = (n-1)^2/(n+1)^2$ with a value of $R \approx 0.3$ for uncoated facets, while in the case of MM waveguides it has been found that R is significantly increased to values in the range of 0.5–0.9 due to the strong sub-wavelength confinement [38, 42]. As compared to Fabry-Pérot THz QCLs with SP waveguides, the output power of THz QCLs with MM waveguide is typically rather small, which is a consequence of the general relation $P_{\text{out}}/P_{\text{int}} = L\alpha_m = -\ln(R_1 R_2)/2$ for the ratio of the total output power P_{out} to the average internal power P_{int} . Another consequence of the strong confinement in THz QCLs with MM waveguides is a complex beam pattern [42, 43], which is not suitable for most applications; a disadvantage which can be partly avoided by using higher order gratings [44, 45]. Due to the stronger confinement and the reduced mirror losses, MM Fabry-Pérot THz QCLs have proven to be superior in achieving high operating temperatures, while SP THz QCLs are usually much more favorable in terms of output power and beam profile. Since the QCLs in this work are based on SP waveguides, the following quantitative discussion will focus on this type.

A vertical waveguide scheme as used for the simulations is given in Tab. 2.2. For the semiconductor layers, the dielectric functions discussed in the previous section have been used. The active region is considered as a single effective $\text{Al}_x\text{Ga}_{1-x}\text{As}$ layer with an Al content of $x = 0.02$. The two limiting cases of vanishing and bulk free-carrier absorption are simulated by setting the doping level of the effective active-region layer to zero in the former case and to the average doping level of the active region in the latter case. However, free-carrier absorption might not be a reasonable assumption for the active region, and alternatives are discussed below. Waveguide simulations have been performed using the software *JCMSuite* [46], which solves Maxwell's equations based on the finite-element method. Due to the selection rule for intersubband transitions, only TM-polarized waveguide modes are considered. The waveguide modes are found by solving Maxwell's equations in one dimension (1D) for an infinitely wide ridge or in two dimensions (2D) for

2 Basic principles of THz QCLs

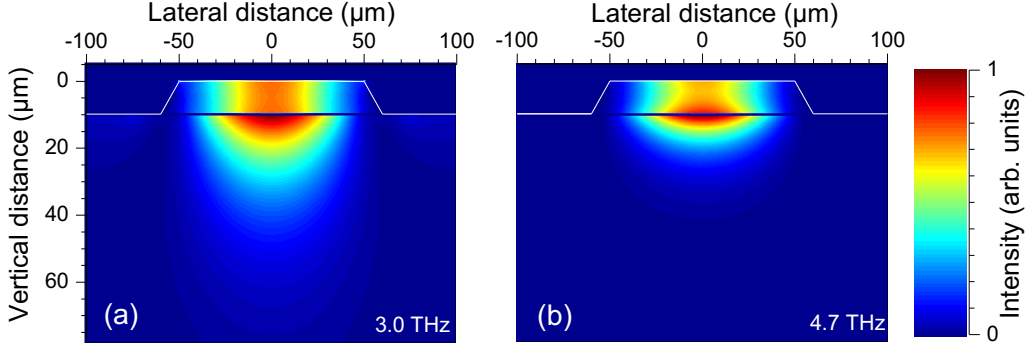


Figure 2.6: Calculated 2D intensity distribution of the low-loss SP waveguide mode for (a) 3.0 THz and (b) 4.7 THz. Free-carrier absorption and gain in the active region have been neglected.

a finite ridge width.

In Fig. 2.6, the 2D mode profile for a 120 μm wide waveguide is shown for 3.0 and 4.7 THz. The confinement factor increases from $\Gamma = 0.27$ at 3 THz to $\Gamma = 0.48$ at 4.7 THz. Since carrier absorption has been neglected for the active region, the waveguide losses of 8.6 cm^{-1} at 3 THz and 17.7 cm^{-1} at 4.7 THz are mainly caused by the highly doped GaAs contact layers as well as the top and bottom metallization.

In Fig. 2.7, the results of a 1D simulation are shown. The two cases of an active region with and without free-carrier absorption are compared. The strong difference in the dielectric function between highly doped and low-doped/undoped layers results in both cases in a significant dispersion with a frequency dependence of the effective refractive index n_{eff} , which is well approximated by a quadratic fit [cf. Fig. 2.7(a)]. In both cases, the waveguide losses increase with frequency, which is due to the increase of the absorption in the highly doped GaAs layers. By comparing the calculated losses of the 1D simulation and the 2D simulation for the 120 μm wide ridge, the additional losses due to the finite ridge width can be estimated to account for 35% of the total losses at 3 THz and 10% at 4.7 THz. Obviously, the influence of the regions next to the laser ridge vanishes with increasing frequency, which is consistent with an increasing confinement factor [cf. Fig. 2.7(c)]. The quantitative results are comparable to those of Kohen *et al.* [38] for single-plasmon waveguides. Note that the absolute values of the calculated losses depend on the particular scattering times, which are used for the Drude model. However, a reasonable agreement is found by comparison with experimental α_w values, which have been determined from the $1/L$ dependence of J_{th} .¹

Lower limits for the threshold gain at different frequencies are obtained from Eq. 2.25 by using the 1D values for the waveguide losses and confinement factors, which correspond to an infinitely wide laser ridge. For $\alpha_m = 0 \text{ cm}^{-1}$ (unity facet reflectance or infinitely long laser ridge), the lower limits for g_{th} are determined to be 19 cm^{-1} and 32 cm^{-1} at

¹For THz QCL ridges emitting around 3.8 THz, waveguide losses of 9 cm^{-1} have been extracted from the $1/L$ dependence of J_{th} (200 μm wide ridges), while at 4.5 THz the value has been 15 cm^{-1} (100 μm wide ridges) [47].

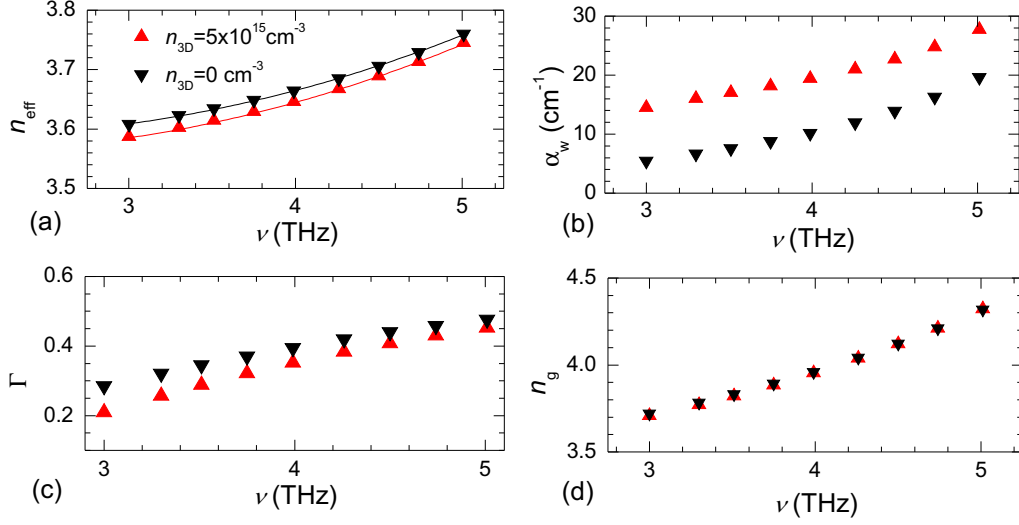


Figure 2.7: Calculated frequency dependence (1D) of (a) the effective refractive index, (b) the waveguide losses, (c) the confinement factor, and (d) the group refractive index in a SP waveguide considering doping-induced free-carrier absorption in the active region.

3.0 THz and 4.7 THz, respectively. For $\alpha_m = 3.5 \text{ cm}^{-1}$ (corresponding to a 3.5 mm long laser ridge with uncoated facets as typically used for pulsed-mode characterizations), the lower limits for g_{th} become 32 cm^{-1} and 43 cm^{-1} at 3.0 THz and 4.7 THz, respectively. The intrinsic gain of the active region has to exceed these values to allow for lasing.

In a Fabry-Pérot cavity, the frequency is determined by n_{eff} , while the spectral spacing of the modes is determined by the group refractive index n_g :

$$\Delta\nu = \frac{1}{2n_g L}. \quad (2.28)$$

n_g is given by the relation

$$n_g = n_{\text{eff}} + \nu \frac{dn_{\text{eff}}}{d\nu}. \quad (2.29)$$

The frequency dependence of n_{eff} , results in a significant difference between n_{eff} and n_g [cf. Figs. 2.7(a) and 2.7(d)]. Since free-carrier absorption in the active region causes an almost constant offset for n_{eff} , the difference in n_g between the cases with and without free-carrier absorption is relatively small.

Instead of the free-carrier absorption model, it appears to be more reasonable to use the oscillator model of the intersubband susceptibility [Eq. (2.15)] to account for the effect of carriers on the optical properties of the active region. In a first approximation, only the imaginary part of the susceptibility is considered, i.e. the gain in case of a QCL. Since the threshold gain depends via the mirror losses on the ridge length, the influence of the ridge length on the waveguide properties can be simulated. Because the magnitude of

2 Basic principles of THz QCLs

the refractive index of the active region increases in the presence of gain, the confinement factor increases as well. However, the effect is rather small causing at 3.75 THz an increase of Γ from 0.32 in the absence of gain to a value of 0.34 for a gain of 100 cm^{-1} , which corresponds approximately to the threshold gain of a 0.45 mm long cavity. Due to the different confinement, also the waveguide losses depend on the cavity length, but the effect is rather small (on the order of 1%). A correct treatment of the intersubband susceptibility would have to account also for the real part of the dielectric constant. In this case, the specific heterostructure and the applied field strength would enter the waveguide simulations, which makes general quantitative conclusions difficult. However, there is one important aspect. Due to the intersubband absorption at frequencies above the laser transition, the refractive index in the active region is increased, which increases the confinement factor. In contrast, free-carrier absorption in the active region decreases the refractive index and the confinement factor due to the small plasma frequency. Another aspect is related to the Kramers-Kronig relation. At the gain maximum, the real part of the susceptibility term related to the laser transition changes its sign. This causes a maximum in the real part of the refractive index on the low-frequency side of the gain peak and a minimum on the high-frequency side, while the strength of this effect depends on the threshold gain. This could explain the experimentally observed different tuning rates with driving current for the different spectral modes of a Fabry-Pérot THz QCL [48].

2.6 Basic concepts of the QCL active region

Basic principles of a QCL active region are well described by a rate equation model with constant scattering times. A typical rate equation approach for the population densities n_3 and n_2 of the upper and the lower laser level, respectively, and the internal photon density S is the following one [25]:

$$\frac{dn_3}{dt} = \eta_3 \frac{J}{ed} - \frac{n_3}{\tau_3} - \Gamma_p v_g g(n_3, n_2) S, \quad (2.30)$$

$$\frac{dn_2}{dt} = \eta_2 \frac{J}{ed} + \frac{n_3}{\tau_{32}} - \frac{n_2}{\tau_2} + \Gamma_p v_g g(n_3, n_2) S, \quad (2.31)$$

$$\frac{dS}{dt} = \Gamma v_g g(n_3, n_2) S - \frac{S}{\tau_{\text{ph}}} + \beta R_{\text{sp}}. \quad (2.32)$$

Here, η_i denote the injection efficiencies, d the thickness of the active-region period, τ_3 and τ_2 the total lifetimes of the electrons in the upper and the lower laser level, respectively, and τ_{32} the radiative lifetime. Γ denotes the total confinement factor of the active region, Γ_p the confinement factor per period, $v_g = c/n_g$ the group velocity, $\tau_{\text{ph}} = n_g/[(\alpha_m + \alpha_w)c]$ the cavity lifetime, $g(n_3, n_2)$ the gain, R_{sp} the spontaneous emission rate, and β the coupling factor for the spontaneous emission. Eqs. (2.30)–(2.32) are easily solved for the steady state case ($dn_i/dt = 0$). At threshold, the photon density is negligible, and with Eqs. (2.13) and (2.26) the threshold current density becomes

$$J_{\text{th}} = \frac{\alpha_w + \alpha_m}{\Gamma} \frac{ed n_{\text{eff}} c \epsilon_0}{e^2 \omega} \frac{\gamma_{32}}{2|z_{32}|^2} \frac{1}{\eta_3 \tau_3 (1 - \tau_2/\tau_{32}) - \eta_2 \tau_2}. \quad (2.33)$$

J_{th} decreases with increasing dipole matrix element z_{32} and decreasing transition broadening γ_{32} . A large population inversion $n_3 - n_2$ is obtained by an efficient injection, i.e. $\eta_3 \gg \eta_2$, and an efficient depopulation of the lower laser level, which enters as the ratio τ_2/τ_{32} . Different approaches exist to optimize these quantities. In a *vertical* design, the upper and lower laser levels are located in the same quantum well which maximizes z_{32} . In *diagonal* designs, these levels are located in different quantum wells, which usually results in a larger n_3 and a reduced parasitic injection η_2 into the lower laser level and also allows for a frequency tuning with the applied electric field due to the linear Stark effect. To improve the injection efficiency η_3 , the effect of resonant tunneling [49] is exploited in most QCLs by using a relatively thick injection barrier to separate the upper laser level from the n -doped injector region. The upper laser level is coupled resonantly to an injector state, which strongly enhances the injection efficiency. However, resonant coupling can also result in negative differential resistance, which eventually limits the operational range of most THz QCLs. In a *bound-to-continuum* design [50], the depopulation relies on the coupling of the lower laser level with an extraction/injection miniband. The efficiency of such a depopulation scheme increases for broader minibands due to the reduced thermal backfilling and an improved miniband transport as discussed in Section 2.3.3. The strong interaction of electrons with LO phonons is exploited in *resonant phonon* designs by incorporating an LO phonon-assisted transition. Due to the LO phonon energy of 36 meV in GaAs, this helps to reduce the thermal backfilling or to provide an efficient depopulation channel for the lower laser level.

Another quantity obtained by the rate equation model is the slope efficiency dP/dI , which is the differential increase of the output power per facet with current. It is related to the average internal photon density S and the internal differential quantum efficiency η_d by

$$\frac{dP}{dI} = \frac{1}{2} \hbar \omega \alpha_m v_g d \frac{dS}{dJ} = \frac{1}{2} \frac{\hbar \omega}{e} \frac{\alpha_m}{\alpha_m + \alpha_w} \eta_d. \quad (2.34)$$

Assuming that $\Gamma_p = \Gamma/N_p$ with N_p being the number of periods, Eqs. (2.30)–(2.32) lead to

$$\frac{dP}{dI} = \frac{1}{2} \frac{\hbar \omega}{e} \frac{\alpha_m}{\alpha_m + \alpha_w} N_p \frac{1}{1 + \frac{\tau_{32}\tau_2}{\tau_3(\tau_{32}-\tau_2)}} \left[\eta_3 - \eta_2 \frac{\tau_{32}\tau_2}{\tau_3(\tau_{32}-\tau_2)} \right]. \quad (2.35)$$

Obviously, the slope efficiency is maximized for unity injection efficiency and decreases, if electrons are also injected into the lower laser level ($\eta_2 > 0$) or if further parasitic channels occur ($\eta_3 + \eta_2 < 1$). With a few rearrangements, it is found that

$$\frac{dP}{dI} \propto \frac{1}{\tau_3(1 - \tau_2/\tau_{32}) + \tau_2} \frac{1}{J_{\text{th}}}. \quad (2.36)$$

If J_{th} is determined by the injection efficiency (no change in the scattering times), the slope efficiency becomes proportional to J_{th}^{-1} . Due to the gain clamping above threshold, the population inversion $n_3 - n_2$ remains constant, which results in a discontinuity in the differential resistance at threshold [49]. An expression for the differential resistance, derived within a density matrix model, can be found in Ref. [51].

Different active-region designs are further characterized by its voltage defect ΔV_p , de-

2 Basic principles of THz QCLs

noting the voltage drop in each period, which occurs in addition to that of the laser transition. The operating voltage of a QCL is given by

$$V_{\text{op}} = \left(\frac{\hbar\omega}{e} + \Delta V_p \right) N_p + V_s, \quad (2.37)$$

where the voltage V_s is due to the series resistance caused by the highly doped bottom contact layer and the bonding wires. The voltage defect is directly connected to Ohmic heating of the active region, independently of the radiative efficiency of the laser transition. For *resonant phonon* designs, the minimum value for ΔV_p is typically 36 mV, determined by the LO phonon energy. Under this aspect, the LO phonon-assisted transition can be considered as an efficient channel, which converts electrical energy into lattice heat. However, a certain voltage defect is required to avoid thermal backfilling of the lower laser level. For cw operation of THz QCLs at cryogenic temperatures, a low electrical input power is crucial, i.e. a small threshold current *and* a small operating voltage. For a certain voltage defect per period, the operating voltage is determined by the number of periods in the active region. Records for high-temperature pulsed operation have been achieved for *resonant phonon* designs with 2–3 quantum wells per period, but with the drawback of a required large number of periods (200–250) and eventually a high operating voltage [4, 51]. The alternative approach is to use a rather large number of quantum wells per period and therefore a smaller total number of periods to obtain a small operating voltage.

2.7 Intrinsic linewidth of QCLs

The intrinsic laser linewidth is a limiting quantity for applications, which require long coherence lengths or a high spectral resolution. In the Schawlow-Townes limit, the linewidth of a laser is determined by [52]

$$\Delta\nu = \frac{n_3}{n_3 - n_2} \frac{2\pi h\nu\tau_{\text{ph}}^{-2}}{P}, \quad (2.38)$$

where ν is the laser frequency and P the laser power. For interband semiconductor lasers, it is known that the minimum linewidth is limited by the fluctuation of the refractive index, which is caused by the fluctuation of the carrier density due to recombination [53]. This is expressed by multiplying Eq. (2.38) with a factor $(1 + \alpha_H^2)$ with α_H denoting the linewidth enhancement factor.

In contrast to interband semiconductor lasers, QCLs are unipolar devices, for which the carrier density is a conserved quantity, causing the intrinsic linewidth enhancement to be much smaller than that of interband lasers. A theory of Yamanishi *et al.* [54] predicts an intrinsic linewidth for QCLs, which can be even below the Schawlow-Townes limit, and for MIR QCLs some experimental evidence has been reported for a narrow linewidth of a few hundred Hertz [55]. Recently, a theoretical Monte Carlo simulation has predicted an intrinsic linewidth of the order of 50–300 Hz for THz QCLs [56]. By using a gas laser as a reference in a difference frequency mixing experiment, the intrinsic linewidth of a THz QCL has been found to be less than 30 kHz [52].

3 Design, fabrication and characterization

The fabrication of QCLs starts with the design of the heterostructure. Due to the many degrees of freedom, a numerical tool is used for calculating the wavefunctions and predicting the electrical and optical properties of a particular structure. After the epitaxial growth by molecular-beam epitaxy (MBE), the wafers are processed to form the waveguide structure and provide the electrical contacts. Following the processing, laser dies are cleaved and soldered onto copper submounts. Finally, the QCLs are electrically and optically characterized. Each of these steps will be briefly discussed in this Chapter.

3.1 Heterostructure design

The numerical design tool, which is used to simulate the QCL heterostructures, is based on a self-consistent solution of the Schrödinger and Poisson equations and a set of linear rate equations for the electron transport [22]. It yields the current density-electric field relation $J(F)$ and the frequency- and field-dependent optical gain $g(\nu, F)$, where F denotes the average electric field strength over one QCL period. The model has further been extended to include the effect of stimulated emission on the transport characteristics [57, 58], which allows for basic simulations of the lasing device.

The iteration loop starts with a solution of the Schrödinger equation for a given potential distribution. To account for the nonparabolicity of the conduction band, the two-band $\mathbf{k}\cdot\mathbf{p}$ approach described in Section 2.2 is applied to calculate the wavefunctions and eigenenergies for the periodic system as defined by Eqs. (2.5)–(2.6). Subsequently, a system of linear transport rate equations is solved to calculate the electron distribution within the QCL period. Finally, a solution of the one-dimensional Poisson equation yields the potential corrections for the next iteration loop.

While the solution of the one-dimensional Schrödinger and Poisson equations is relatively straightforward, the simulation of the electronic transport is not, as discussed in Section 2.3.2. To keep the calculation time small, the electrons are treated in a single-particle picture. The scattering rates are assumed to depend on the transition energy and the dipole matrix element, but not on the electron momentum. For a transition between subbands i and j , the scattering rate is given by

$$\tau_{ij}^{-1} = \gamma_E(E_i - E_j)|z_{ij}|^2 \quad (3.1)$$

with the energy-dependent factor γ_E , which is an empirical function. This results in a system of linear rate equations for the population densities n_i of each subband i . The advantage of this approach is a very efficient simulation of relevant properties. One drawback of this approach is that many-particle effects, such as the dephasing involved in resonant tunneling [27], cannot be treated. Another related deficiency is that the anticrossing of

3 Design, fabrication and characterization

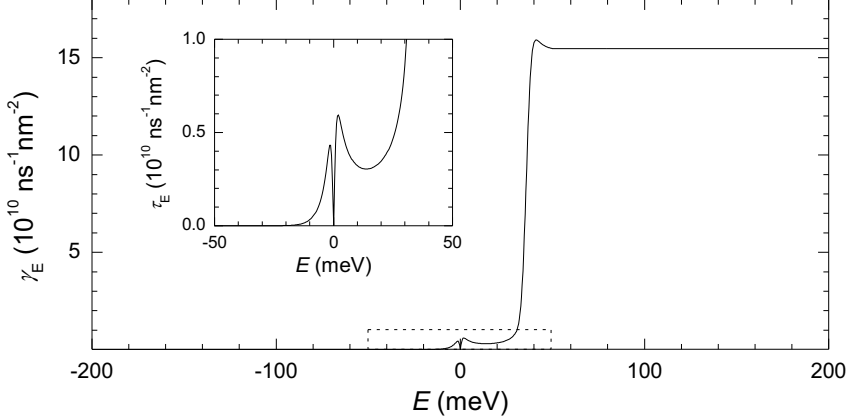


Figure 3.1: $\gamma_E(E)$ relation used for the rate equation-based transport simulations [22]. The inset shows an enlargement of the region marked by the dashed rectangle.

two remote states at a certain field strength results in artificial spikes in the calculated $J(F)$ characteristics, which are not observed experimentally. This is due to the formation of two largely extended wavefunctions at the anticrossing field strength. For the rate equation model, the electrons are treated as fully delocalized in either of the states. However, the mixed state should indeed propagate on a time scale determined by the oscillation of the coupled system. If the oscillation period is of the order or above the scattering time for each of the coupled states, the rate equation model yields erroneous results. A further problem of Eq. 3.1 is that it suggests a parity selection rule also for phonon-assisted transitions, which is in contradiction to the established theory of phonon scattering (cf. Ref. [26]). However, for a large class of THz structures, this parity problem seems to be not an issue. We find that in most cases only states, which are ground-state-like and first-excited-state like in terms of a square-well parity exhibit significant levels of population, i.e. contribute to the transport. Since dipole-transitions between such states are allowed, also phonon-assisted transport can be approximated (to a low order) by Eq. 3.1.

Figure 3.1 depicts the $\gamma_E(E)$ relation used for the numerical simulations. The large step at 36 meV is due to the onset of LO phonon scattering. While in the one-dimensional transport model the electrons are considered to have zero in-plane momentum, a nonzero temperature is simulated by a finite scattering time for negative energies, i.e. $\gamma_E(E_i - E_j) > 0$ for $E_i - E_j < 0$. However, a consistent systematic simulation of temperature effects is not possible within this approach.

The prediction of gain for a certain heterostructure by the numerical simulations can be considered a necessary, but not sufficient condition for obtaining a THz laser. This is related to the role of negative differential resistance. If the optical gain falls into such a regime, it is not accessible by electrical pumping due to the formation of electric-field domains.

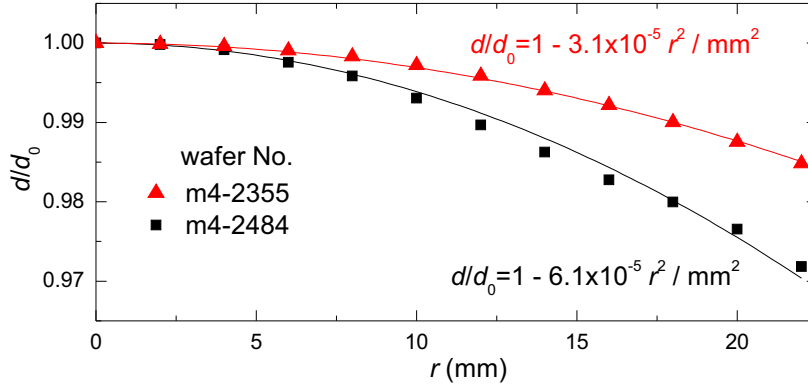


Figure 3.2: Variation of the relative period length d/d_0 with distance r from the center of the wafer as determined for two distributed Bragg reflector structures grown at different filling levels of the Ga effusion cells [59].

3.2 Epitaxial growth

All wafers have been grown in a VG V80H MBE system, equipped with Al, As, Ga, and Si effusion cells. By using two Ga cells, $\text{Al}_x\text{Ga}_{1-x}\text{As}$ barriers with two different compositions x can be grown during one run without changing the cell temperatures. The growth chamber is equipped with an optical system to monitor the growth rate by means of continuous spectral reflectance measurements (Filmetrics F30). After growth, wafers are characterized by x-ray diffraction and capacitance-voltage (C - V) measurements. The THz QCLs investigated in this work have been grown on semi-insulating (SI) GaAs (001) substrates. The typical growth sequence consists of a GaAs buffer layer (300 nm), an undoped $\text{Al}_{0.95}\text{Ga}_{0.05}\text{As}$ layer (75 nm) to enhance the contrast for the optical monitoring, a highly n -doped GaAs layer (700 nm), which acts as the bottom electrical contact and waveguide layer, the active-region sequence (10 μm), and a highly n -doped GaAs layer (50 nm) for the top contact. Detailed growth sequences of the investigated QCLs are given in the Appendix. Due to the large active-region thickness, a single growth run lasts about 12–18 hours. To account for the decreasing filling level of the effusion cells, the temperature of the cells is readjusted during growth. Caused by the geometry of the MBE system, the wafers exhibit a radial thickness gradient.

In Fig. 3.2, the thickness gradient is shown as a function of the distance from the center of the wafer for two different times after refilling the effusion cells. The data have been obtained from a determination of the resonance wavelength of microcavity resonator structures [59]. A parabolic dependence of the thickness gradient is obtained in both cases with a deviation of about 1.5% at the wafer edge (growth edge) in case of the higher filling level (sample M4-2355) and 3% in case of the lower filling level (sample M4-2484). This deviation with time is mainly caused by the conic geometry of the Ga effusion cells. By using the optical monitoring system to adjust the growth rate in situ, it is possible to keep the period length at a certain distance from the center within 1% of a reference value, as

revealed by post growth x-ray diffraction measurements. Without the monitoring system, the average period length deviates typically within less than 3% from the reference value, in a few cases within 7%. Since the x-ray data are typically obtained for a region close to the wafer edge, the nominal thickness values in the center of the wafer are approximately met, if the x-ray data reveal a deviation of about -1 to -2% depending on the filling level of the effusion cells. The influence of the distance from the center of the wafer on the lasing characteristics of THz QCLs is discussed in Section 6.3.

The level of n -doping in the doped layers is determined by the temperature of the Si cell, which is adjusted according to a calibrated flux/temperature characteristic. The doping level of each sample is usually confirmed by C - V measurements [60]. For these measurements, the highly doped upper contact layer is removed, and either an evaporated Au contact or a Hg probe is used to form the Schottky contact. Due to the rather limited accuracy of the method, the doping level is only known with a precision of approximately 25%.

3.3 Post-growth fabrication

Following the growth, the wafers are processed into ridge waveguide structures. The fabrication of the Fabry-Pérot SP QCLs discussed in this work is based on a wet chemical processing scheme. A first lithographic mask defines the waveguide ridges, which are subsequently formed by wet chemical etching using $\text{H}_2\text{SO}_4:\text{H}_2\text{O}_2:\text{H}_2\text{O}$ (1:1:8). The etch depth is controlled by the etching time and the etching rate (about $1 \mu\text{m}/\text{min}$) and verified ex situ by a tactile profilometer. A second lithographic mask defines the top and bottom contact metal stripes. To clean the resist windows prior to metal deposition, the sample is exposed to an O_2 plasma (2–3 min) followed by a solution for oxide removal ($\text{HCl}:\text{H}_2\text{O}$, 1:3). Subsequently, the metal is evaporated followed by the lift-off step. $\text{Au}_{0.995}\text{Ge}_{0.005}/\text{Ni}$ (300 nm) is used to provide Ohmic contacts with a low resistance. For that reason, the electrical contacts are eventually annealed at 450°C for 3 min. To allow for soldering, the backside of the substrate is evaporated with Ti/Au (10/100 nm).

In the case of THz QCLs with lateral corrugated gratings (cf. Chapter 7), a separate lithographic step is used for the corrugated top-metal contact, which is fabricated prior to the etching step (100 nm AuGe/Ni). To obtain vertical sidewalls, the corrugated laser ridges are dry etched by reactive ion etching.

For the fabrication of MM waveguides, which are not a subject of this work, an additional substrate transfer process is required. The epoxide of the QCL wafer and a recipient substrate are evaporated with a thick layer of Au (> 500 nm) prior to the processing steps already explained. The two gold faces are subsequently welded with each other in a thermo-compression bonding process, forming the bottom metallization of the MM waveguide. In a next step, the substrate of the QCL wafer piece is removed by mechanical lapping and selective wet-chemical etching, for which the $\text{Al}_{0.95}\text{Ga}_{0.05}\text{As}$ layer acts as an etch stop. The next processing steps are the same as for the fabrication of SP waveguides. However, the electrical polarity is reversed.

After processing, laser dies are formed by cleaving. Typically, the die has a width of 2 mm, containing three or four laser stripes. The length of the laser cavities defined by the cleaved facets lies in the range of 0.5–5 mm. The laser dies are soldered with indium to gold-

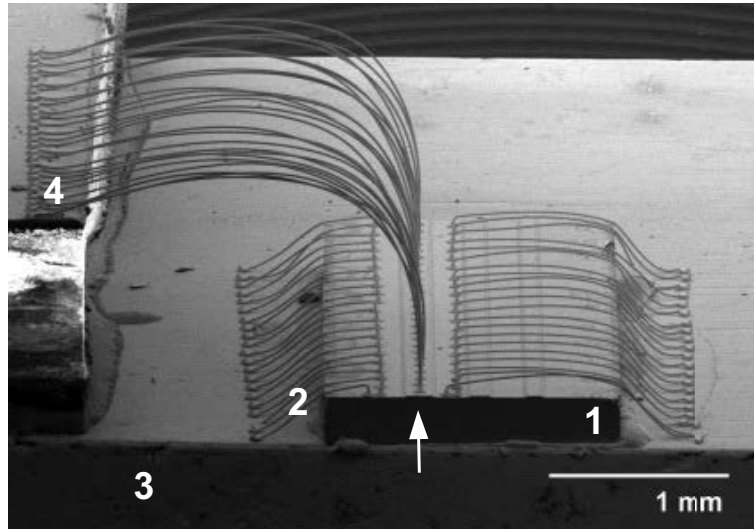


Figure 3.3: [Scanning-electron microscopy (SEM) image of a mounted THz QCL] Scanning-electron microscopy (SEM) image of a mounted THz QCL. 1: laser die (the arrow marks the bonded laser ridge). 2: bonding wires (bottom contact). 3: Cu submount. 4: bond pad with bonding wires for the top contact (electrically insulated from the submount).

plated, oxygen-free copper submounts. Some laser dies have been alternatively attached with silver epoxy to the submount. In the case of low-duty-cycle pulsed operation, for which the Ohmic heating is still negligible, no significant difference to indium soldering has been observed for the laser characteristics. However, for cw operation, indium solder has proven to be superior due to its much higher thermal conductivity, which is about $90 \text{ W m}^{-1}\text{K}^{-1}$ [61] as compared to about $2 \text{ W m}^{-1}\text{K}^{-1}$ for the silver epoxy [62].

After the mounting procedure, one of the laser stripes is electrically connected by wire bonding. Due to the semi-insulating substrate, bonding wires have to be attached to the top and to the bottom contact. Because of the rather high sheet resistance of the highly doped bottom contact layer, the bonding of the lower contact is performed on both sides of the laser ridge. Figure 3.3 depicts a mounted QCL die with attached wire bonds. The contacted laser ridge is marked by an arrow. Typically, a large number of bonding wires is used to ensure a homogeneous current injection, and to avoid contact degradation during cw operation.

3.4 Characterization

For the characterization, the THz QCLs are mounted in a He-flow cryostat (Oxford Instruments, Optistat CF1104) with polyethylene (PE) windows. For pulsed operation, a pulsed current source is applied (typically Avtech, AV-107C-B; alternatively ILX Lightwave, LDP-3840). For cw operation, either a laser diode current source (ILX Lightwave, LDX-3232) or a multipurpose source measure unit (Keithley, 2635A) is used. The QCL

3 Design, fabrication and characterization

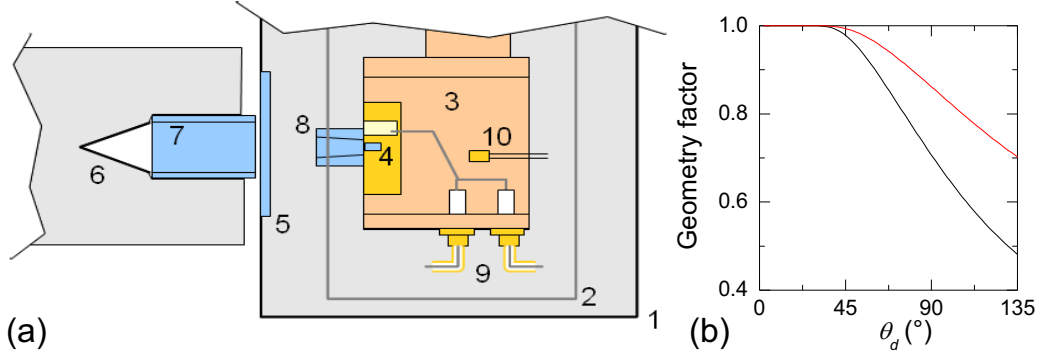


Figure 3.4: (a) Schematic diagram of the setup for power measurements. 1: outer cryostat vessel, 2: cold shield, 3: Cu cold finger, 4: QCL on Cu submount, 5: PE window, 6: pyroelectric detector, 7: cylindrical Al light pipe, 8: conical Al light pipe, 9: 50 Ω coaxial cables, 10: temperature sensor. (b) Geometry factor (collection efficiency neglecting window losses) vs. divergence angle θ_d for this setup, assuming divergence in one direction only (red line) and in both directions (black line).

emission spectra are measured with a Fourier transform infrared spectrometer (FTIR) (Bruker, IFS66v), which has a maximum resolution of 0.12 cm^{-1} . The detector is either a He-cooled Si bolometer or a pyroelectric detector based on deuterated triglycene sulphate (DTGS). Ge-coated Mylar is used as a beamsplitter for the frequency range of $30\text{--}700 \text{ cm}^{-1}$ ($0.9\text{--}21 \text{ THz}$). To measure the current and voltage amplitudes during pulsed operation, a digital storage oscilloscope is used (Tektronix, DPO7040). A voltage signal corresponding to the current value is provided by the monitor output of the Avtech current pulser, and the voltage is measured directly across a 50Ω impedance in parallel to the QCL, i.e. across a terminated 50Ω coaxial cable. To perform automated measurements of the light-current-voltage (L - I - V) characteristics, a *Labview* program is used. The absolute output power of the THz QCLs is measured with a pyroelectric power meter (Laserprobe Inc, RkP-575 RF). Note that currently no calibration standard exists for the power measurements in the THz range. However, Werner *et al.* [63] have calibrated the same type of detector against a cryogenic radiometer and found an absolute agreement of the output power values within 20%. For the power measurements, the power meter is placed directly in front of the cryostat window. For pulsed operation, the required 30 Hz modulation is provided by an external gating trigger, which controls the current pulser. To reduce losses in the remaining optical path due to the beam divergence, the light is guided by a conical Al pipe attached in front of the QCL and a cylindrical Al pipe in front of the pyroelectric detection area. A schematic diagram of the setup is shown in Fig. 3.4(a). For a comparison of experimental and simulated output power-current characteristics or for calculations of the quantum efficiency, it is sometimes desirable to know the real collection efficiency of the setup.¹ Figure 3.4(b) shows the calculated geometry factor, which is the collection efficiency neglecting window losses for a Gaussian intensity distribution. The

¹Due to the cryogenic operating temperatures for THz QCLs, standard setups based on Ulbricht spheres cannot be applied for measurements of the total power.

	θ_{vertical}	$\theta_{\text{lateral}}^{(a)}$	$\theta_{\text{lateral}}^{(b)}$	$\eta_{\text{collect}}^{(a)}$	$\eta_{\text{collect}}^{(b)}$
$\nu = 3.0$ THz	96°	54°	106°	0.66	0.53
$\nu = 4.7$ THz	110°	34°	68°	0.55	0.52

Table 3.1: Calculated $1/e^2$ far-field divergence angles in the vertical (θ_{vertical}) and lateral (θ_{lateral}) directions for the fundamental waveguide mode of (a) a 200 μm wide and (b) a 100 μm wide ridge as well as corresponding estimates for the collection efficiency η_{collect} for the power measurement setup shown in Fig. 3.4(a).

divergence angle θ_d denotes the opening angle of the beam at which the intensity dropped to $1/e^2$ of its maximum value. Both limiting cases are shown: negligible divergence in one direction and the same divergence in both directions. Depending on the dimensions of the laser ridge, the beam divergence of a semiconductor laser typically differs in the two directions parallel and perpendicular to the growth axis. The far field corresponding to a waveguide mode is essentially the Fourier transform of the near field at the facet times a correction factor for large angles called the obliquity factor. It has been calculated for the fundamental waveguide mode at 3.0 and 4.7 THz (100 μm and 200 μm ridge widths) following the approach described in Ref. [64].

The calculated divergence angles in the lateral and vertical directions are summarized in Tab. 3.1. As a consequence of the Fourier transform, the far-field divergence angle decreases with increasing spatial extent of the waveguide mode in the particular direction and with increasing frequency. The increased vertical divergence at 4.7 THz as compared to 3.0 THz is due to the much stronger vertical confinement at 4.7 THz. Since the lateral confinement does not change essentially from 3.0 to 4.7 THz, the lateral divergence decreases with increasing frequency. The collection efficiency for the fundamental mode can be estimated by taking into account the geometry factor and the transmittance of the PE window, which is 80% at 3.0 THz reducing to 70% at 4.7 THz. For 200 μm wide ridges, values for the collection efficiency are estimated to be 66% at 3.0 THz and 55% at 4.7 THz. For 100 μm wide ridges, the values are 53% and 52%, respectively. To avoid an overestimation of the output power, the collection efficiency of the setup for power measurements under pulsed operation is treated as unity in the following. For the cw power measurements, a chopper wheel is inserted into the optical path, which reduces the collection efficiency to typically 30% with respect to the pulsed-mode setup.

Another aspect of the cryogenic setup is the measurement and control of the temperature during the operation of QCLs. To regulate the temperature, the cryostat is equipped with a heating resistor. The temperature is measured at two positions: at the cooling head of the cryostat, to which the cold finger with the QCL is attached, and at the cold finger itself as shown in Fig. 3.4(a). The temperature measured by the second sensor is typically higher than that of the first one due to the non-perfect thermal insulation and the heat generated by the QCL. The operating temperature of the setup is defined as the temperature of the cooling head, which has approximately the temperature of the coolant liquid with the heater switched off. For measurements under pulsed operation, the duty cycle is typically in the range 0.25–0.5%, and the Ohmic heat generated by the QCL is therefore negligible. However, during cw operation, the heat generated by the QCL can

3 Design, fabrication and characterization

become several Watts, which has to be compensated by the temperature control loop. Since the original temperature controller has quite a large time constant, fast cw $L-I-V$ measurements at a constant temperature are performed by directly reducing the driving power of the heating resistor by the amount of the QCL driving power.

4 Low-voltage, high-power THz QCLs emitting around 3 THz

For practical applications of THz QCLs such as local oscillators in THz heterodyne detection, the laser has to be operated in cw mode. All THz QCLs reported to the date of this work rely on cryogenic cooling [6, 42, 65], and some physical arguments of that limitation will be discussed later. The cryogenic cooling imposes a major restriction for the cw operation of THz QCLs, since the size and cost of cryogenic cooling systems scale with the total power, which has to be dissipated at a certain temperature. A typical value for a small Stirling cooler is 7 W for the total power, which can be dissipated at 65 K [66]. Therefore, practical applications of THz QCLs as cw sources require a small electrical driving power. For that reason, not only the threshold current density is a decisive parameter, but also the operating voltage.

For the maximum operating temperature of THz QCLs, it has been shown to be beneficial, if the lower laser level is separated from the upper laser level of the next period by an LO phonon-assisted intersubband transition due to a reduced thermal population of the lower laser state [4, 67]. This holds in particular for pulsed operation, for which the operating voltage is of minor importance. For designs including LO phonon-assisted transitions, a low-temperature limit (negligible electron temperature) for the voltage drop per period V_{op}/N_p is given by the LO phonon energy $\hbar\omega_{\text{LO}}$ and the photon energy $\hbar\omega$,

$$\frac{V_{\text{op},\text{min}}}{N_p} = \frac{1}{e} (\hbar\omega + \hbar\omega_{\text{LO}}). \quad (4.1)$$

At elevated temperatures, Eq. (4.1) might be regarded as a lower limit for the optimum voltage, since electrons with sufficient in-plane momentum can undergo an LO phonon-assisted transition also for subband separations smaller than the GaAs LO phonon energy of 36 meV, but for a decreased scattering rate [26].

In this chapter, THz QCLs are discussed, which rely on such LO phonon-assisted transitions in the active region and emit around 3 THz. The following section deals with the active-region design and a detailed discussion of the QCL characteristics for a particular wafer. Subsequently, the results of a doping series are summarized.

4.1 Active-region design and QCL characteristics

The active-region period of the QCLs discussed in this chapter is based on nine quantum wells following the usual approach of an injector region and an optical transition region, which are separated by an injection barrier. The conduction band profile and the squared moduli of the wavefunctions are shown in Fig. 4.1 for an operating field strength of 4.4 kV/cm. The LO phonon-assisted transition takes place from the quasi-miniband

4 Low-voltage, high-power THz QCLs emitting around 3 THz

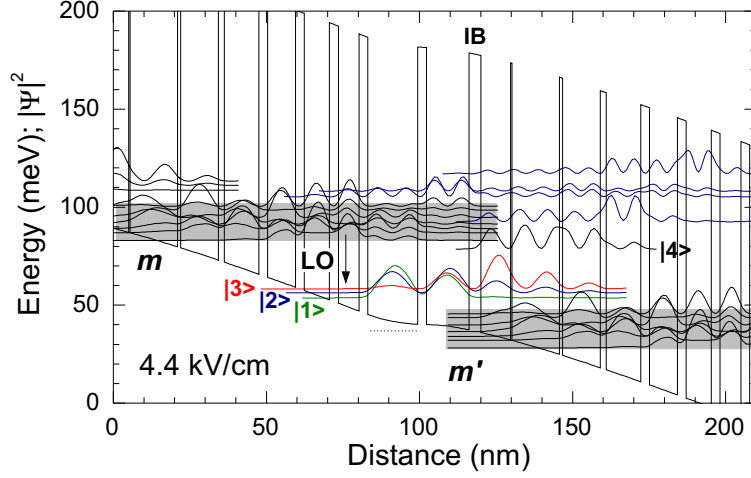


Figure 4.1: Calculated conduction band profile and squared moduli of the wavefunctions for the nominal active-region period of sample M4-2243 at an average field strength of 4.4 kV/cm. IB: injection barrier. LO: LO phonon-assisted transition. The doped quantum well is indicated by the horizontal dotted line.

labeled m to one of the states labeled $|1\rangle$ and $|2\rangle$, while the lasing transition occurs from one of the states $|2\rangle$ and $|3\rangle$ to the quasi-miniband m' . Potential parasitic current channels arise by a transition from the quasi-minibands m to m' via the gap state $|4\rangle$ or by scattering of electrons from m into other excited states to the right side of the injection barrier.

The $g(\nu, F)$ and $J(F)$ relations as obtained from a numerical simulation of the nominal active-region sequence are shown in Figs. 4.2(a) and 4.2(b), respectively. To account for inhomogeneous broadening effects, a broadening of 0.5 meV in addition to the lifetime broadening is assumed for each subband (stimulated emission is not taken into account).

Several regions of gain are found, depending on the field strength and the frequency. However, only gain within regions of positive differential resistance can be accessed by electrical pumping. According to the result of the $J(F)$ simulation, the large gain, which occurs above a field strength of 7 kV/cm, cannot be exploited due to the presence of NDR. A gain region with positive differential resistance is found between 3.5 and 5.5 kV/cm and 3–4 THz, with a peak gain of 52 cm^{-1} at 4.4 kV/cm. However, the exact value of the peak gain is difficult to predict for this structure, since the calculated gain is affected by the reabsorption region at higher frequencies caused by the $|3\rangle \rightarrow |4\rangle$ transition. Neglecting the additional broadening of 0.5 meV, the value of the peak gain becomes 150 cm^{-1} due to a reduced reabsorption and a reduced broadening of the laser transition.

In the following, experimental results for the wafer M4-2243 are discussed. For this sample, the x-ray and C - V measurements revealed a deviation of the average period length d of -4% with respect to the nominal value d_0 and a doping density of $7.0 \times 10^{10} \text{ cm}^{-2}$ in each period. In Fig. 4.3(a), the L - I - V characteristics for a 200 μm wide and 3.4 mm long laser stripe under pulsed operation are shown for different temperatures. At 5 K, the threshold current density is 175 A cm^{-2} increasing to 785 A cm^{-2} at the maximum oper-

4.1 Active-region design and QCL characteristics

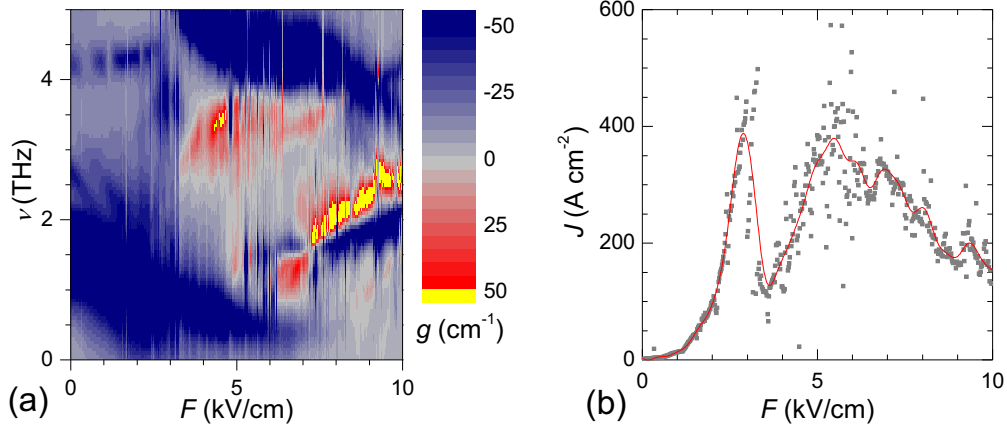


Figure 4.2: (a) Calculated frequency- and field-dependent gain $g(\nu, F)$ and (b) calculated current density-field relation $J(F)$ (sample M4-2243, nominal sequence). As a guide to the eye, the $J(F)$ data (black dots) have been smoothed (red line). At $F = 4.4$ kV/cm, values for the peak gain, transition energy, dipole matrix element, total lifetime of upper and lower laser level, and radiative transition lifetime are 52 cm^{-1} , 14.0 meV , 5.2 nm , 1.6 ps , 0.9 ps , and 12 ps , respectively.

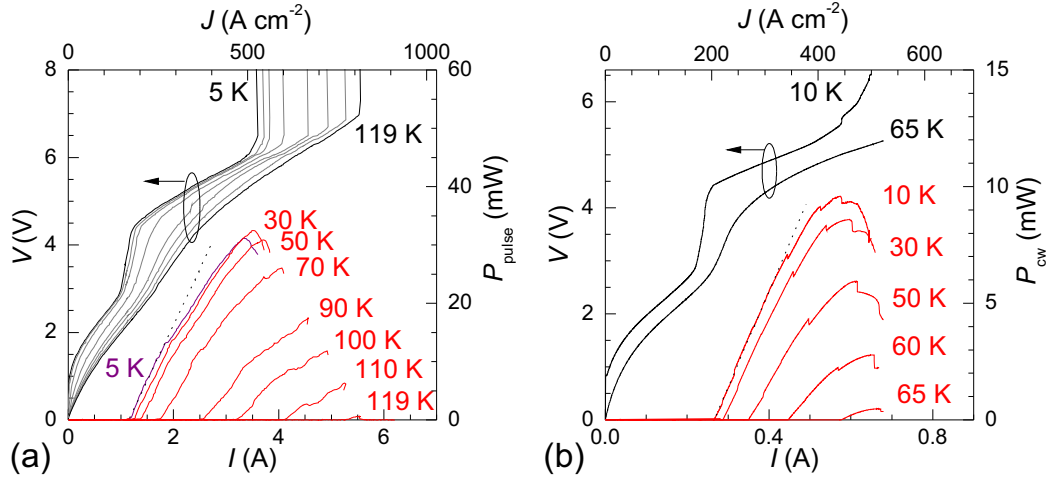


Figure 4.3: (a) $L-I-V$ characteristics for a $0.2 \times 3.4 \text{ mm}^2$ laser stripe of the wafer M4-2243 operated in pulsed mode with 500 ns and 5 kHz . P_{pulse} denotes the output power during pulsed operation divided by the duty cycle of 0.25% . (b) $L-I-V$ characteristics for a $0.1 \times 1.3 \text{ mm}^2$ laser stripe operated in cw mode. Due to the heating during cw operation, the temperature of 10 K is maintained only up to 425 A cm^{-2} . The dashed lines in (a) and (b) are fits to the linear slope of the low-temperature $L-I$ characteristics.

4 Low-voltage, high-power THz QCLs emitting around 3 THz

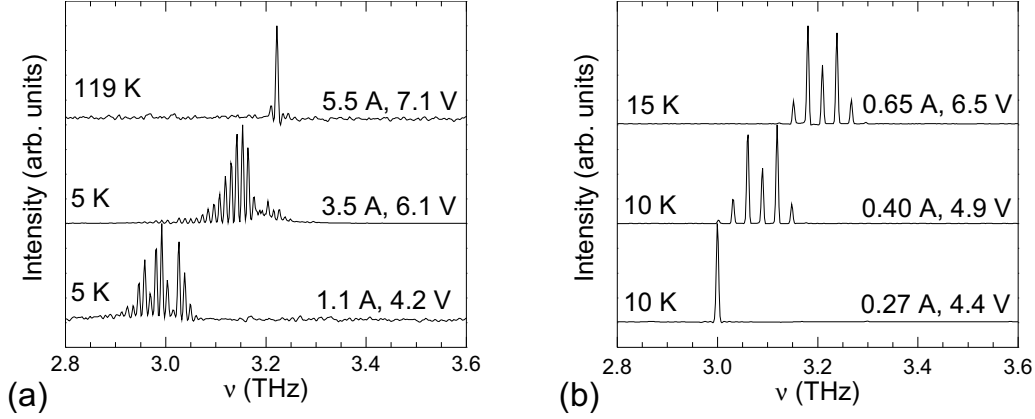


Figure 4.4: (a) Lasing spectra of a $0.2 \times 3.4 \text{ mm}^2$ laser ridge of sample M4-2243 close to threshold and close to operation with the maximum output power at 5 K and at the maximum operating temperature of 119 K (pulsed operation with 500 ns and 5 kHz). (b) Continuous-wave lasing spectra of a $0.1 \times 1.3 \text{ mm}^2$ laser ridge from the same wafer close to threshold and close to the maximum output power at low temperatures.

ating temperature of 119 K. Lasing starts above the first kink in the I - V characteristics, which is related to the alignment of the quasi-miniband (in the following called extraction/injection miniband). The peak output power P_{peak} , which is the maximum output power during pulsed operation divided by the duty cycle, is found to be 32 mW per facet at a temperature of 30 K (not corrected for collection efficiency). The drop of the output power corresponds to a large discontinuity in the differential resistance, which is related to the onset of NDR in the simulations. The slope efficiency dP/dI has its maximum value at the low-temperature threshold with 19 mW/A indicated by the dashed line in Fig. 4.3(a). Due to the large area of this ridge, the electrical power required to drive the laser is rather large (in the range of 5–40 W), which prevents cw operation of this ridge.

Continuous-wave operation with high-output powers has been possible for a 100 μm wide and 1.3 mm long laser ridge. In Fig. 4.3(b), the cw L - I - V characteristics are shown for different temperatures. Due to the higher mirror losses of this stripe, the threshold current density is increased to 205 A cm^{-2} at 10 K. The maximum cw operating temperature is 67 K, while pulsed operation is possible up to 97 K for this laser. The maximum cw output power P_{cw} is 9.5 mW at low temperatures and still 0.5 mW at 65 K. The maximum slope efficiency is 41 mW/A at 10 K. Its higher value as compared to the 3.4 mm long stripe is in accordance with Eq. (2.34), which predicts an increase of the slope efficiency due to the higher mirror losses of the shorter stripe.

The lasing spectra as measured under pulsed operation of the $0.2 \times 3.4 \text{ mm}^2$ laser ridge are shown in Fig. 4.4(a). The spectra exhibit the typical comb-like Fabry-Pérot structure. At low temperatures, the laser emits at threshold within the range of 0.1 THz around a central frequency of 3.0 THz. The central frequency shifts with increasing current and voltage toward higher values. At the maximum operating temperature, the laser emits mostly in a single longitudinal mode at 3.2 THz resulting in a total lasing range

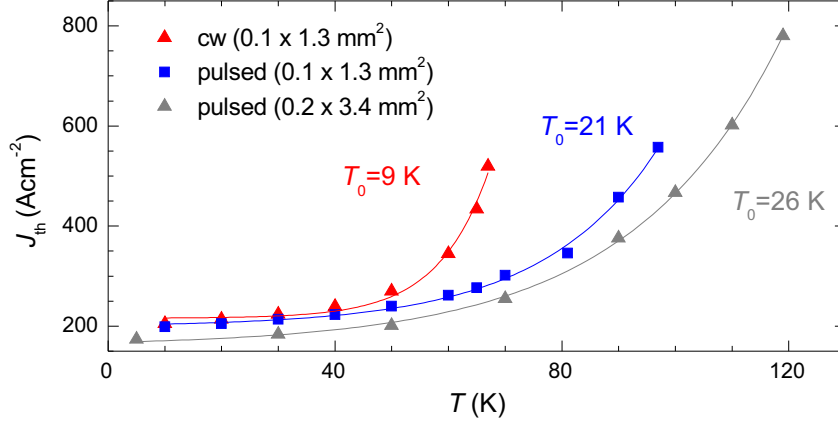


Figure 4.5: Temperature dependence of the threshold current density of sample M4-2243 for different ridge dimensions and operation modes (cw and pulsed operation with 500 ns, 5 kHz).

of 0.3 THz for this device. The shift of the central frequency is a consequence of the linear Stark effect. Due to the diagonal laser transition in this structure, i.e. the upper and lower laser level are centered in different quantum wells, the transition energy shifts approximately linearly with the applied electric field. This effect is also qualitatively reproduced in the calculated $g(\nu, F)$ dependence shown in Fig. 4.2(a), for which an almost linear shift with field strength is obtained. The cw lasing spectra for the 0.1×1.3 mm² laser ridge are depicted in Fig. 4.4(b). Due to the smaller stripe length, the spacing of the Fabry-Pérot modes is larger in this case. Again, a blue shift of the central lasing frequency with increasing bias is found. While the total lasing range of this QCL is also 0.3 THz, a rather large electrical power and a low temperature are required to observe the modes at the highest frequencies. The usable range may be reduced in systems with a smaller cooling power such as a Stirling cooler. In Fig. 4.5, the temperature dependence of the threshold current density is shown for both QCLs and different operating modes. The threshold current density follows the typical phenomenological exponential behavior $J_{\text{th}} = J_0 + J_1 \exp(T/T_0)$ with a T_0 values for pulsed operation of 26 K of the large-area ridge and 21 K for the small-area ridge (9 K for cw operation). From a comparison of the $J_{\text{th}}(T)$ characteristics for pulsed and cw operation, the additional increase of the active-region temperature during cw operation can be determined, and, with the corresponding values for the cw electrical driving power, the thermal resistance of the device is obtained. The values for the maximum cw and pulsed operating temperature are related via the electrical driving power P_{el} and the thermal resistance R_{th} of the device, i.e. $T_{\text{max,cw}} = T_{\text{max,pulsed}} - R_{\text{th}}P_{\text{el}}$. A value of $R_{\text{th}} = 9$ K/W is found for the small-area ridge, which corresponds to a temperature increase of 32 K in the active region at the maximum cw driving power of 3.6 W.

The active region contains 85 periods, which yields a value of $V_{\text{op,min}} = 4.1$ V according to Eq. (4.1). This is close to the experimental operating voltage of 4.45 V at threshold (10 K), which includes also the voltage drop due to the series resistance. The resistivity

4 Low-voltage, high-power THz QCLs emitting around 3 THz

Sample No.	M4-2235	M4-2326	M4-2243	M4-2239	M4-2247	M4-2325
n_{dop} (10^{10}cm^{-2})	4.8 (4.25)	6.1 (4.25)	7.0 (4.25)	9.2 (5.1)	11 (6.0)	20 (17)
$\Delta d/d_0$ (%)	-5.7	-3	-4.2	-1	+6.5	-3
T_{max} (K)	110	116	119	107	115	90
J_{th} (A cm^{-2})	330	370	175	295	185	840
J_{max} (A cm^{-2})	750	890	500	870	480	1280
V_{th} (V)	4.3	4.15	4.2	4.8	3.75	4.45
P_{peak} (mW)	41.5	66	32.5	45	48.5	22.5
dP/dI (mW/A)	17	24	19	16	33	14
ν (THz)	3.15–3.4	2.95–3.25	2.95–3.25	3.3–3.6	2.7–3.0	3.1–3.4

Table 4.1: Characterization results for a doping series. The lasing parameters are obtained for pulsed operation (500 ns, 5 kHz) of laser ridges with dimensions of $0.2 \times 3.3 \dots 3.6$ mm². n_{dop} denotes the sheet doping density per period as determined by C - V measurements (nominal values in brackets), $\Delta d/d_0$ the deviation of the average period length with respect to the nominal value as determined by x-ray measurements, J_{max} the current density at the maximum output power, and V_{th} the operating voltage at threshold. Values for J_{th} , J_{max} , V_{th} , and dP/dI are for $T \leq 10$ K.

of the highly doped bottom contact layer (sheet resistance of 20–30 Ω/\square) and the lateral gap of 20 μm between laser ridge and lower contact metallization cause a series resistance of 0.5–0.8 Ω for a 1.3 mm long laser ridge, which accounts for 0.1–0.2 V at the threshold.

4.2 Influence of growth variations on the lasing characteristics

To evaluate the impact of the doping level on the performance of THz QCLs based on the presented active-region design, a series of six wafers was grown with nominal identical growth sequences except for the doping level of the active region. For this series, the optical monitoring was not used for the in-situ growth control, and the post-growth x-ray data revealed a deviation of the average period length within $\pm 6.5\%$ of the nominal values due to the calibration error of the Ga effusion cell. For comparison, and since some irregularity during the growth of one the samples M4-2235 was anticipated, three wafers with the identical nominal doping density of $4.25 \times 10^{10} \text{ cm}^{-2}$ were grown (M4-2235, M4-2243, M4-2326). The C - V characterization revealed different doping levels for each of these samples, which was probably caused by a problem with the temperature control of the Si effusion cell (the Si cell was replaced by a new one later).

In Tab. 4.1, the results of the doping series are summarized. Data referring to the QCL characteristics are obtained from measurements of the temperature-dependent L - I - V characteristics and from the lasing spectra of QCLs with similar ridge dimensions (200 μm ridge width, 3.3–3.6 mm ridge length). Within the nominal doping range of $(5\text{--}11) \times 10^{10} \text{ cm}^{-2}$, there are no obvious trends for the QCL properties with increasing doping level. Within this range, the threshold current density varies within 175–370 A cm^{-2} . In contrast to the rather large variation of J_{th} , there are only small differences of T_{max} .

Furthermore, there is no correlation between the doping density and the peak output power P_{peak} , which differs within a factor of two, as well as the slope efficiency dP/dI at threshold. Obviously, the QCL properties for this active-region design do not depend sensitively on the doping level as a single parameter in this range. Only for the highest doped sample with $n_{\text{dop}} = 2 \times 10^{11} \text{ cm}^{-2}$, a significant increase of the threshold current density to 840 A cm^{-2} is found along with a significantly smaller T_{max} value of 90 K.

By taking into account the deviations of the average period length in the numerical simulation of the active region, the different emission ranges are qualitatively reproduced. However, the rather large variation of the threshold current densities is not reproduced in the simulated $J(F)$ characteristics. Since the experimental J_{th} and J_{max} values appear to be correlated, the formation of parasitic current channels, which are out of the scope of the transport model, seems to be a reasonable explanation. This might be a consequence of a complex interplay between the dynamic dipole formation around the doped quantum well, which is caused by the different distribution of ionized donors and electrons (cf. Fig. 4.1) and the formation of parasitic current channels via excited subband states.

For all samples, the operating voltage at threshold V_{th} is close to the limit given by Eq. (4.1) with the exception of sample M4-2247, for which V_{th} is even below that limit.

For this active-region design, the alignment of the extraction/injection miniband is related to a kink in the I - V characteristics at about 4 V [cf. Fig. 4.3(a)], and lasing starts typically in the flat region above that kink. For sample M4-2247, the threshold is slightly below that kink, which indicates that the injection/extraction miniband is not yet aligned for all periods. This might also explain the high slope efficiency for this sample, since the number of periods, which contribute to lasing, increases above threshold.

4.3 Conclusions

Based on an active-region design, which involves LO phonon-assisted transitions for an efficient electron injection, THz QCLs emitting around 3 THz with high output powers and low operating voltages are realized. As a consequence of using single-plasmon waveguides, the levels of output power are well above the typical sub-mW values obtained for THz QCLs based on metal-metal waveguides [42].

A similar active-region approach based on a period with seven quantum wells has been reported by Scalari *et al.* [67]. While the threshold current densities for pulsed operation of samples M4-2243 and M4-2247 are comparable to the data reported in this reference, the maximum cw operating temperature for single-plasmon devices is increased by 25 K due to the reduced operating voltage and hence a reduced heating of the active region. Compared to the bound-to-continuum active-region designs of Barbieri *et al.* [68] and Ajili *et al.* [69], which are not based on LO phonon-assisted transitions, the maximum pulsed operating temperature is significantly increased (for the best sample M4-2243 by 24 K and 15 K, respectively). However, the maximum cw operating temperature is not higher as compared to the reported values in these references (70 and 67 K, respectively), which appears to be due to a stronger active-region heating during cw operation in consequence of a larger driving power of the present QCLs. A cw operating temperature above 80 K for single-plasmon QCLs of the samples M4-2243 and M4-2247 appears possible, but would require a better heat sinking such as epi-side-down mounting to reduce the thermal resistance.

4 Low-voltage, high-power THz QCLs emitting around 3 THz

Operating a laser ridge of sample M4-2243 in a small-size Stirling cooler, a cw output power of 8 mW was obtained as well as a Gaussian beam profile [66], which are promising features for the use of similar THz QCLs as local oscillators in heterodyne experiments. One drawback of the presented nine-quantum-well active-region design appears to be the difficult predictability of the QCL properties such as the threshold current density. This might be a consequence of the complex interplay between the dynamic dipole formation close to the injection barrier and the alignment of subbands at a certain applied bias.

5 Low-threshold THz QCLs based on GaAs/Al_{0.25}Ga_{0.75}As heterostructures

Most of the THz QCL structures reported in the literature rely on GaAs/Al_xGa_{1-x}As heterostructures with a rather small Al content of $x = 0.10$ – 0.15 in the barriers [6, 42, 70]. The Al content determines the conduction band offset in the heterostructure and by that the maximum energy for the confined subbands (cf. Section 2.1). A smaller Al content allows for the use of thicker barriers resulting in a better control of the MBE growth. However, for MIR QCLs based on GaAs/Al_xGa_{1-x}As, it has been found that a high Al content is crucial to obtain high operating temperatures. Page *et al.* [71] have first obtained room temperature operation for GaAs-based MIR QCLs by using an Al content of $x = 0.45$ for the barriers of the active-region heterostructure, while before that usually $x = 0.33$ had been used. They explained this improvement by a reduced scattering of confined electrons into continuum states due to the increase of the conduction band offset by 95 meV. The operation of a MIR QCL based on purely binary GaAs/AlAs heterostructure has also been reported [72]. However, due to the onset of negative differential resistance, the operation was limited to cryogenic temperatures, even though the QCL showed a comparatively high characteristic temperature of $T_0 = 320$ K.

To examine the role of the barrier composition on the performance of THz QCLs, structures with an Al content of $x = 0.25$ in the barriers have been investigated. In such structures, the conduction band offset between the wells and barriers ΔV_c is increased by about 80 meV as compared to an Al content of $x = 0.15$. Due to this increased conduction band offset, possible leakage currents due to thermally activated scattering of electrons into continuum states are expected to be suppressed.

5.1 Influence of the barrier composition on the electronic transport

By increasing the barrier height, the coupling of subband states centered in different quantum wells is reduced. There are two limiting cases for the electronic transport, in which the influence of the barrier height can be treated analytically. One case is the transport within the minibands of a superlattice, which is expected to be a reasonable approximation for the transport within the quasi miniband in the injector region of many QCLs. The other limiting case is resonant-tunneling transport across the injection barrier, for which analytic results exist for the coupling of a single injector state with the upper laser level [27, 49].

Scattering-induced intraminiband transport has been discussed in Section 2.3.3 for the lowest miniband of a superlattice. In the low-temperature limit ($k_B T \ll \Delta$), Eq. (2.18) results in a linear dependence of the current density on the miniband width at a constant

field strength, i.e. $J_1/J_2 = \Delta_1/\Delta_2$. In the high-temperature limit ($k_B T \gg \Delta$), this becomes a quadratic dependence, i.e. $J_1/J_2 = (\Delta_1/\Delta_2)^2$. In order to apply Eq. (2.18) to the extraction/injection miniband of a THz QCL, a superlattice with 12 nm well width and 2.5 nm thick barriers is assumed, which corresponds to the average layer thicknesses of the THz QCL structure discussed in the previous chapter. For $x = 0.15$, a width of $\Delta = 11$ meV is obtained for the lowest miniband, while $\Delta = 7$ meV for $x = 0.25$. The corresponding current density ratios in the low- and high-temperature limit are 1.6 and 2.5, respectively. For a temperature of 100 K, Eq. (2.18) results in a value of 2.4, close to the high-temperature limit.

If the transport is limited by resonant tunneling from a single injector state into the upper laser level, the current density is given by [27]

$$J = en_{2D} \frac{\Omega_s^2 \tau_{\text{deph}}}{1 + (\Delta_{i-u}/\hbar)^2 \tau_{\text{deph}}^2 + \Omega_s^2 \tau_u \tau_{\text{deph}}}, \quad (5.1)$$

where Ω_s denotes the splitting frequency, i.e. the frequency which corresponds to the energy separation at the anticrossing resonance of the injector state and the upper laser level. Δ_{i-u} denotes the energy detuning from this resonance, τ_{deph} the dephasing time related to the intrasubband relaxation, and τ_u the total lifetime of the upper laser level. In the case of weak injection ($\Omega_s^2 \tau_u \tau_{\text{deph}} \ll 1$), the maximum current density ($\Delta_{i-u} = 0$) scales as $J_{\text{max},1}/J_{\text{max},2} = \Omega_{s,1}^2/\Omega_{s,2}^2$. To estimate this ratio, a double quantum well is considered with a barrier width of 4 nm and quantum well widths of 12 nm, approximating the injection barrier and the adjacent quantum wells of the active region discussed in the previous chapter. Splitting energies of 2.53 meV ($x = 0.15$) and 1.28 meV ($x = 0.25$) are obtained for the lowest doublet, which would correspond to a variation of the maximum current density by a factor of four.

To obtain similar subband energies and wavefunctions for QCL structures with $x = 0.15$ and $x = 0.25$, the thicknesses of the barriers have to be rescaled. Such a rescaled QCL structure should exhibit a similar coupling in particular of those subbands, which are mainly involved in the electronic transport and lasing. A quantitative scaling relation is derived from the expression for the width of the lowest miniband Δ in a superlattice, which is given in the tight-binding limit by [21]

$$\Delta \propto \exp\left(-L_B \sqrt{\frac{2m^*}{\hbar^2} \Delta V_c}\right), \quad (5.2)$$

where L_B denotes the barrier width. From Eq. (5.2), the following scaling relation is directly obtained

$$\frac{L_{B,1}}{L_{B,2}} = \sqrt{\frac{\Delta E_{c,2}}{\Delta E_{c,1}}}, \quad (5.3)$$

where 1 and 2 refer to the Al content of $x = 0.15$ and $x = 0.25$, respectively. By applying Eq. (5.3), similar subband energies and wavefunctions are obtained for the lowest subbands with increasing deviations as the subband energies increase toward the barrier band edge.

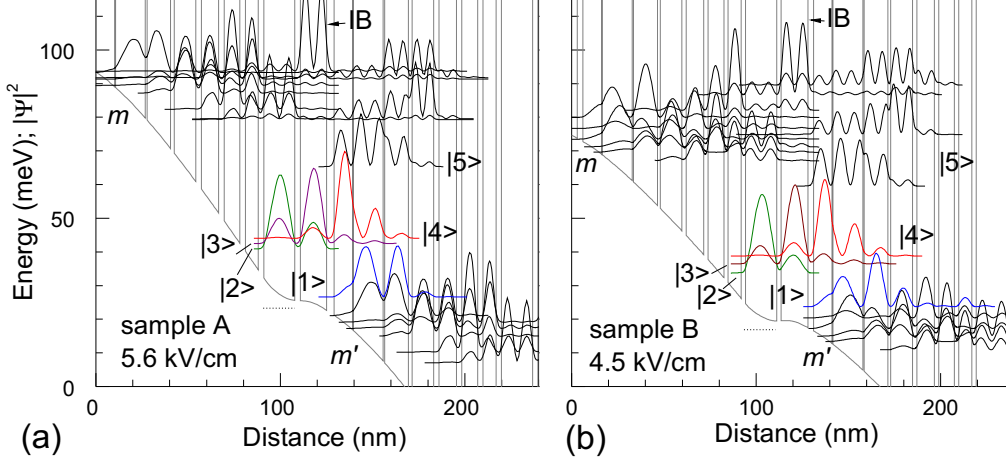


Figure 5.1: Calculated conduction band profile and squared moduli of the wavefunctions for the active-region period of (a) sample A (M4-2340) and (b) sample B (M4-2342) at their respective threshold bias. The doped quantum well is indicated by the horizontal dotted line.

5.2 Experimental results and discussion

For the experiments, the nine-quantum-well active-region design discussed in the previous chapter has been chosen as a starting point. Two additional samples have been grown. For sample M4-2340 (labeled sample A in this chapter), the same nominal active-region sequence has been used, except for the Al content in the barriers, which has been increased to $x = 0.25$. In addition to that, the barrier thicknesses in sample M4-2342 (labeled B in this chapter) have been reduced by about 30% according to Eq. (5.3). No significant deviations were found by x-ray measurements as compared to the nominal sequences. The doping densities as determined by C - V measurements are $9.2 \times 10^{10} \text{ cm}^{-2}$ for sample A and $8.3 \times 10^{10} \text{ cm}^{-2}$ for sample B, which are close to the nominal doping density of $8.5 \times 10^{10} \text{ cm}^{-2}$ for both samples. The growth sequences of these samples are given in the Appendix. For a quantitative comparison of the laser parameters, the sample of the original series, which is closest to sample A in terms of layer thicknesses and doping density (M4-2239), is referred to as sample R. In Figs. 5.1(a) and 5.1(b), the results of band structure calculations are shown for samples A and B at their respective threshold bias. The band structures are qualitatively very similar to the one of sample R (cf. Fig. 4.1). Therefore, the intersubband transport channels should be in principle the same as for the original design as well as the mechanism of intersubband gain. There are certain qualitative differences such as that the energy splitting of the injector states $|2\rangle$ and $|3\rangle$ and the upper laser level $|4\rangle$ is smaller in sample A due to a reduced coupling of subband states as compared to sample B. The energy of the lasing transition $|4\rangle \rightarrow |1\rangle$ is higher in sample A because of the higher threshold field strength. There are additional

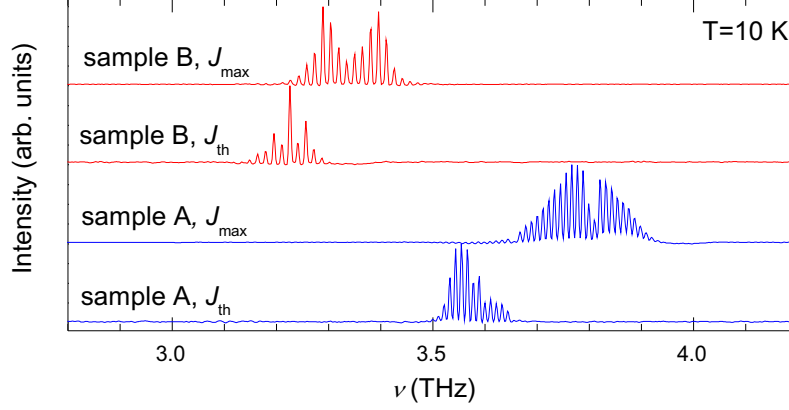


Figure 5.2: Lasing spectra of sample A ($0.2 \times 2.5 \text{ mm}^2$ laser ridge) and sample B ($0.2 \times 3.4 \text{ mm}^2$ laser ridge) for pulsed operation (500 ns, 5 kHz) at current densities close to J_{th} and J_{max} at 10 K.

small differences in the alignment of the extraction/injection miniband (m, m') and of the excited subband states to the right of the injection barrier.

The lasing spectra for samples A and B are shown in Fig. 5.2 for a current density close to J_{th} and close to the maximum output power (J_{max}) of the respective lasers. The rescaled sample B emits in the range of 3.2–3.4 THz, which is within the emission ranges obtained for the original series such as 3.3–3.6 THz for sample R. The emission of sample A occurs at higher frequencies in the range of 3.5–3.9 THz. This is in agreement with the higher threshold field strength in sample A, which accounts for a 2.5 meV (0.6 THz) increase of the laser transition energy as compared to sample B according to the calculation shown in Fig. 5.1. The blue shift of the emission spectra between threshold and maximum output power is a consequence of the spatially diagonal laser transition, which causes a linear Stark shift. Indeed, it is found that the central lasing frequency depends almost linearly on the operating voltage even for different operating temperatures. The linear Stark shift results for sample A in a remarkably large total lasing range of almost 400 GHz.

In Fig. 5.3(a), the threshold current density for pulsed operation is depicted as a function of temperature for samples A, B, and R ($0.2 \times 3.5 \text{ mm}^2$ laser ridges). The gray shaded area refers to the total data range of the original series with $x = 0.15$, except for the sample with the highest doping level (M4-2325). At 10 K, J_{th} for sample A is as low as 70 A cm^{-2} as compared to 235 A cm^{-2} for sample B and 295 A cm^{-2} for sample R. While J_{th} of sample B is significantly below the value of sample R, it is still within the rather large range of the original series. In contrast to that, the strongly reduced value for sample A is clearly an effect of the increased barrier height in this structure. Similar characteristic temperatures T_0 are found with values of 20.5, 26, and 23.5 K for samples A, B, and R, respectively. In contrast to the remarkably reduced threshold current density for sample A at low temperatures, its maximum pulsed operating temperature is reduced to 90 K as compared to 110 K for samples R and B. Since both, the T_0 value and the maximum operating temperature of the rescaled sample B, fall well into the range of the original series, it can

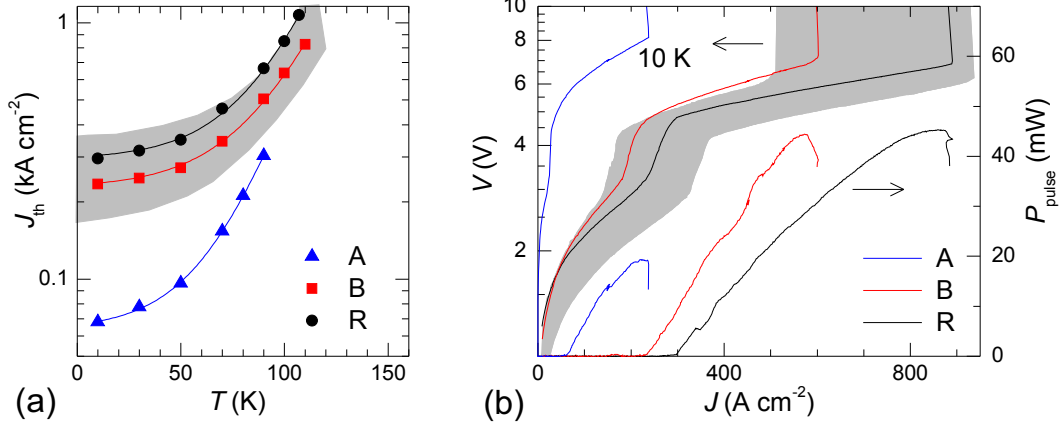


Figure 5.3: (a) Temperature dependence of the threshold current density (logarithmic scale) for samples A, B, and R for pulsed operation with 500 ns and 5 kHz ($0.2 \times 3.4 \text{ mm}^2$ laser ridges). (b) $L-I-V$ characteristics of the same laser ridges at 10 K (logarithmic voltage scale).

be concluded that thermally assisted scattering of electrons into continuum states does not result in significantly enlarged leakage currents in the QCLs with $\text{Al}_{0.15}\text{Ga}_{0.85}\text{As}$ barriers.

In Fig. 5.3(b), the $L-I-V$ characteristics for pulsed operation are shown for samples A, B, and R at 10 K. The gray shaded area refers to total $I-V$ data range of the original series, except for the sample with the highest doping level. The $I-V$ characteristics of sample B fits into the rather large variation of the original series, but the current densities in sample A are much smaller, while the voltages during operation are significantly higher. Samples B and R have comparable levels of peak output power P_{peak} with values of about 45 mW at $J_{max} = 570 \text{ A cm}^{-2}$ in sample B and $J_{max} = 870 \text{ A cm}^{-2}$ in sample R. In contrast, the peak output power of sample A is only 19 mW at $J_{max} = 225 \text{ A cm}^{-2}$, which can be ascribed to the onset of NDR at rather low current densities in this sample. The slope efficiencies at threshold are 24.5 mW/A for sample A, 21 mW/A for sample B, and 16 mW/A in sample R. Hence, the reduced peak output power of sample A is not related to a reduced internal quantum efficiency.

Despite the limited output power and temperature range of sample A during pulsed operation, cw lasers have been obtained from that wafer with output powers of a few mW. The lasing parameters for a $0.1 \times 1.0 \text{ mm}^2$ laser ridge of wafer A are a maximum operating temperature of 47 K, a maximum output power at 10 K (40 K) of 2.5 mW (1 mW), and values for J_{th} of 132 A cm^{-2} (183 A cm^{-2}), which would be still sufficient for applications such as heterodyne spectroscopy. The cw electrical driving power at threshold is just 0.8 W at 10 K, which is well below the threshold driving power obtained for similar lasers with $\text{Al}_{0.15}\text{Ga}_{0.85}\text{As}$ barriers. From a comparison of the $J_{th}(T)$ characteristics for pulsed and cw operation, a thermal resistance of 9.3 K/W is found, similar to the value discussed in the previous section. Due to the small driving power, the effective active-region temperature during cw operation does not increase by more than 20 K above its value during pulsed operation.

The strong reduction of the current densities as found for sample A is in qualitative agreement with both analytic models, the scattering-induced miniband transport within the extraction/injection miniband as well as the model of resonant tunneling across the injection barrier. It is a consequence of the reduced tunneling probability through the barriers. However, the strong reduction of J_{th} in sample A is not directly obvious, since this requires an increase of the differential gain \tilde{g} in Eq. (2.26). The differential gain is affected for instance by parasitic currents. Parasitic current channels are the non-radiative injection of electrons into the lower laser level and the bypass via parasitic states such as state $|5\rangle$ in Figs. 5.1(a) and 5.1(b). A reduction of the first channel would increase the injection efficiency η_3 into the upper laser level and reduce the injection efficiency η_2 into the lower laser level, while a reduction of the latter would increase $\eta_3 + \eta_2$. Both would result in a smaller threshold current density and an increased slope efficiency according to Eqs. (2.33) and (2.35). Such parasitic channels would also explain the increased value of J_{th} and the decreased value of the slope efficiency of sample R as compared to sample B.

The different threshold current densities of samples A and B are qualitatively reproduced by numerical simulations of the active region based on the one-dimensional transport model. The threshold current density can be determined by the condition for lasing, i.e. $\Gamma g = \alpha_m + \alpha_w$. For the $0.2 \times 3.5 \text{ mm}^2$ laser ridges, a threshold gain of $(\alpha_m + \alpha_w)/\Gamma = 30 \text{ cm}^{-2}$ is assumed. In addition, the inhomogeneous level broadening was set to 0.5 meV. The calculated threshold current densities for samples B and A are 120 and 80 A cm^{-2} , respectively, suggesting a reduction of J_{th} for sample A by about a factor of 1.5 as compared to sample B [58]. The stronger experimental deviation by a factor of three might be in part a consequence of the electron dephasing involved in the resonant-tunneling process. Since this is a collective effect, it is not considered in the rate-equation-based transport simulations. Neglecting the electron dephasing is likely to result in an overestimation of resonant-tunneling currents, in particular for small splitting energies as obtained by an increase of the barrier heights. However, Eq. (5.1) cannot be applied to this particular active-region design, since there are not one but two injector states, which is beyond the scope of the density matrix model [27], for which this equation has been derived.

5.3 Conclusions

By increasing the Al content in the barriers from $x = 0.15$ to $x = 0.25$, the threshold current density for a particular QCL structure could be significantly reduced, but for the sake of smaller output powers and higher operating voltages. By readjusting the barrier thicknesses in order to account for the increased barrier height, similar properties for QCLs with $x = 0.15$ and $x = 0.25$ have been obtained. Hence, the experimental results confirm for x values between 0.15 and 0.25 that the Al content is indeed a degree of freedom for the design of THz QCLs. Since the subband energies close to the barrier and quantum well band edge shift differently with the value of x , this parameter might be exploited in the case of an unfavorable alignment of subbands. Such an example is the reabsorption of emitted photons caused by higher-energy states above the upper laser level. By changing the quantum well thicknesses and the Al content, higher-energy states might be shifted, while the different effects just compensate for the laser transition energy. While Al contents of $x > 0.25$ have not been investigated, the practical use of larger x values is restricted at

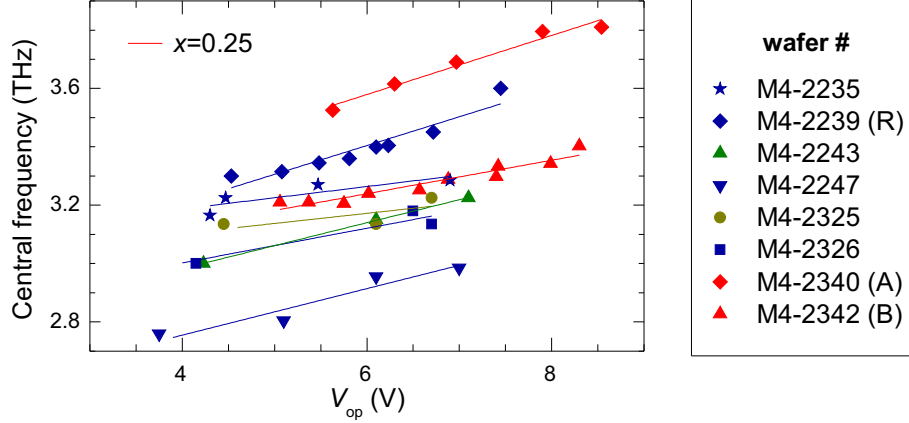


Figure 5.4: Central frequency vs. operating voltage for samples A and B as well as for all samples of the original series with $x = 0.15$.

a certain point by the required small barrier widths in the monolayer and sub-monolayer range. Another aspect, which should be kept in mind, is the rather strong dependence of the threshold current density on the Al content, in particular since the Al content cannot be confirmed with a sufficient precision by x-ray measurements.

In Fig. 5.4, the central emission frequency is plotted versus the operating voltage for samples A and B as well as for all samples of the original series with $\text{Al}_{0.15}\text{Ga}_{0.85}\text{As}$ barriers. Linear dependencies are found for the frequency shift with voltage, which is explained by the linear Stark effect. The total emission range spans 2.7–3.9 THz with a typical range of 200–350 GHz for each sample. The broad emission ranges, the rather high levels of output power, and the small operating voltages are promising features of this type of design. However, the wafer-to-wafer variation of the threshold current density as well as the wafer-to-wafer variation of the particular emission range impose a significant challenge for the development of THz QCLs, which have to operate in continuous-wave mode at a specified target frequency.

6 THz QCLs for emission above 4 THz

For far-infrared astronomy, a particular important emission line is the fine structure transition ${}^3P_1-{}^3P_2$ of neutral atomic oxygen (OI) at 4.7448 THz, since it is believed to be one main coolant channels for the interstellar medium [73, 74]. One goal of the current SOFIA mission (stratospheric observatory for far-infrared astronomy) is the heterodyne detection of this transition, which requires a local oscillator at a frequency, which is just a few GHz above or below the OI transition. To use a THz QCL as the local oscillator, several challenges have to be solved. One main challenge is the active-region heterostructure, which has to provide a combination of gain around the target frequency and an electrical driving power and operating temperature range, which allows for cw operation in small cryocoolers or in a liquid nitrogen dewar. Another main challenge is the single-frequency operation at one of the specified upper- and lower-sideband frequencies for the local oscillator, which will be subject of Chapter 7.

In this chapter, the focus is on general experimental results for a particular active-region design developed for emission above 4 THz and its modifications toward an optimized performance. The goal has been the development of an active-region heterostructure for emission around 4.75 THz to be used for single-frequency THz QCLs based on DFB gratings or external cavity resonators. In the first part of this chapter, the basic active-region design and the results of a doping series are presented, where the focus will be on the general pulsed-mode characteristics (cw operation and particular nonlinear transport effects are discussed in Chapter 8). Subsequently, several design modifications toward an optimized performance are discussed as well as the variation of laser parameters across a wafer.

6.1 Basic active-region design for emission above 4 THz

The basic active-region design is comparable to the LO phonon-assisted injection design discussed in Chapters 4 and 5. As for the active-region designs discussed above, nine quantum wells are used, which provide an extraction/injection quasi-miniband and a doublet of injector states coupled to the upper laser level. The larger laser transition energies above 4 THz as compared to 3 THz cause a general trend toward higher energies of the involved subbands. To account for this trend, an Al fraction of $x = 0.25$ has been used for the barriers, which improves the electronic confinement of higher-energy subbands as compared to $x = 0.15$.

In Fig. 6.1(a), the result of a band structure calculation is shown for the basic active-region design labeled TIX3. As a main difference to the previous designs, the single injection barrier is changed into a double barrier (labeled 1 and 2) to increase the separation between the higher-energy state $|5\rangle$ and the upper laser level $|4\rangle$. In this way, absorption at the frequency of the laser transition is avoided. Figure 6.1(b) depicts the cal-

6 THz QCLs for emission above 4 THz

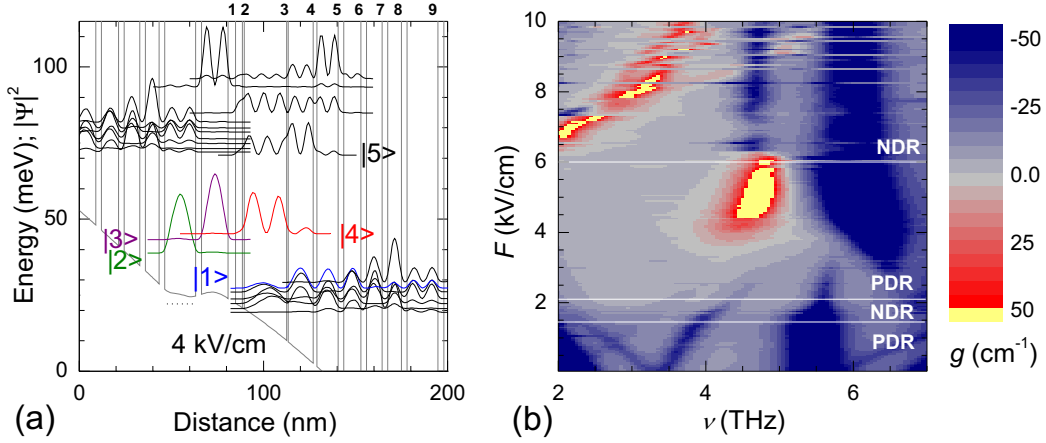


Figure 6.1: (a) Calculated conduction band profile and squared moduli of the wavefunctions at 4 kV/cm for the design labeled TIX3. The doped quantum well is indicated by the horizontal dotted line ($n_{\text{dop}} = 2 \times 10^{11} \text{ cm}^{-2}$). For the discussion of design modifications, the barriers have been numbered. (b) Calculated gain vs. field strength and frequency for this design. Horizontal white lines separate regions of positive (PDR) and negative (NDR) differential resistance.

culated gain characteristics for this structure. While the laser transition (with the upper level $|4\rangle$) is responsible for the gain region between 4 and 5 THz, the absorption between 5 and 7 THz is caused by the transition $|4\rangle \rightarrow |5\rangle$. This points also to the importance of including the higher-energy subband states into the simulations. While the $|4\rangle \rightarrow |5\rangle$ transition causes a strong absorption region, it is not involved in the electronic transport below threshold.

In the momentum-independent transport model, the effect of a non-vanishing electron temperature is simulated by assuming a finite transition rate if the subband energy of the final state is above the initial state. A finite electron temperature can cause the presence of gain even below the low-temperature limit for the operating bias as imposed by Eq. (4.1). At $F = 4 \text{ kV/cm}$, the electrons require a kinetic energy of about 6 meV to be injected from level $|2\rangle$ into the upper laser level $|4\rangle$, which corresponds to a temperature value $T = E/k_B$ of approximately 70 K. Due to the transfer of kinetic into potential energy, such a transition might be regarded as an electronic cooling channel for the system. The numerical simulation further reveals several gain regions above 6 kV/cm. However, this gain cannot be exploited by electrical pumping due to the NDR regime above this field strength indicated in Fig. 6.1(b). The simulation of the active region has been repeated for different sheet doping densities. In Fig. 6.2(a), the maximum gain below 6 kV/cm is plotted vs. the frequency. The peak gain is found at 4.75 THz and does not shift with the doping concentration. In Fig. 6.2(b), the gain at 4.75 THz is plotted vs. the field strength for different doping concentrations. With increasing doping concentration, a small increase of the value of the peak gain is found as well as a shift to smaller field strengths. This result suggests that the doping density is not a sensitive parameter for THz QCLs based on this active region. However, several doping dependent effects are not

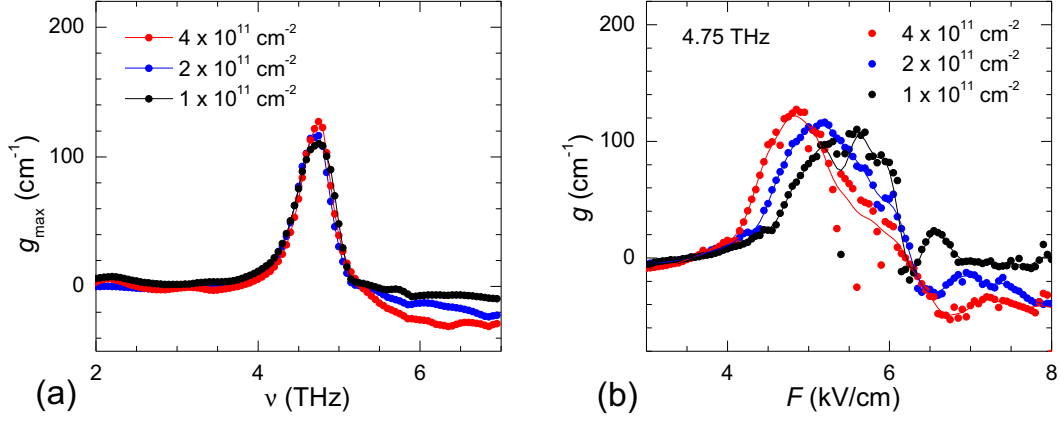


Figure 6.2: (a) Calculated gain maximum (for $F \leq 6$ kV/cm) vs. frequency for different sheet doping densities per period. (b) Calculated gain at 4.75 THz vs. field strength. Solid lines are guides to the eye.

taken into account in the simulations such as electron-impurity scattering [75] and the potential increase of waveguide losses due to free-carrier absorption for high doping levels.

6.1.1 Experimental results of a doping series

A series of four wafers has been investigated to clarify the impact of the doping level for this active-region design. The doping densities are in the range of $(0.8\text{--}5) \times 10^{11} \text{ cm}^{-2}$ per period. Except for one wafer, which showed a rather large deviation of the average period length of 6%, all wafers are within a deviation of $\Delta d/d_0 \leq 1.5\%$ with respect to the nominal sequence. Figures 6.3(a) and 6.3(b) depict exemplarily for one of the samples (M4-2404) the pulsed-mode L - I - V characteristics and lasing spectra, respectively. For that sample, the doping level is $2 \times 10^{11} \text{ cm}^{-2}$. Lasing operation up to 70 K is obtained with a peak output power of about 5 mW at low temperatures and a threshold current density of only 50 A cm^{-2} for a $0.2 \times 3.3 \text{ mm}^2$ laser ridge. The QCL emits in the range of 4.0–4.2 THz, and the presence of a Stark shift for increasing bias confirms the diagonal nature of the laser transition, which is in agreement with the simulations. In Tab. 6.1 the results of a characterization for QCLs from the central region of each wafer are summarized. Compared to the THz QCL design discussed in Chapter 4, the low-temperature threshold current densities of these QCLs are remarkably smaller, even for the sample with the highest doping level. However, also the maximum operating temperatures are smaller, and the peak output power is reduced by about one order of magnitude, which is accompanied by much smaller dynamic current ranges of the present series. While the calculated gain maximum is found at 4.75 THz, the experimental spectra reveal somewhat smaller emission frequencies in the range of 4.0–4.45 THz.

There are several quantitative differences between the samples of this series, which are likely to be related to the doping density. J_{th} increases by a factor of 1.6 from the lowest to the highest doping density with a value of only 50 A cm^{-2} for the two samples with the

6 THz QCLs for emission above 4 THz

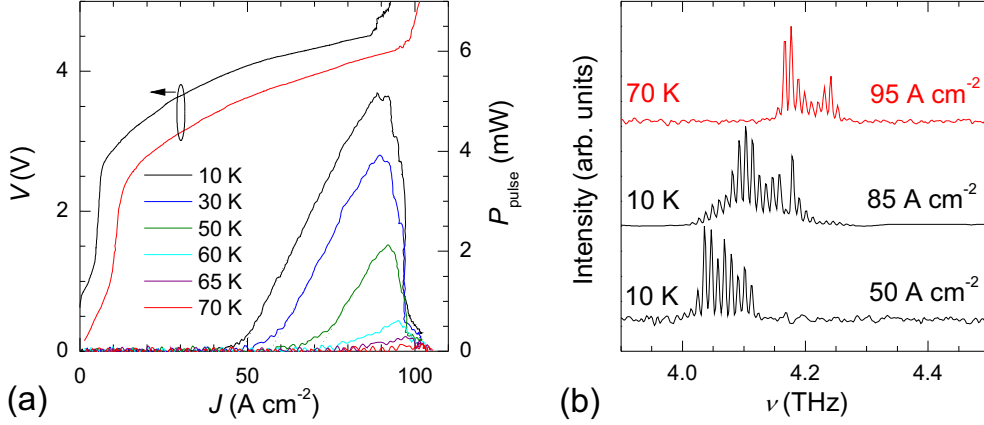


Figure 6.3: (a) Measured L - I - V characteristics under pulsed operation for sample M4-2404 (0.2×3.3 mm² laser ridge, 500 ns, 5 kHz). The nonlinear power dependence at threshold is artificial due to the shape of the electrical driving pulse at small current amplitudes. J_{th} is determined by extrapolation of the linear part of the output power characteristics toward the abscissa as indicated by the dotted lines. (b) Lasing spectra of this device for different operating conditions.

Sample No.	M4-2397	M4-2404	M4-2421	M4-2429
n_{dop} (10^{11} cm ⁻²)	0.8 (1.0)	2.0 (2.0)	3.95 (4.0)	4.7 (4.0)
$\Delta d/d_0$ (%)	-1.5	+1	+6	+0.7
T_{max} (K)	50	70	45	70
J_{th} (A cm ⁻²)	50	50	65	80
J_{max} (A cm ⁻²)	70	90	95	215
V_{th} (V)	4.75	4.1	3.15	3.55
P_{peak} (mW)	2	5	2	7.5
dP/dI (mW/A)	15	20	11	12
ν (THz)	4.32–4.44	4.05–4.26	3.99–4.14	4.23–4.44

Table 6.1: Sample properties for the doping series of the basic 4.7 THz active-region design. Doping densities are determined by C - V measurements (nominal values in brackets). The laser characteristics are measured for $0.2 \times 3.3 \dots 3.5$ mm² laser ridges under pulsed operation with 500 ns and 5 kHz. The values for J_{th} , J_{max} , V_{th} , and dP/dI are determined at 5 K (10 K for sample M4-2404).

lowest and second-lowest doping level. The same trend is found for J_{max} , which increases by a factor of 3. Except for sample M4-2421, also an increase of the maximum pulsed output power P_{peak} with increasing doping density is found, which is correlated with an increase of the dynamic range $J_{\text{max}} - J_{\text{th}}$. The operating voltage at threshold V_{th} decreases with increasing doping density, which is consistent with a predicted shift of the gain peak toward lower field strengths by the numerical simulation. Sample M4-2421, for which a rather large deviation from the nominal sequence was found, does not seem to fit into this

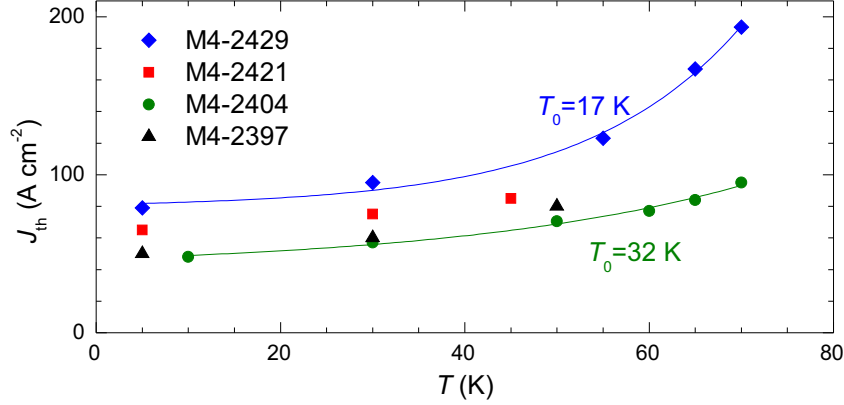


Figure 6.4: Temperature dependence of the threshold current density ($0.2 \times 3.3 \dots 3.5 \text{ mm}^2$ laser ridges, pulsed operation with 500 ns, 5 kHz). The solid lines depict the phenomenological fit to $J_{th} = J_0 + J_1 \exp(T/T_0)$.

series in terms of maximum operating temperature and peak output power. However, by taking the deviation from the nominal sequence into account in the numerical simulations, a reduction of the peak gain by 35% and a shift of the NDR onset from 6 to 4.2 kV/cm has been calculated, which explains the rather small dynamic range and maximum operating temperature of this sample and illustrates the rather strong influence of small structural differences on the QCL characteristics.

Figure 6.4 depicts the $J_{th}(T)$ characteristics of the different samples. While T_{max} is the same for samples M4-2404 and M4-2429 (70 K), the difference of J_{th} between these two samples is accompanied by a difference in the characteristic temperature T_0 of about a factor of two. Since in addition to the experimental value of T_{max} also the calculated value of the peak gain is similar for both samples, free-carrier absorption losses caused by the higher doping level in sample M4-2429 seems to play only a minor role.

6.1.2 Discussion

For the present design, a doping level optimum appears to be around $2 \times 10^{11} \text{ cm}^{-2}$. For this doping density, the lowest threshold current density, the highest operating temperature and the highest characteristic temperature T_0 are found. However, the dependence of the QCL performance on the doping density is rather weak, such as a variation of J_{th} by a factor of 1.6 for a variation of the doping density by a factor of 4. Obviously, the impact of MBE growth variations (such as for sample M4-2421) can exceed the effect of the doping level itself, which has been also found for the QCL design discussed in Chapter 4. Comparing the experimental results for the different designs, it becomes obvious that the range of suitable doping densities depends on the particular active-region design. While for the QCL design discussed in Chapter 4 a sheet doping density of $n_{dop} = 2 \times 10^{11} \text{ cm}^{-2}$ resulted already in a significantly degraded performance, more than twice that doping level yields still threshold current densities as low as 80 A cm^{-2} for the present design. We believe that the remarkable insensitivity to the doping density of the present design

as compared also to reported results for other designs [76, 77, 78] is related to the field screening and the formation of a local dipole in front of the injection barrier [cf. Fig. 6.1(a)]. This dipole, caused by the different distribution of ionized donors and electrons, might be regarded as a buffer, which allows for a self-alignment of the extraction/injection miniband. In contrast, the alignment of the wavefunctions is not affected by local space charge in the case of a quasi-constant electric field strength, for which the current density becomes proportional to the doping level [78].

Different results for the impact of the doping density on the performance of THz QCLs are reported in Refs. [76, 77, 78]. Lasing operation for much smaller sheet doping densities between $(0.5\text{--}2)\times 10^{10}\text{ cm}^{-2}$ is reported in Ref. [78] for a four-quantum-well *resonant-phonon* active-region period. The increase of the doping density by a factor of 3.5 resulted in the same relative increase of J_{th} with a linear slope. In Ref. [76], the increase of the doping density from 3.2 to $4.8\times 10^{10}\text{ cm}^{-2}$ for a similar *resonant-phonon* design resulted in an increase of J_{th} by a factor of 3 with a strongly nonlinear slope. In Ref. [77], an increase of J_{th} by a factor of 2 has been obtained for a *bound-to-continuum* active region for a doubling of the doping density from 4.4 to $8.8\times 10^{10}\text{ cm}^{-2}$. The variety of different results confirms that the optimum doping range and the impact of the doping density depend sensitively on the particular active-region design.

The low-temperature threshold current densities of the present design are among the smallest reported for THz QCLs. In Ref. [79], a smaller J_{th} of about 30 A cm^{-2} has been reported. However, this result has been obtained using a metal-metal waveguide with high-reflectivity coatings on both facets, which results in a significantly smaller threshold gain as compared to uncoated single-plasmon waveguides.

Another conclusion can be drawn about the electron temperature in the present THz QCLs. Since the operating voltages of the higher doped samples are already below the low-temperature limit as imposed by Eq. (4.1), the presence of electrons with significant in-plane momentum in front of the injection barrier is required to overcome the energy difference of about 6 mV at threshold between the lowest injector state and the upper laser level. For a different type of active region, Monte-Carlo simulations including the in-plane momentum have predicted electron temperatures of more than 100 K for the different subbands of the THz QCLs at a heat sink temperature of 5 K [80]. Such high temperatures would be consistent with the present results and also justify the use of finite scattering rates for negative transition energies as implemented in the effective one-dimensional transport model.

6.2 Design modifications

Besides the promisingly small values of J_{th} and V_{th} of the previously discussed QCLs, the rather small maximum operating temperatures and output powers limit the range of practical applications. For that reason, various modifications of the active-region design have been tested. One goal has been to extend the dynamic range $J_{\text{max}} - J_{\text{th}}$ of the QCLs. Since J_{max} is usually determined by the onset of NDR-related discontinuities in the I - V characteristics, design modifications, for which the numerical simulations resulted in a high field strength for the onset of NDR, are preferential. The other goal is to shift the emission frequency toward 4.75 THz.

6.2.1 Impact of local modifications of the barrier thicknesses

A series of three wafers was grown to investigate the impact of the injection barrier and the barriers in the extraction/injection region. In the following, the wafer numbers M4-2454, M4-2435, and M4-2455 refer to samples m1, m2, and m3, respectively. For sample m1, the thicknesses of the injection barrier 1 [cf. Fig. 6.1(a)] and the adjacent barrier 9 were reduced from 4 to 3 nm and 3.3 to 2.8 nm, respectively, which increases the coupling between the injector states and the upper laser level. For sample m2, also the thicknesses of several barriers in the extraction/injection region was reduced from 3 to 1.5 nm (barrier No. 3, 4, 5, 6, 7, 8). The same changes were applied to sample m3, but with the original thicknesses of the barriers 1 and 9. A doping density of $2 \times 10^{11} \text{ cm}^{-2}$ was used for all samples. The simulations revealed similar values for the peak gain and similar $J(F)$ characteristics below the onset of NDR for the unmodified and the modified designs. The onset of NDR above the gain region [cf. Fig. 6.1(b)] is shifted from 6 to 7 kV/cm for samples m2 and m3, which is expected to result in a larger dynamic current range for these samples.

The design modifications and the main experimental results are summarized in Tab. 6.2. While for sample m1 the value of T_{max} is increased to 90 K as compared to 70 K for the previous series, only a marginal increase to 75 K is found for sample m2, and no lasing at all is observed for sample m3. The barrier modifications resulted also in significantly larger threshold current densities of 125 and 330 A cm^{-2} at 5 K ($0.2 \times 3.5 \text{ mm}^2$ laser ridges) for samples m1 and m2, respectively. A large operating voltage with a V_{th} value of 7 V at 5 K is obtained for sample m2, while for sample m1 the V_{th} value of 4.3 V falls within the range of the previous series. The emission frequencies vary between 4.5–4.7 THz for sample m1 and 4.8–4.95 THz for sample m2, starting at the lower end of these ranges at threshold.

For sample m1, cw operation has been obtained up to a heat sink temperature of 63 K for a small-area laser ridge ($0.1 \times 1.13 \text{ mm}^2$). The electrical driving power of less than

Sample	m1	m2	m3	ref.
Barriers 9/1 (nm)	2.8/3.0	2.8/3.0	3.3/4.0	3.3/4.0
Barriers 3–8 (nm)	3.0	1.5	1.5	3.0
$\Delta d/d_0(\%)$	–4	–5	–4	
T_{max} (K)	90	75	—	
J_{th} (A cm^{-2})	125	330	—	
V_{th} (V)	4.3	7.0	—	
P_{peak} (mW)	10	6	—	
ν (THz)	4.5–4.7	4.85–4.95	—	

Table 6.2: Top: Barrier modifications of samples m1 to m3 as compared to the original design (ref.) and thickness deviations as determined by x-ray measurements. Bottom: Basic operating parameters for laser ridges from the central part of samples m1 to m3 (pulsed operation, $0.2 \times 3.5 \text{ mm}^2$ ridges). The values for J_{th} , V_{th} , and P_{peak} were determined at 5 K.

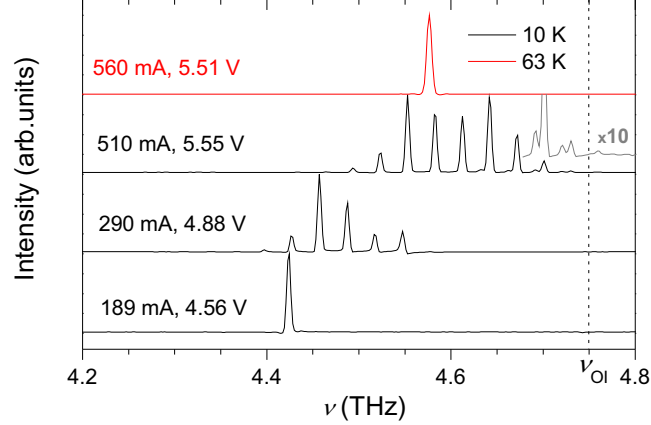


Figure 6.5: Continuous-wave emission spectra of a $0.1 \times 1.13 \text{ mm}^2$ laser ridge of sample m1 (M4-2454). The dashed line indicates the target frequency of the 3P_1 - 3P_2 OI transition.

3 W allowed for operation in a Stirling cooler. The maximum output power has been 5.5 mW at 20 K and 3 mW at 50 K, which is well above the specified 1 mW for heterodyne applications. Figure 6.5 depicts the cw lasing spectra. At low temperatures and operation at J_{\max} , the emission is centered around 4.59 THz, and rather weak Fabry-Pérot modes are observed at 4.697, 4.726, and 4.755 THz close to the OI frequency of 4.745 THz. At higher temperatures, the spectral range narrows significantly, and at T_{\max} a single mode appears at 4.573 THz. Hence, the important central frequency of the emission at J_{\max} is still about 4% off the target frequency. Very similar results have been obtained for two other cw laser ridges from the same wafer.

The absence of lasing for sample m3 can be attributed to a very small current density of 120 A cm^{-2} for the onset of the NDR-related discontinuities, a value which is below J_{th} for the other two samples. This illustrates the importance of a balance between the thicknesses of the injection barrier and the barriers in the extraction/injection region. In the present case of large thickness differences, the onset of NDR-related effects cannot be well predicted by the active-region simulations, and the presence of NDR eventually prevents reaching the lasing threshold.

6.2.2 Design modifications based on a double injection barrier

One weak point of the original design and the previous modifications m1–m3 is the very thin barrier 2 [cf. Fig. 6.1(a)], which has a rather large impact on the subband energy of the reabsorption state $|5\rangle$. To reduce the sensitivity with respect to the precision of the MBE growth, one strategy has been to increase the width of this barrier. Based on the nominal sequence of sample m1, the width of the three layers starting from barrier 1 have been changed from **3.0**/**3.7**/**1.0** nm for sample m1 to **1.7**/**3.1**/**1.3** nm in the modified design TAX8 (bold numbers refer to the barriers). In the design TAX9, this has been further changed to **1.5**/**3.5**/**1.5** nm. In both cases, additional small changes of the layer sequence have been necessary in order to shift the gain maximum toward the desired 4.75 THz and

to avoid that regions of strong gain and reabsorption occur at close-by frequencies. For both modifications, the simulations revealed similar characteristics as for the sample m1.

Samples M4-2478 and M4-2473, referred to as m4 and m5 in the following, belong to the TAX8 design and have been grown with doping densities of 1.3×10^{11} and 2.0×10^{11} cm^{-2} , respectively. Sample M4-2491 and M4-2540, referred to as m6 and m7, belong to the TAX9 design and have been grown with a doping density of 2.0×10^{11} cm^{-2} . Sample m7 has been used to test the reproducibility of the MBE growth after 7 months.

The modifications and experimental results are summarized in Tab. 6.3. The low-temperature threshold current densities and operating voltages are rather small for all of these samples, and the output powers and maximum operating temperatures of samples m4 and m5 are significantly increased as compared to the original design. However, the emission frequencies in the range of 4.2–4.6 THz are still off the target frequency of 4.75 THz. Continuous-wave lasers have been tested for samples m4 and m5. For sample m5, cw operation at 50 K has still been possible with an output power of 0.5 mW (0.1×1.45 mm² laser ridge). Thus, the changes applied to the active-region sequence of sample m1 did not result in significant improvements. In particular, QCLs operating at 4.75 THz could not be obtained. However, the good agreement of the properties of samples m6 and m7, which agree within the usual variation of QCL parameters for a single wafer, indicates a reasonable reproducibility of the MBE growth for this active-region design.

6.2.3 Design modifications based on a single injection barrier

A significant improvement of the lasing properties has been obtained by a further design modification. The barrier 2 involved in the double injection barrier has been omitted in favor of a single injection barrier resulting in an active-region period with eight quantum wells. Figure 6.6(a) depicts the calculated frequency and field dependent gain for this structure. The corresponding band structure for the operating field strength range of 4–6 kV/cm is still similar to the original design shown in Fig. 6.1(a). However, the parasitic

Sample	m4	m5	m6	m7
Injector seq. (nm)	1.7/3.1/1.3	1.7/3.1/1.3	1.5/3.5/1.5	1.5/3.5/1.5
n_{dop} (cm^{-2})	1.3×10^{11}	2×10^{11}	2×10^{11}	2×10^{11}
$\Delta d/d_0$ (%)	−1	−1	+2	+3
T_{max} (K)	95	90	70	70
J_{th} (A cm^{-2})	140	160	100	100
V_{th} (V)	4.6	4.0	3.8	4.3
P_{peak} (mW)	30	20	10	14
ν (THz)	4.2–4.5	4.3–4.6	4.3–4.5	4.3–4.5

Table 6.3: Top: Modified injector sequences with the barriers in bold (starting from the injection barrier 1), nominal doping density and thickness deviations as determined by x-ray measurements for samples m4 to m7. Bottom: Basic operating parameters for laser ridges from the central part of each sample (pulsed operation, 0.2×3.5 mm² ridges). The values for J_{th} , V_{th} , and P_{peak} were determined at 5 K.

6 THz QCLs for emission above 4 THz

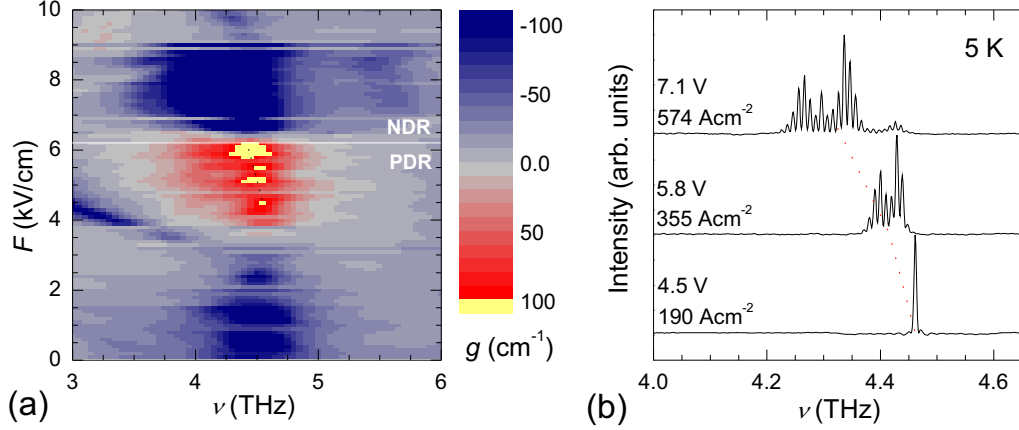


Figure 6.6: (a) Calculated gain vs. frequency and field strength for wafer M4-2535 (sample m8). (b) Lasing spectra for a QCL ($0.2 \times 3.5 \text{ mm}^2$) at different driving conditions in pulsed mode. Dashed lines in (a) and (b) are guides to the eye.

Sample	T_{max} (K)	J_{th} (A cm^{-2})	V_{th} (V)	P_{peak} (mW)	ν (THz)
m8	100	175	4.3	42	4.20–4.50
m9	90	540	6.2	29	4.55–4.85
m10	85	200	4.7	27	4.75–4.95

Table 6.4: Basic operating parameters for laser ridges from the central part of samples m8 to m10 (pulsed operation, $0.2 \times 3.5 \text{ mm}^2$ ridges).

state $|5\rangle$ appears at smaller energies, which shifts the absorption due to the $|4\rangle \rightarrow |5\rangle$ transition to frequencies below the gain region [cf. Fig. 6.6(a)]. Another difference to the original design is a stronger overlap of the injector states $|2\rangle$ and $|3\rangle$ with state $|1\rangle$ of the extraction/injection miniband, which results in multiple radiative laser transitions and causes a net red-shift of the gain peak with increasing field strength. The first sample of this series (m8, wafer M4-2535) resulted in QCL emission in the range of 4.2–4.5 THz. The QCLs operated in pulsed mode up to 100 K with low-temperature values for J_{th} and V_{th} of 175 A cm^{-2} and 4.3 V, respectively, and a peak output power of 42 mW (values for a $0.2 \times 3.5 \text{ mm}^2$ laser ridge). Continuous-wave operation of a $0.1 \times 1.1 \text{ mm}^2$ laser ridge has been possible up to a temperature of 60 K with maximum output powers of 12 mW at 10 K and 1 mW at 60 K.

The net red-shift of the gain peak with increasing field strength as found for the simulations is also observed experimentally for an increasing driving current and voltage [cf. Fig. 6.6(b)]. To adjust the lasing range toward the desired 4.75 THz, all layer thicknesses of the nominal structure have been reduced by a factor of 0.95 for sample m9 (wafer M4-2548). Eventually, this resulted in a difference of 5.5% for the average period length of the two samples as found by x-ray measurements. The emission range of the latter sample is indeed shifted to 4.55–4.85 THz. However, the threshold current density is drastically

6.3 Variation of the laser parameters across a wafer

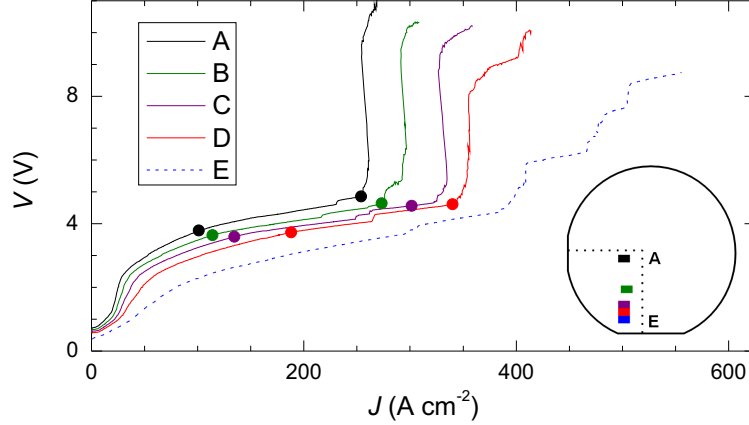


Figure 6.7: Measured I - V characteristics at 5 K for several QCLs from sample M4-2491 ($0.2 \times 3.5 \text{ mm}^2$ ridges, pulsed operation with 500 ns, 5 kHz). The dots indicate J_{th} and J_{max} (maximum output power) on each curve. The inset depicts the location on the wafer for each laser die, and the dashed line indicates the dimensions of the processed wafer piece.

increased to values of 540 A cm^{-2} at 5 K. Due to the high value of J_{th} , cw operation could not be obtained for any laser of this sample. To exclude the possibility of parasitic leakage currents due to a resonant alignment of states of the extraction/injection miniband with excited states of the next period, the layer sequence has been slightly modified for sample m10 (wafer M4-2561). This resulted in a J_{th} value of 200 A cm^{-2} at 5 K and total emission range of 4.75–4.95 THz for pulsed operation of a $0.2 \times 3.5 \text{ mm}^2$ laser ridge starting at the upper end of this range at threshold. Continuous-wave operation of a $0.12 \times 1.2 \text{ mm}^2$ laser stripe has been possible up to a temperature of 50 K with a maximum output power of 5.5 mW at 10 K and 0.1 mW at 50 K and an emission range, which covers 4.86–4.97 THz. Very similar parameters have also been found for other QCLs from this sample. The results of a pulsed-mode characterization for lasers of samples m8–m10 are summarized in Tab. 6.4, and detailed layer sequences are given in the Appendix.

6.3 Variation of the laser parameters across a wafer

Due to the wafer rotation during the MBE growth and the shape of the molecular beams, the heterostructure exhibits a radial symmetry with a negative thickness gradient of a few percent toward the wafer edge (cf. Section 3.2). A series of five QCLs cleaved from different locations on the wafer M4-2491 (sample m6) has been investigated to quantify the impact of the wafer position for the lasing properties of the QCLs

In Fig. 6.7, the measured low-temperature I - V characteristics are shown for the QCLs labeled from A to E, and the inset depicts the location on the wafer die. The operation conditions at threshold and at the maximum output power ($J = J_{\text{max}}$) are depicted as dots on each graph. Lasing is observed for all samples except for sample E, which is located closest to the wafer edge. The values of J_{th} and J_{max} increase toward the

6 THz QCLs for emission above 4 THz

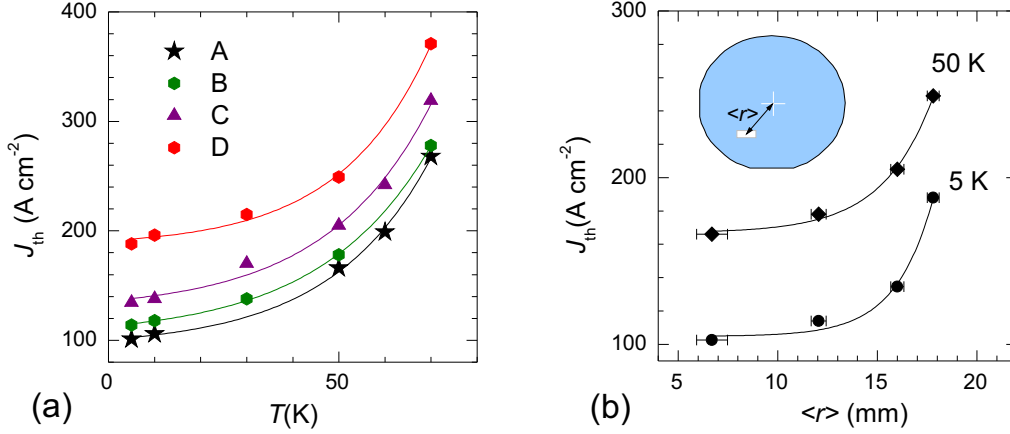


Figure 6.8: (a) Threshold current density vs. temperature for QCLs from different locations on wafer M4-2491 (sample A–D of Fig. 6.7). (b) Threshold current density vs. average distance $\langle r \rangle$ from the wafer center for 5 K and 50 K. The error bars indicate the range of r due to the finite ridge lengths. Solid lines in (a) and (b) refer to exponential fits.

wafer edge by about 100 A cm^{-2} , which is almost an increase by a factor of two for J_{th} . Furthermore, there is appears a general trend from sample A to E toward smaller voltages in the I - V characteristics.

In Fig. 6.8(a), the threshold current density is shown as a function of temperature for samples A–D. The value of T_{max} is approximately 70 K for all QCLs A–D. From the phenomenological fit $J_{th}(T) = J_0 + J_1 \exp(T/T_0)$, only a small decrease for the values of T_0 from 24 to 19.5 K from the center toward the wafer edge is found. While at low temperatures J_{th} differs by almost a factor of 2 between samples A and D, the relative difference becomes smaller at elevated temperatures, which indicates a parasitic current channel related to a temperature-insensitive scattering process. In Fig. 6.8(b), J_{th} is plotted versus the average distance $\langle r \rangle$ from the wafer center for two different temperatures. In both cases, $J_{th}(\langle r \rangle)$ is strongly nonlinear and well approximated by an exponential dependence. The additional increase of J_{max} results in similar dynamic current ranges $J_{max} - J_{th}$ for the different samples. The strong increase of J_{th} toward the wafer edge does not correlate with the values of peak output power, which are 10, 16.5, 16, and 13 mW for QCLs A, B, C, and D, respectively.

The lasing spectra of all samples are in the range of 4.30–4.55 THz, and no significant shift of the emission spectra depending on the wafer position is found. In Fig. 6.9, the lasing spectra are exemplarily shown for QCLs A and D at their respective threshold current density and output power maximum. At threshold, the emission of device D appears slightly blue-shifted as compared to device A. However, this effect is small and is even exceeded by the rather small intrinsic Stark shift for this sample.

The growth gradient of the MBE system was determined for a distributed Bragg reflector structure (M4-2484), which has been grown a few weeks before the present sample M4-2491. According to this data (cf. Fig. 3.2), the change in the average period length from

6.4 Frequency trend of the operating temperature

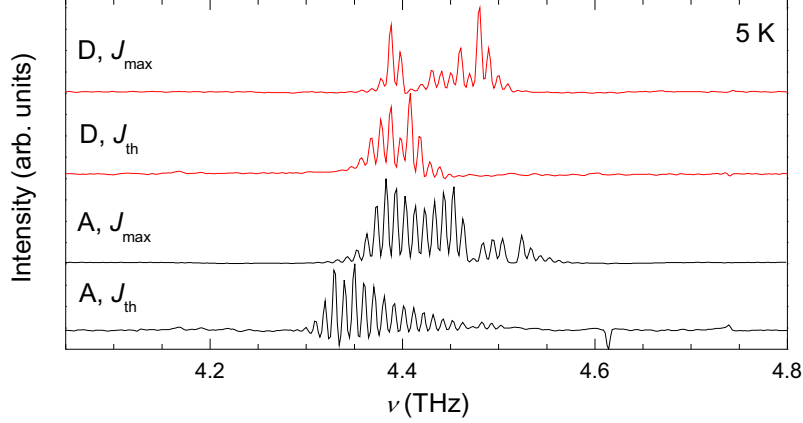


Figure 6.9: Lasing spectra for QCLs A and D at their respective threshold current density J_{th} and output power maximum J_{max} at 5 K.

position A to D and A to E is expected to be -1.6% and -2.1% , respectively. This small decrease does not explain the strong increase of J_{th} toward the wafer edge. An alternative explanation is an increase of the interface roughness with increasing $\langle r \rangle$. It has been shown theoretically that interface roughness can have quite a strong impact on the QCL properties [29]. An increase of the interface roughness toward the wafer edge might be caused by a temperature gradient or by the growth rate modulation — during growth, the rotating wafer experiences a constant growth rate close to the center, but not close to the edge. An experimental determination of interface roughness parameters within the random-fluctuation model has been reported by Jenichen *et al.* [81] for a single quantum well structure based on measurements of the x-ray reflectivity and diffuse scattering. However, due to the much more complex heterostructure and the required spatial resolution, it would be very challenging to perform and evaluate a spatially resolved measurement of this kind for a THz QCL structure. The decreasing operating voltage from sample A to E might be partly caused by the small differences in the series resistance of the bottom contact for the QCLs, which is due to a small etch depth gradient by the wet chemical etching of the mesas.

In summary, the growth gradient of the used MBE system cannot be exploited to select THz QCLs for a particular emission range by its position on the wafer. The effect of the growth gradient on the emission spectra is by far too small, and the strong increase of the threshold current density restricts the use of QCLs, which are cleaved close to the wafer edge. The same qualitative result has been also obtained for other wafers.

6.4 Frequency trend of the operating temperature

With additional small modifications of the active-region sequence based on a single-injection barrier, QCLs with sufficient output power and emission around the target frequency of 4.75 THz are expected. However, cw operation of such QCLs based on single-plasmon waveguides might be restricted to temperatures below 80 K. There appears to be

6 THz QCLs for emission above 4 THz

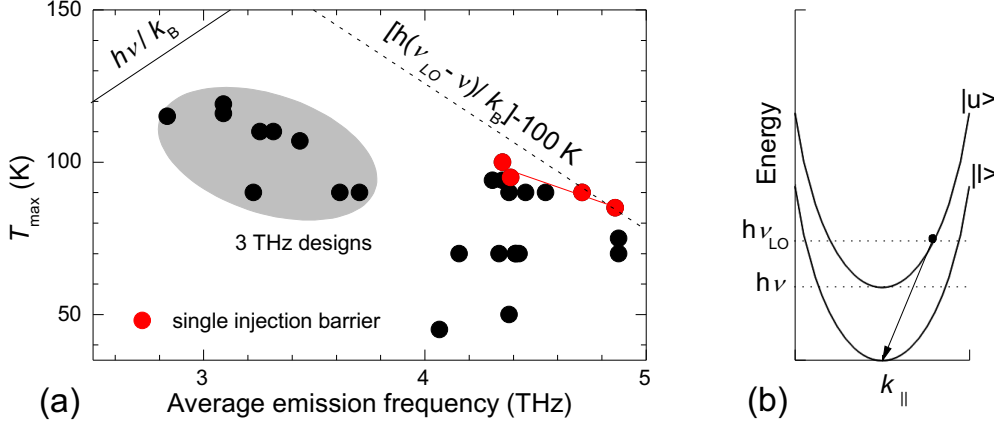


Figure 6.10: (a) Average maximum pulsed operating temperature versus emission frequency for all samples discussed in Chapters 4–6. (b) In-plane subband dispersion of the upper ($|u\rangle$) and lower ($|l\rangle$) laser level. The arrow indicates the non-radiative phonon-assisted transition from ($|u\rangle$) to ($|l\rangle$) at elevated temperatures.

a general trend toward a decreasing value of T_{\max} with increasing frequency. This trend becomes evident by plotting the value of T_{\max} versus the average emission frequency for all characterized THz QCL designs as shown in Fig. 6.10(a). While for the QCLs emitting around 3 THz the maximum operating temperature is close to 120 K, it decreases to 85 K for QCLs emitting at frequencies close to 5 THz. Such a general trend is also found from a similar plot in the review of Williams [42] by comparing data of different authors. Often, the discussion about T_{\max} focuses on the thermal population of subbands at elevated temperatures related to the thermal distribution of electrons and the equivalent temperature $h\nu/k_B$, i.e. the temperature value, which corresponds to a certain emission frequency ν . Due to the large width of thermal distributions and the non-equilibrium operation of QCLs, there is no strict limit and operating temperatures well above $h\nu/k_B$ have been demonstrated for metal-metal THz QCLs emitting below 3 THz [42, 65]. Furthermore, the thermal population of subbands does not explain the trend of a decreasing T_{\max} for higher frequencies, since $h\nu/k_B$ is proportional to the frequency. A more likely explanation for the observed trend is related to phonon emission. At elevated temperatures, the probability for phonon-assisted transitions from the upper into the lower laser subband is proportional to the transition energy. Electrons with sufficient in-plane momentum are scattered via an LO phonon-assisted transition into the lower laser subband as illustrated in Fig. 6.10(b). The frequency dependence of the required thermal activation is given by $[h(\nu_{LO} - \nu)/k_B] - \Delta T_e$, where ΔT_e denotes the temperature difference of the electron gas in the upper laser level with respect to the heat sink. In Fig. 6.10(a), this dependence is marked by a dashed line assuming a value of 100 K for ΔT_e . This is not a strict limit, and the value of ΔT_e might also be lower. However, it explains the general trend of T_{\max} for QCLs operating close to 5 THz.

7 THz QCLs with lateral distributed-feedback gratings

For applications requiring a terahertz source with a high output power at a single frequency, the multi-mode emission spectra of Fabry-Pérot THz QCLs is of limited use, since the total power is typically distributed over many spectral modes. The two conventional approaches for single-mode MIR QCLs have been distributed-feedback (DFB) gratings and external cavity setups [82, 83]. However, for THz QCLs, the realization of tunable external cavities is complicated by the limitations due to the cryogenic operating temperatures and to the fabrication of THz anti-reflection coatings [84]. THz QCLs with a DFB grating are often realized by slits in the top metallization of the laser ridge [85, 86, 87, 88], which provides a strong feedback due to the large modal intensity at the top metal in THz waveguides and the large refractive-index modulation. The electrical contacting of the laser ridges is typically performed by just one or two thin bonding wires attached to the ends of the laser ridge in order to avoid any interference with the grating slits. An alternative approach are lateral DFB (IDFB) gratings [45, 89, 90], which allow for a closed top metallization such as for Fabry-Pérot THz QCLs. The advantage is a homogeneous current injection and the possibility of using a larger number of bonding wires, which reduces the current load for each wire and consequently the risk of failure in case of cw operation. A major step for THz QCLs based on metal-metal waveguides has been the introduction of third-order IDFB gratings, which yielded cw operation with high output powers and a small beam divergence [45]. The approach, which is pursued in this work, is the combination of a single-plasmon waveguide with a first-order IDFB grating. THz QCLs with a first-order IDFB grating and metal-metal waveguide have already been demonstrated in Ref. [90]. However, the output power has been limited to sub-mW levels. Furthermore, it showed that the common formula for DFB gratings severely underestimates the coupling strength for such gratings. In Fig. 7.1(a), a schematic diagram of an IDFB QCL with its two end facets is shown. The grating period Λ corresponds to the vacuum Bragg wavelength of $\lambda_B = 2\Lambda n/m$, where n denotes the real part of the effective refractive index of the waveguide ($n_{\text{eff}} = n + ik$) and m the grating order. The facet phases ϕ_F are defined such that the distance of the facets to the center of the next wide-ridge section of the grating is equal to $\Lambda\phi_F/(2\pi)$. Figure 7.1(b) depicts an etched IDFB mesa after dry etching. Before the discussion of experimental results, the coupled-mode theory of DFB lasers is briefly introduced followed by a method for the calculation of the complex coupling coefficient for IDFB gratings in the case of THz waveguides.

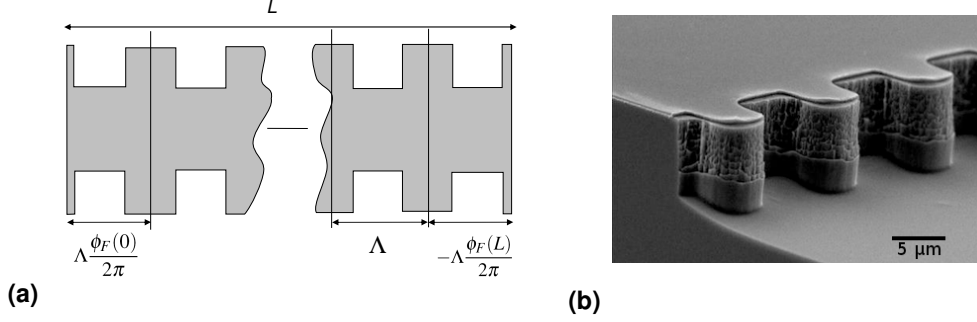


Figure 7.1: (a) Schematic diagram of a THz QCL with a 1DFB grating. L denotes the length of the laser, Λ the grating period, and $\phi_F(0)$ and $\phi_F(L)$ the facet phases with respect to the grating comb for the front and rear facet, respectively. (b) SEM image of a test sample after dry etching of the DFB mesa (M4-2243).

7.1 A brief survey of the coupled-mode theory of DFB lasers

The coupled-mode theory [91] has proven to be a valuable tool for the modeling and understanding of DFB lasers. An introduction to the coupled-mode theory can be found in many textbooks such as Refs. [25, 64, 92]. Here, we will basically follow Ref. [25].

The dielectric function of a uniform DFB grating is modulated in the ridge direction (labeled z in this chapter due to the convention) with $\varepsilon(x, y, z) = \varepsilon(x, y, z + \Lambda)$. It is assumed that the lateral mode profile $\mathbf{E}(x, y)$ can be approximated by the lateral mode profile $\mathbf{E}^{(0)}(x, y)$ of a reference waveguide, which does not depend on z . The ansatz for the electric field becomes

$$\mathbf{E}(x, y, z) = [A(z)e^{i\beta_B z} + B(z)e^{-i\beta_B z}]\mathbf{E}^{(0)}(x, y), \quad (7.1)$$

where $A(z)$ and $B(z)$ denote the amplitudes of the forward and backward propagating wave, respectively, $\beta_B = \pi/\Lambda$ the Bragg propagation constant, and $\mathbf{E}^{(0)}(x, y)$ the solution of the two dimensional waveguide equation for the reference waveguide. β_B can be expressed in terms of the propagation constant $\beta_0 = \omega n_{\text{eff}}/c$ and a number $\Delta\beta$: $\beta_B = \beta_0 - \Delta\beta$. Applying Maxwell's wave equation to the expression (7.1) results in the coupled-mode equations

$$\frac{d}{dz} \begin{pmatrix} A(z) \\ B(z) \end{pmatrix} = i \begin{pmatrix} \Delta\beta & K_{ab} \\ -K_{ba} & -\Delta\beta \end{pmatrix} \begin{pmatrix} A(z) \\ B(z) \end{pmatrix}, \quad (7.2)$$

where K_{ab} and K_{ba} are the coupling coefficients for forward and backward propagating modes, respectively. The modulation of the dielectric function can be decomposed into a Fourier series $\Delta\varepsilon(z) = \sum_m \Delta\varepsilon_m \exp(i2\pi m z/\Lambda)$ with coefficients $\Delta\varepsilon_m$. Usually, K_{ab} and K_{ba} are obtained by integrating over the cross-section of the reference waveguide,

7.1 A brief survey of the coupled-mode theory of DFB lasers

$K_{ab} \propto \int \Delta\varepsilon_{+m} |\mathbf{E}^{(0)}| dA$ and $K_{ba} \propto \int \Delta\varepsilon_{-m} |\mathbf{E}^{(0)}| dA$, where $m = 1$ for a first order grating (cf. Ref. [25]). For index gratings, i.e no modulation of the imaginary part of ε , it can be shown that $K_{ab} = K_{ba}^*$, which simplifies further to $K_{ab} = K_{ba}$ if the grating is symmetric with respect to $z = 0$.

The coupled-mode equations (7.2) are formally solved by

$$\begin{pmatrix} A(z) \\ B(z) \end{pmatrix} = \begin{pmatrix} A_{\pm} \\ B_{\pm} \end{pmatrix} e^{\pm iqz} \quad (7.3)$$

with

$$q = \sqrt{\Delta\beta^2 - K_{ab}K_{ba}}. \quad (7.4)$$

The latter equation defines the dispersion relation for the coupled system of forward and backward propagating modes of an infinite uniform grating. The propagation constant of the coupled system are given by $\beta_{\pm} = \pi/\Lambda \pm q$, while β_0 and $\Delta\beta$ refer to the reference waveguide. Note that q , β_0 , and $\Delta\beta$ are complex quantities in the current notation due to the presence of gain and losses, while the frequency ω is a real quantity.

In the case of index and gain coupling, the coupling coefficients can be written as $K_{ab} = K + iK_g \exp(i\phi_g)$ and $K_{ba} = K + iK_g \exp(-i\phi_g)$ with K denoting the index coupling coefficient, K_g the gain coupling coefficient, and ϕ_g the phase difference between index and gain coupling. We obtain the relation

$$K_{ab}K_{ba} = K^2 - K_g^2 + 2iKK_g \cos(\phi_g). \quad (7.5)$$

Here, only symmetric gratings are considered, for which the origin in the ridge direction z can be chosen such that $\Delta\varepsilon(z) = \Delta\varepsilon(-z)$. The only possible values for ϕ_g are 0 and π , i.e. $K_{ab}K_{ba} = (K \pm iK_g)^2$, where in the following the plus sign is chosen by allowing for negative amplitudes K_g . Using Eq. (7.3), the coupled-mode equations (7.2) can be rewritten in a transfer matrix form

$$\begin{pmatrix} A(L) \\ B(L) \end{pmatrix} = \begin{pmatrix} \cos(qL) + i\frac{\Delta\beta}{q} \sin(qL) & i\frac{K_{ab}}{q} \sin(qL) \\ -i\frac{K_{ba}}{q} \sin(qL) & \cos(qL) - i\frac{\Delta\beta}{q} \sin(qL) \end{pmatrix} \begin{pmatrix} A(0) \\ B(0) \end{pmatrix} \quad (7.6)$$

with the length L of the uniform section. This allows for the application of the transfer-matrix formalism to account for reflective end facets or phase-shift sections (cf. Ref.[25]). Eventually, the resulting eigenvalue problem has to be solved numerically.

Besides the grating period and coupling coefficients, also the facet phases $\phi_F(0)$ and $\phi_F(L)$ enter the eigenvalue problem in the case of reflective end facets, and eventually the eigenfrequencies of the DFB cavity are determined by both. Hence, it is beneficial if besides the grating period also the facet phases can be controlled. In principle, the facets can be dry etched, which has been demonstrated for THz DFB QCLs based on metal-metal waveguides [90]. However, for single-plasmon waveguides, this approach is hampered by the large penetration depth of the optical mode into the substrate. On a cleaved die, usually all laser ridges exhibit the same length. Equal facet phases for two neighboring DFB ridges with periods Λ_1 and $\Lambda_2 = \Lambda_1 + \Delta\Lambda$ are obtained for cavity lengths $L_m = l\Lambda_1 = (l + m)\Lambda_2$, with integers l and m . This results in

$$L_m = m \frac{\Lambda_1 \Lambda_2}{\Lambda_2 - \Lambda_1} = m \frac{\Lambda_1 \Lambda_2}{\Delta \Lambda}. \quad (7.7)$$

For a third grating period Λ_3 , the same facet phase at L_m is obtained for $\Lambda_3 = \Lambda_1 \Lambda_2 / (2\Lambda_1 - \Lambda_2)$. This shows that by a proper design of the lithographic grating mask, equal facet phases for cleaved DFB ridges with different grating periods can be obtained. However, this approach is limited by the precision of cleaving (typically not better than $\pm 100 \mu\text{m}$).

7.2 Calculation of the coupling coefficients for lateral DFB gratings

In Ref. [93], the coupled-mode theory is applied to interband semiconductor lasers with a lateral grating. The coupling coefficient is determined by integrating over the mode profile of a reference waveguide, which uses an average refractive index in the lateral corrugation region. This rather straightforward approach cannot be applied in the present case because of the involved corrugated metal layers. The reason is the large magnitude of $\Delta\varepsilon$ in the case of metals. The assumption that the lateral mode profile does not change between wide- and narrow-ridge sections results in coupling coefficients, which are too small to explain the experimental results. An alternative way to calculate the complex coupling coefficients arises from the dispersion relation (7.4) for a uniform grating, which can be interpreted in terms of the band structure of a one-dimensional photonic crystal. We rewrite Eq. (7.4) using $\omega = \beta_0 c / n_{\text{eff}} = \beta_0 c / (n + ik)$:

$$\omega_{\pm}(q) = \frac{c}{n + ik} \left(\frac{\pi}{\Lambda} \pm \sqrt{q^2 + K_{ab} K_{ba}} \right). \quad (7.8)$$

In the following, the wavevector $\pi/\Lambda \pm q$ is treated as a real quantity, which causes β_0 and $\Delta\beta$ to be real, while the frequency ω becomes complex. The case $q = 0$ correspond to the eigenfrequencies of a one-dimensional photonic crystal at the edge of the Brillouin zone. Assuming a symmetric grating with $K_{ab} K_{ba} = (K + iK_g)^2$, the complex frequencies of the two eigenmodes at $q = 0$ are

$$\omega_{\pm}(0) = \frac{c}{n + ik} \left[\frac{\pi}{\Lambda} \pm (K + iK_g) \right] \approx \frac{c}{n} \left[\frac{\pi}{\Lambda} \pm (K + iK_g) + i \frac{g_n}{2} \right], \quad (7.9)$$

where $g_n = \Gamma g - \alpha_w$ denotes the net gain. The difference of the two eigenfrequencies correspond to the complex coupling coefficient

$$K + iK_g = \frac{n_g}{2c} (\omega_+ - \omega_-) \quad (7.10)$$

with n_g denoting the group refractive index of the reference waveguide as defined in Eq. (2.29). Note that even for index coupling ($K_g = 0$) the frequencies ω_{\pm} are complex. In this case, the imaginary part of $(\omega_+ + \omega_-)$ corresponds to the net gain.

The problem of calculating the coupling coefficients is now shifted to the calculation of the complex eigenfrequencies of a photonic crystal at the Bragg wavevector. For an lDFB grating implemented in a THz waveguide, this requires to solve Maxwell's equations for

7.2 Calculation of the coupling coefficients for lateral DFB gratings

	TM ₀₀	TM ₀₁	TM ₀₂
Re($\omega_-/[2\pi c]$) (cm ⁻¹)	110.83	111.79	113.66
Re($\omega_+[2\pi c]$) (cm ⁻¹)	111.09	112.79	115.54
Im($\omega_-/[2\pi c]$) (cm ⁻¹)	-0.28	-0.53	-0.79
Im($\omega_+[2\pi c]$) (cm ⁻¹)	-0.21	-0.34	-0.55
K (cm ⁻¹)	3.0	11.9	22.5
K_g (cm ⁻¹)	0.8	2.3	2.9

Table 7.1: Real and imaginary part of the eigenfrequencies ω_- and ω_+ and corresponding coupling coefficient $K + iK_g$ ($n_g = 3.8$) for the TM₀₀, TM₀₁, and TM₀₂ modes of the grating geometry shown in Fig. 7.2(a).

the volume of the DFB unit cell with periodic boundary conditions in the ridge direction. This task has been performed by means of a finite element method using the Maxwell solver *JCMsuite* [46, 94]. We have tested the validity of the approach by considering the analytic result for a first-order index grating with a square modulation of the dielectric constant, i.e. a spatially constant refractive index in each section of the grating, and no dispersion ($n_g = n$). In this case, K is given by [92, 93]

$$K = \frac{\Delta\varepsilon}{2\Lambda n^2} = \frac{2\Delta n}{\lambda_B}, \quad (7.11)$$

where $\Delta\varepsilon = 2n\Delta n$ denotes the difference of the dielectric constant between the sections. Using $\Lambda = 12.5 \mu\text{m}$, $\Delta\varepsilon = 0.2$, and $n = 3.584$, Eq. (7.11) results in $K = 6.23 \text{ cm}^{-1}$. The same value (6.23 cm^{-1}) is obtained via the numerical determination of ω_- and ω_+ for a corresponding 1D photonic crystal.

Figure 7.2(a) depicts the geometry of the unit cell used for the calculations of the LDFB coupling coefficients; exploiting the symmetry of the problem, only half of the original grating unit cell is simulated. Modes, which are symmetric and antisymmetric with respect to the center of the ridge, are found for different boundary conditions at $x = 0$ (vanishing tangential magnetic or electric field, respectively). The grating period is $12.5 \mu\text{m}$, and the full width of the ridge is 120 and $107 \mu\text{m}$ in the wide- and narrow-ridge section, respectively. In Figs. 7.2(b), 7.2(c), and 7.2(d), the calculated intensity distributions for the TM₀₀, TM₀₁, and TM₀₂ modes are shown, respectively, i.e. for modes with zero, one, and two lateral intensity nodes. The upper and lower panels in Figs. 7.2(b)–7.2(d) depict the modal intensity for the ω_- and ω_+ frequencies, respectively, while the left and right panels show the top- and front-view projections, respectively. The ω_+ modes are localized in the narrow-ridge section of the grating, and the mode profile is basically that of a Fabry-Pérot single-plasmon waveguide. The ω_- modes are localized mainly in the wide-ridge section. Apparently, the mode profile differs significantly from the ω_+ modes. The intensity distribution exhibits features of a surface plasmon bound to a metal film of finite width [95] such as the large intensity peaks, which occur at the edges of the top metallization outside the actual ridge volume. Furthermore, the ω_- modes appear to couple weakly to the bottom contact metallization.

The results for the eigenfrequencies and coupling coefficients are summarized in Tab. 7.1.

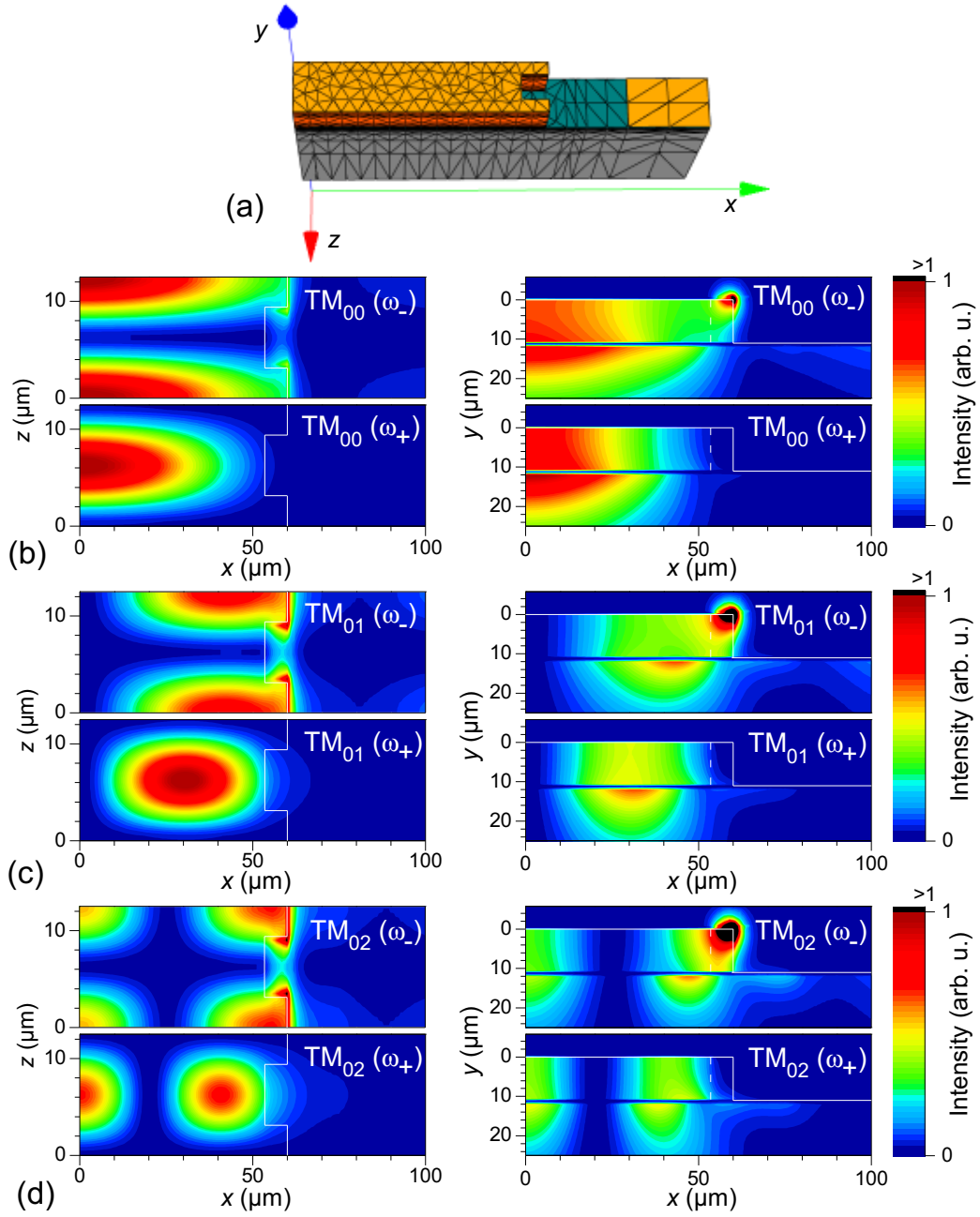


Figure 7.2: (a) Geometry and initial finite-element grid of the unit cell (periodic in the z -direction) used in the simulations. Top and bottom metallizations are dark yellow colored, the active region red, the highly doped bottom contact layer cyan, and the substrate gray. Perfectly matched layers are applied at $x = 100 \mu\text{m}$ (transparent boundary conditions). (b) Projections of the intensity distribution of the ω_- and ω_+ TM_{00} modes to the xz and xy plane. (c) Intensity projections for the two TM_{01} modes. (d) Intensity projections for the two TM_{02} modes.

The magnitude of the coupling coefficient increases strongly with increasing lateral mode index, which is related to a stronger localization of the ω_- modes at the edges of the corrugated ridge. The value of K for the fundamental TM_{00} mode is larger by a factor of 4 as compared to the value of $K = 0.75 \text{ cm}^{-1}$ obtained from the approximation (7.11) using $\Delta\varepsilon = n_w^2 - n_n^2$ with the effective indices n_w and n_n corresponding to separate 2D waveguide solutions for wide- and narrow-ridge section, respectively. The imaginary parts of ω_- and ω_+ are different, which results in an imaginary component K_g for the coupling coefficient. Since gain has been neglected for the simulations, i.e. $g_n = -\alpha_w$, the effective waveguide losses for the corresponding reference waveguide can be determined via $\alpha_w = \text{Im}(\omega_+ + \omega_-)n/c$. A value of 11.1 cm^{-1} for the TM_{00} modes is obtained, while 2D waveguide simulations of the narrow- and wide-ridge section result in 9.5 and 9.4 cm^{-1} , respectively, i.e. the lateral grating causes additional losses of about 1.6 – 1.7 cm^{-1} . The larger magnitude of the imaginary part of ω_{\pm} for the TM_{01} and TM_{02} modes corresponds to effective losses of 20 and 30 cm^{-1} , respectively, which should inhibit lasing in the higher-order lateral modes. Note that the higher-order lateral modes exhibit a larger lateral extend [cf. Fig. 7.2(c)], which increases the uncertainty for the calculated loss values due to the influence of region next to the ridge and the way this region is modeled in the simulations.

So far, the discussion has focused on modes located at $q = 0$, i.e. on the modes adjacent to the photonic bandgap. Note that the continuous dispersion relation (7.8) corresponds to an infinite photonic crystal, while the mode spectrum of a uniform DFB cavity with a finite length L is discrete according to the different minima of the grating reflectivity. The KL product of such a cavity is finite, i.e. the product of the coupling coefficient K and the cavity length L . By considering $q \neq 0$ in the photonic crystal simulations, the behavior of the different longitudinal DFB modes of a uniform grating can be approximately simulated (strictly only for a KL product of infinity, i.e. an infinitely long DFB laser). It shows, that modes with $q \neq 0$ are neither located merely in the wide- nor in narrow-ridge section anymore. As for $q = 0$, the modes located in the ω_- branch have a larger imaginary parts as compared to modes located in the ω_+ branch.

7.3 Experimental results and discussion

The fabrication of the THz QCLs with lateral DFB grating is similar to that of single-plasmon Fabry-Pérot THz QCLs. In the first step, the metal grating is defined in a lift-off process (10/100 nm Ti/Au). This is followed by dry etching of the corrugated mesa and a second metallization step, which defines the bottom contact and reinforces the bonding area of the top contact (300 nm AuGe/Ni). Subsequently, laser dies are cleaved and In-soldered to copper submounts. Special care is taken during wire bonding to avoid hitting the lateral grating regions. In a first step, grating periods of 11.6 – $13.5 \mu\text{m}$ were used for the lithographic masks so that the Bragg frequencies match the range of 3.0 – 3.7 THz . The ridge width, as defined by the mask, is $120 \mu\text{m}$ in the wide-ridge section and $107 \mu\text{m}$ in the narrow-ridge section, and the grating duty cycles were 50% . For dry etching, a reactive ion etch system based on an inductively coupled plasma has been used (Samco, RIE-200iP).

In the following, the experimental results for three laser stripes from a single die with

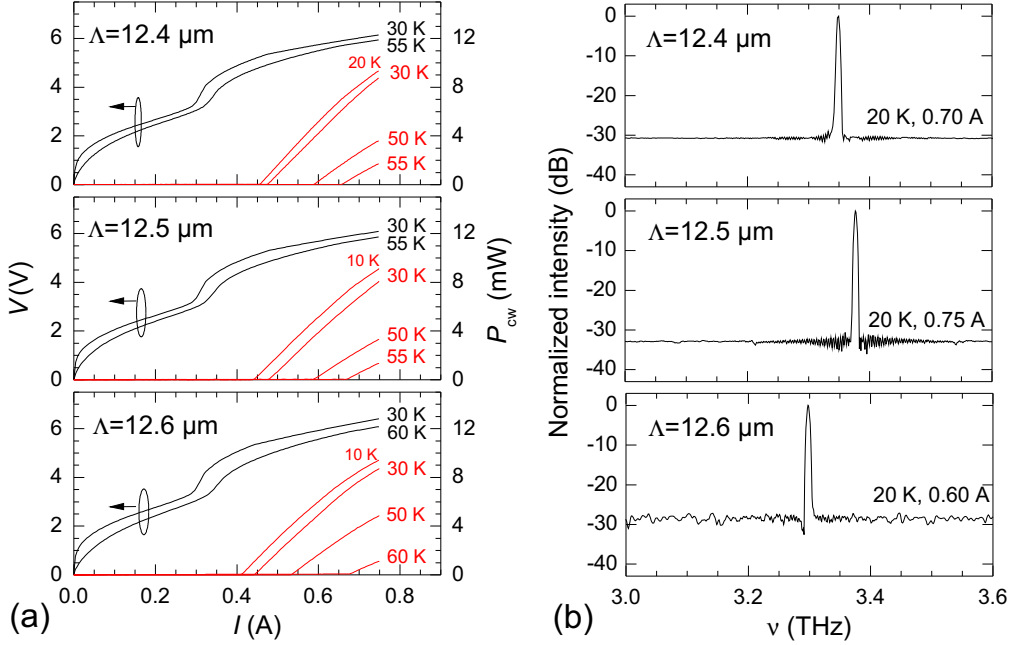


Figure 7.3: Measured characteristics of three IDFB QCLs (ridge length 1.45 mm) with grating periods of 12.4, 12.5, and 12.6 μm in the single-mode operation regime. (a) Continuous-wave L - I - V characteristics at different temperatures. The nominal temperature of 10 K is maintained only up to current values of 0.46 A. (b) Typical lasing spectra in this regime for all three lasers (logarithmic intensity scale).

grating periods of 12.4, 12.5, and 12.6 μm and as-cleaved facets are exemplarily discussed. Since the three laser stripes are located on the same die, they have all the same ridge length (1.45 mm). The lasers were processed from wafer M4-2342, for which Fabry-Pérot lasers emitted in the range of 3.15–3.45 THz. The IDFB lasers operate in cw mode with a single-mode emission regime above threshold switching into a multimode emission regime at elevated driving currents. Figure 7.3(a) shows the light-current-voltage (L - I - V) characteristics of the three lasers for driving currents up to 0.75 A (455 A cm^{-2}). In this range, the emission of the lasers is dominated by a single spectral mode. Due to the large dissipated electrical power, only temperatures above 20 K can be maintained over the whole range of driving currents. The three lasers exhibit similar L - I - V characteristics with threshold current densities J_{th} of 290, 290, and 270 A cm^{-2} at 30 K for $\Lambda = 12.4$, 12.5, and 12.6 μm , respectively. The maximum operating temperature is about 55 K for $\Lambda = 12.4$ and 12.5 μm and about 60 K for $\Lambda = 12.6 \mu\text{m}$. The slope efficiency at threshold (30 K) is approximately 30 mW/A for all three lasers. The output powers at a driving current of 0.75 A are 8.7, 8.0, and 8.7 mW at 30 K and 3.6, 3.3, and 4.8 mW at 50 K for $\Lambda = 12.4$, 12.5, and 12.6 μm , respectively. For comparison, a Fabry-Pérot laser ridge of the same wafer with similar dimensions ($0.1 \times 1.5 \text{ mm}^2$) operated in cw mode up to 55 K with a threshold current density of 320 A cm^{-2} at 30 K, a slope efficiency of 20 mW/A at 30 K, and a maximum cw output power of 7 mW. The reduced threshold current densities of the

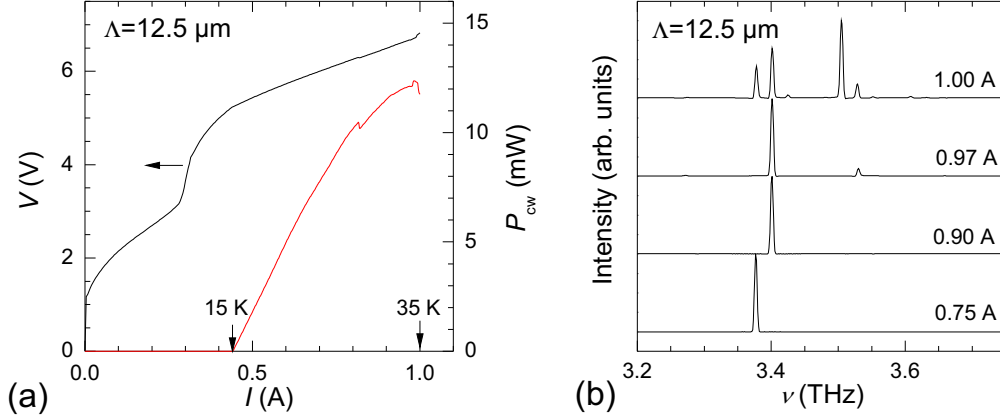


Figure 7.4: (a) Continuous-wave L - I - V characteristics for the laser with $\Lambda = 12.5 \mu\text{m}$ including the multi-mode emission regime (disabled temperature control loop). (b) Corresponding lasing spectra at four different driving currents.

IDFB QCLs as compared to the Fabry-Pérot QCL are qualitatively explained by a smaller threshold gain as a consequence of the feedback provided by the grating in addition to the feedback of the reflective end facets. However, the effect is stronger than expected. While the levels of cw output power are comparable for IDFB and Fabry-Pérot laser ridges, the spectral power density for the IDFB QCLs is much higher due to single-mode operation. Figure 7.3(b) shows typical spectra of the three lasers for the single-mode regime. The side-mode suppression ratio exceeds the signal-to-noise ratio of 20–30 dB, which is limited by the baseline of the used Fourier-transform spectrometer and the QCL intensity. No side-modes could be detected within the entire current and temperature range of Fig. 7.3(a) for the laser with $\Lambda = 12.5 \mu\text{m}$. For the lasers with $\Lambda = 12.4$ (12.6) μm , this regime extends up to 0.7 (0.6) A at 20 K and over the entire current range at elevated temperatures. The single-mode emission for $\Lambda = 12.4$, 12.5, and 12.6 μm occurs at frequencies of 3.35, 3.38, and 3.30 THz, respectively. The single-mode tuning with driving current and temperature is limited to about 5 GHz for each laser, which is related to the rather small temperature dependence of the dielectric constants at low temperatures. While the Bragg frequency of a uniform grating increases with decreasing grating period, the smaller emission frequency for $\Lambda = 12.4 \mu\text{m}$ as compared to 12.5 and 12.6 μm is due to the finite facet reflectance, which will be discussed later.

In Fig. 7.4(a), the L - I - V characteristics is shown for the laser with $\Lambda = 12.5 \mu\text{m}$ including the multi-mode emission regime. Due to the large dissipated electrical power at elevated current levels, the temperature control loop was disabled for this measurement resulting in a linear temperature increase of 20 K between J_{th} and J_{max} . At its maximum, the cw output power exceeds 12 mW for this laser. In Fig. 7.4(b), the emission spectra for different driving currents are shown. Between 0.75 and 0.9 A, the laser emission switches from 3.38 to 3.40 THz. This new regime is related to a discontinuity at 0.82 A in the light-current characteristics, which is also observed in the derivative of the I - V characteristics. Increasing the driving current to 0.97 A, another mode at 3.53 THz starts to appear, and,

7 THz QCLs with lateral distributed-feedback gratings

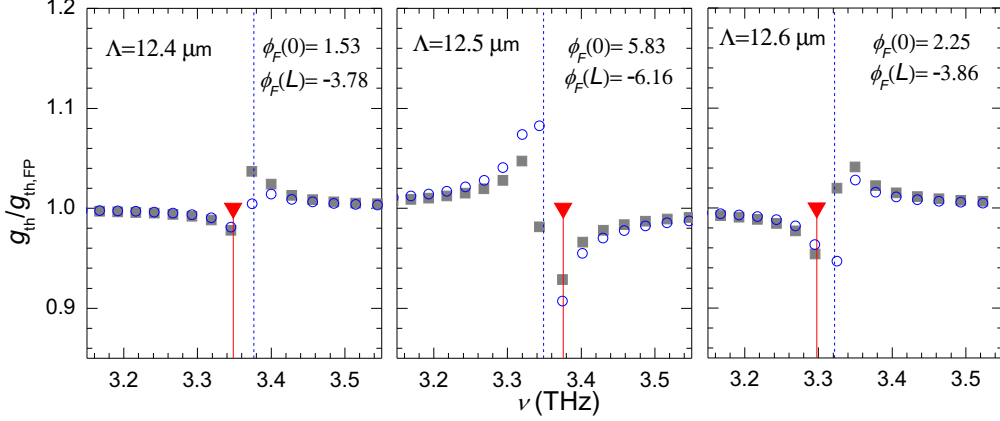


Figure 7.5: Calculated threshold gain g_{th} vs. frequency of the eigenmodes of the IDFB lasers ($\Lambda = 12.4, 12.5,$ and $12.6 \mu\text{m}$) in units of g_{th} of the corresponding Fabry-Pérot cavity. The vertical dashed lines indicate the Bragg frequency using $n = 3.58$. The facet phases ϕ_F have been determined by SEM imaging using the definition of Fig. 7.1(a). Blue circles refer to a complex coupling coefficient [$K + iK_g = (3.0 + 0.8i) \text{ cm}^{-1}$] and gray squares to a real coupling coefficient ($K = 3.0 \text{ cm}^{-1}$). Red triangles indicate the experimentally observed frequencies.

at a driving current of 1.00 A, the laser emission exhibits a complex multi-mode pattern with strong modes at 3.38/3.40 THz and 3.50/3.53 THz.

The emission spectra can be interpreted within the framework of the coupled-mode equations for a DFB cavity with two reflective end facets, for which the facet phases as defined in Fig. 7.1(a) enter the eigenvalue problem. A numerical tool has been used to solve the coupled-mode equations for this case (*CME*, FBH Berlin). In Fig. 7.5, the calculated threshold gain for the TM_{00} mode is plotted versus the frequency eigenvalues for the three IDFB QCLs with $\Lambda = 12.4, 12.5,$ and $12.6 \mu\text{m}$. We have performed simulations either for a complex coupling coefficient or for a real coupling coefficient ($K_g = 0$). The experimentally observed single-mode emission and the calculated longitudinal modes with the lowest threshold gain occur at close-by frequencies, where the quantitative agreement appears to be better for the simulations with a real coupling coefficient. In this case, an agreement better than 9 GHz is found for all three lasers, while in the case of a complex coupling coefficient the calculated mode with the second-lowest threshold gain coincide with the lasing frequency for $\Lambda = 12.6 \mu\text{m}$. While the Bragg frequency (depicted as dashed lines in Fig. 7.5) decreases with increasing grating period, the finite facet reflectance and the different facet phases cause lasing in the longitudinal mode below the Bragg frequency for $\Lambda = 12.4$ and $12.6 \mu\text{m}$ and above the Bragg frequency for $\Lambda = 12.5 \mu\text{m}$. The differences in the calculated threshold gain explain the different experimental threshold current densities. However, the calculation predicts the lowest threshold gain for $\Lambda = 12.5 \mu\text{m}$, but experimentally the lowest J_{th} is found for $\Lambda = 12.6 \mu\text{m}$. Deviations between experiments and simulations are likely due to the uncertainty of the involved parameters such as the coupling coefficients. For instance, the occurrence of a small displacement between the etch and metallization mask might result in a phase difference between index

and gain coupling, which has been neglected in the simulations.

While the single-mode operation regime is quite well explained by the coupled-mode equations for the fundamental lateral TM_{00} mode, the situation becomes more complex for the multi-mode emission regime. In Fig. 7.4(b), the emission of a second mode at 3.40 THz for the laser with $\Lambda = 12.5 \mu\text{m}$ can be understood by the Stark shift of the gain with increasing bias, since the emission frequency agrees with the calculated frequency of the mode with the second lowest threshold gain. However, the multi-mode emission pattern for the highest driving current seems to exhibit a stop band between 3.40 and 3.50 THz. This cannot be explained by the spectral position and threshold gain of the longitudinal modes with TM_{00} symmetry. A likely explanation is the presence of higher-order lateral modes such as TM_{01} and TM_{02} , for which the coupling coefficient is much larger and the Bragg frequency is increased due to the smaller effective index of these modes. For lasing of higher-order lateral modes in favor of the fundamental TM_{00} mode, the threshold gain close to the frequency of the gain maximum has to be smaller as compared to the TM_{00} mode, i.e. the larger coupling coefficient has to compensate for the higher waveguide losses. An experimental indication for the presence of higher-order lateral modes was found by imaging the beam profile with a microbolometer camera. For large driving currents, a change of the beam profile was observed. However, continuous operation in this regime was prevented by the limited cooling power of the used Stirling cooler setup.

7.4 Single-mode emission at specified target frequencies

Of particular interest for far-infrared astronomy is the heterodyne spectroscopy of the OI transition at 4.7448 THz (158.27 cm^{-1}), which requires a local oscillator emitting close to that frequency (preferable 3.6 GHz below or above the OI transition according to the specifications for the heterodyne receiver of the current SOFIA mission). The Fabry-Pérot emission spectra of the wafer M4-2548 include the OI transition frequency for almost all operating conditions. To obtain the desired single-mode operation, an adjusted DFB mask has been applied. Grating periods from 8.2–8.7 μm have been used, while the width of the wide- and narrow-ridge sections have been the same as for the former mask for 3.0–3.7 THz IDFB lasers. In Figs. 7.6(a) and 7.6(b), the emission spectra are shown for a grating period of 8.58 μm and a ridge length of 2.47 mm. Due to the large threshold current density of the used material, only pulsed operation has been possible. The measured spectra are obtained for operation with 10 μs current pulses, which are optimized for low pulse ringing amplitudes to simulate cw driving conditions. Just above threshold at 1.89 A/6.3 V, the laser emits in a single mode at 4.83 THz. With increasing driving bias, the emission switches to a second mode at 4.80 THz and a third mode at 4.75 THz. The red shift of the laser emission frequency with increasing driving current is a particular feature of this active-region design and observed also for Fabry-Pérot lasers (cf. Section 6.2.3). The laser emission becomes again single-mode above a driving current of 2.51 A up to 3 A (the limit of the applied current pulser) and for temperatures up to the maximum operating temperature of 75 K. The laser line in this regime can be tuned between 4.740–4.749 THz ($158.1\text{--}158.4 \text{ cm}^{-1}$), which includes the frequency of the OI transition and would allow for lower- as well as upper-side-band operation of the local oscillator [cf. Fig. 7.6(b)].

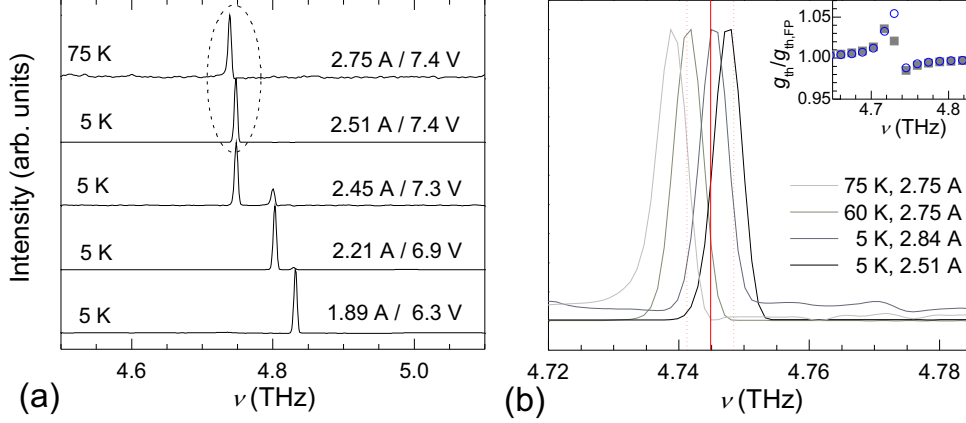


Figure 7.6: (a) Emission spectra for a grating period of $8.58 \mu\text{m}$ (sample M4-2548, 2.47 mm long ridge, pulsed operation with $10 \mu\text{s}$ current pulses). (b) Single-mode emission above 2.5 A . The solid line indicates the OI frequency of 4.745 THz (158.27 cm^{-1}), while the dotted lines indicate the possible upper- and lower-side-band frequency for the local oscillator. Inset: Simulated threshold gain vs. wavenumber for this ridge. Parameters have been $n = 3.695$, $\phi_F(0) = 0.18$, $\phi_F(L) = -0.03$, and $K = 1.5 \text{ cm}^{-1}$. Gray squares: $K_g = 0 \text{ cm}^{-1}$, blue circles: $K_g = 0.4 \text{ cm}^{-1}$.

Due to the stronger waveguide confinement close to 5 THz , the calculated value of K of the fundamental TM_{00} mode is reduced to 1.5 cm^{-1} . This causes the eigenfrequencies of the cavity to be close to the Fabry-Pérot case without any grating. The observed spectra are in agreement with a calculation of the relative threshold gain, which ranges from 0.98 to 1.04 with the lowest value found for the mode at 4.75 THz [cf. inset of Fig. 7.6(b)]. For the calculation, the values for ϕ_F have been determined by SEM imaging.

7.5 Conclusions

The presented results demonstrate that first-order IDFB gratings are suitable to obtain high-power single-mode operation for THz QCLs with single-plasmon waveguides. Based on an active region for 3.3 THz , single-mode operation with cw output powers exceeding 8 mW have been obtained. Simulations of the grating unit cell reveal that the large coupling strength of the gratings is caused by the strong plasmonic metal-light interaction at the lateral grating edges. The emission frequency of the lasers is determined by the Bragg frequency of the grating and the facet phases, i.e. the positions of the cleaved facets with respect to the grating comb. The latter are not known *a priori* due to the limited accuracy of the cleaving process. The uncertainty of the emission frequency is approximately equal to the mode spacing of the corresponding Fabry-Pérot cavity. For a cavity length of 2.5 mm , the spacing of the Fabry-Pérot modes is about 15 GHz . With an intrinsic tuning range of 5 GHz , the number of lasers, which are required to obtain a particular target frequency, is of the order of three. The number of cleaved laser dies can be kept small, if laser ridges with different grating periods are located on the same

die. The grating periods should be chosen in such a way that the difference in the Bragg frequencies is equal or larger than the spacing of the Fabry-Pérot modes for the desired cavity length. To avoid lasing of higher-order lateral modes, the Bragg frequency for the fundamental TM_{00} mode should match approximately the frequency of the gain maximum. If parameters such as the effective refractive index are sufficiently precisely known, a pre-selection of laser ridges could be performed by determining the facet phases via SEM imaging and using these quantities for a numerical solution of the coupled-mode equations.

The feasibility of obtaining single-mode emission at specified target frequencies with a first-order lateral grating and as-cleaved facets has been demonstrated for the OI transition, which requires a local oscillator at (4744.8 ± 3.6) GHz for the heterodyne detection. The total number of tested laser ridges to fulfill this frequency specification was six, located on just two different dies. However, the particular active region did not allow for cw operation due to the large operating current densities.

For all presented lasers, the value of the KL product is about 0.4. A larger KL yields in principle a reduced threshold gain, but a smaller slope efficiency and vice versa [64]. Hence, an increase of KL would be beneficial in order to reduce the threshold current density, but for the trade-off of potentially smaller output powers. To avoid extensively long laser ridges with large total driving currents, further optimizations toward a smaller threshold current density might focus on increasing the coupling coefficients, which are determined by parameters such as the grating duty cycle, the ridge width, and the width difference between wide- and narrow-ridge sections.

8 Nonlinear transport effects related to electric-field domains in THz QCLs

For semiconductor superlattices, many nonlinear transport phenomena are related to the presence of negative differential resistance (NDR) and the formation of electric-field domains (EFDs). Common phenomena, which have been intensively investigated in the past, include discontinuities in the I - V characteristics and current self-oscillations [96, 97, 98]. Although QCLs are based on more complex unit cells than typical semiconductor superlattices, similar effects are known to exist. EFDs have been reported for mid-infrared quantum-cascade structures operated below threshold [99] and also for quantum-cascade structures designed for THz emission [100]. Since these nonlinear transport effects involve the formation and the movement of space charge accumulation and depletion layers, they are not covered by QCL simulations, for which a constant voltage drop in each period is assumed (PVD condition, cf. Section 2.2). However, an understanding of such effects is important, since they are often in conflict with a stable operation of THz QCLs.

In the first part of this chapter, THz QCLs are discussed, for which the presence of stationary EFDs affects the continuous-wave I - V and output power characteristics above threshold, resulting in the observation of discontinuities in the laser characteristics. A method is presented to simulate the QCL characteristics in the presence of NDR and EFDs. In the second part of this chapter, THz QCLs are discussed, for which the I - V and output power characteristics are affected by non-stationary EFDs resulting in current self-oscillations.

8.1 Stationary electric-field domains

The discussion will focus on a particular active-region design, which resulted in extraordinarily low threshold current densities. This allows for the observation of nonlinear transport effects over an extended cw operation range, which would otherwise not be possible due to excessive device heating.

The active-region design labeled TIX3 and the lasing characteristics of the corresponding QCLs below the onset of EFD formation have already been discussed in Section 6.1. Above 6 kV/cm, the simulations reveal an NDR regime for this active region. In Figs. 8.1(a) and 8.1(b), the conduction band offset and wavefunctions are shown at 5.7 kV/cm (close to resonant injection) and at 7.0 kV/cm (in a regime of NDR), respectively. Between the two field strengths, an anticrossing occurs between the upper laser level $|4\rangle$ and the two injector states $|2\rangle$ and $|3\rangle$, which is accompanied by a reduced overlap of these states at 7.0 kV/cm as well as a stronger localization of the lower laser level $|1\rangle$ and the states

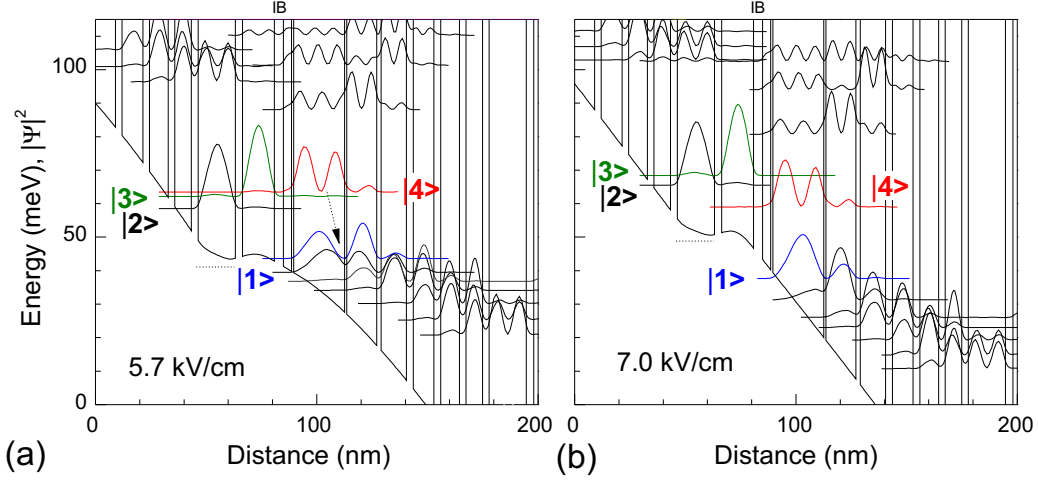


Figure 8.1: (a) Result of a band structure calculation for (a) below and (b) above the onset of NDR for the design TIX3. The doped quantum well is indicated by a dotted horizontal line and the lasing transition by an arrow. IB: injection barrier.

in the extraction/injection miniband. Note also the local screening of the electric field in front of the injection barrier in both cases, which is due to the different distributions of electrons and ionized donors. Since the simulation is based on the PVD condition, i.e. the assumption of an equal voltage drop in each period (cf. Section 2.2), the $J(F)$ characteristics can be considered as an effective drift velocity-field relation $v_D(F)$ for the single active-region period, which is given by $v_D(F) = (Jd)/(en_{\text{dop}})$ for non-zero sheet doping densities n_{dop} . As a consequence of the local screening effect and in contrast to the classical concept of a drift velocity, $v_D(F)$ depends in general also on the doping density of the system. It may also depend on the initial conditions of the system if multiple stationary solutions exist for the system of Schrödinger, Poisson, and rate equations. Multiple stable solutions are found in NDR regions in cases where the doping level causes a significant local screening.

The field-dependent simulations are performed with a discrete stepwidth ΔF , using the solution for the carrier and field distribution for each value of F as the set of initial values for solving the system for $F + \Delta F$. In Fig. 8.2, the calculated $v_D(F)$ characteristics for the nominal doping density (up- and down-sweep) and for a vanishingly small doping density are shown. For a doping density of $n_{\text{dop}} = 2 \times 10^{11} \text{ cm}^{-2}$, two N-shaped regions are obtained: The first one (1–3 kV/cm) is related to the alignment of the extraction/injection miniband, while the N-shaped region around 6.5 kV/cm is related to the anticrossing of the injector states with the upper laser level. The calculated gain maximum is close to the onset of the second NDR region. Within the N-shaped regions, the value of $v_D(F)$ depends on the sweep direction. This is explained by several stable field distributions for a certain value of F and a different order of anticrossings depending on the sweep direction. For a vanishingly small doping density ($n_{\text{dop}} = 1 \text{ cm}^{-2}$), only a single solution $v_D(F)$ exists, and the peak at 1.3 kV/cm disappears. Hence, the first N-shaped region is caused by a local screening of the electric field within each QCL period.

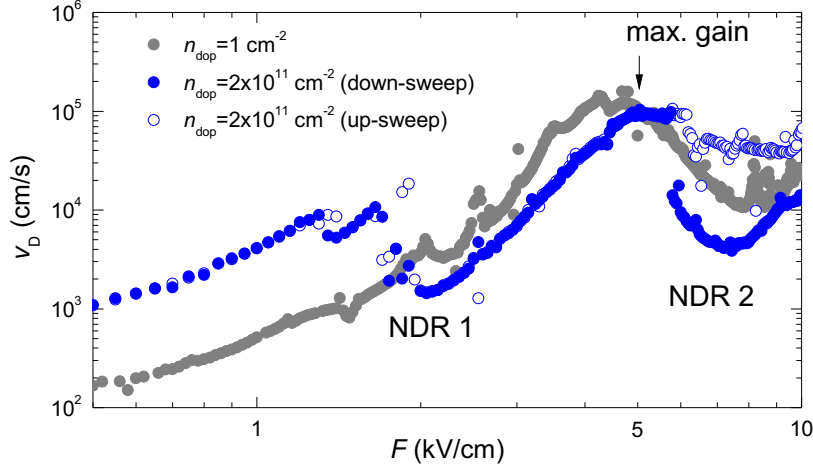


Figure 8.2: Calculated $v_D(F)$ characteristics for $n_{\text{dop}} = 2 \times 10^{11} \text{ cm}^{-2}$ and a vanishing doping density and different sweep directions ($\Delta F = 0.05 \text{ kV/cm}$).

8.1.1 Experimental results

In the following, the experimental results for the two differently doped QCL structures M4-2397 and M4-2404 are discussed, which are referred to as samples A and B, respectively, in this chapter. The doping density for samples A and B is $0.8 \times 10^{11} \text{ cm}^{-2}$ and $2 \times 10^{11} \text{ cm}^{-2}$, respectively. From both samples, devices for cw operation have been fabricated, using ridge dimensions of $0.1 \times 0.55 \text{ mm}^2$ (sample A) and $0.1 \times 0.50 \text{ mm}^2$ (sample B).

The cw L - I - V characteristics and the lasing spectra of device A recorded with a current source are shown in Figs. 8.3(a) and 8.3(b), respectively. The threshold current density at 10 K is as low as 75 A cm^{-2} . The QCL operates in cw mode up to 50 K with a peak output power of about 1.5 mW at 10 K and a rather high slope efficiency of 110 mW A^{-1} . The lasing spectra consist of one or two spectral modes, depending on the operating conditions. At 10 K, single-mode emission at 4.29 THz is found for current densities below 100 A cm^{-2} and at 4.36 THz for current densities above 125 A cm^{-2} . In between, the emission consists of a mixture of both spectral modes. The lower doped device B did not reach the lasing threshold, and in the following only its dc I - V characteristics will be discussed. However, by pulsed operation of a larger QCL ridge, laser emission in the range of 4.35–4.45 THz has been observed for sample B (cf. Section 6.1).

In Fig. 8.4, the cw L - I - V characteristics of device A and the I - V characteristics of device B are shown under voltage bias. The I - V characteristics of each device exhibit two regions of hysteresis in the ranges of 1–3 and 4–16 V. In these regions, the I - V characteristics contain a large number of small discontinuities forming a sawtooth pattern. In the low-voltage hysteresis loops, the number of discontinuities in each branch is close to the number of QCL periods, while in the high-voltage hysteresis loops significantly fewer but larger discontinuities occur. The I - V characteristics of device A and B are qualitatively similar. One main difference is the area enclosed by the hysteresis loop at low voltages, which is significantly smaller for device B.

8 Nonlinear transport effects related to electric-field domains in THz QCLs

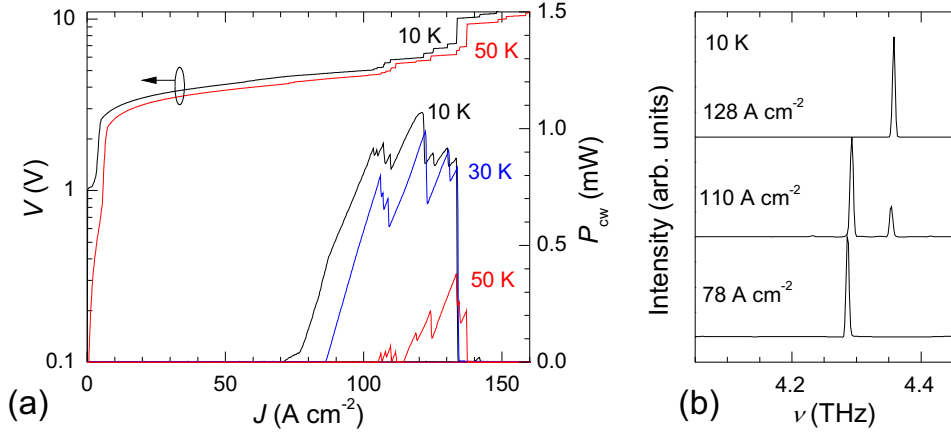


Figure 8.3: (a) Continuous-wave $L-I-V$ characteristics (logarithmic voltage scale) for current biasing (up-sweep, 0.1 mA steps). (b) Measured cw lasing spectra of device A ($0.1 \times 0.55 \text{ mm}^2$ laser ridge) for different current densities at 10 K.

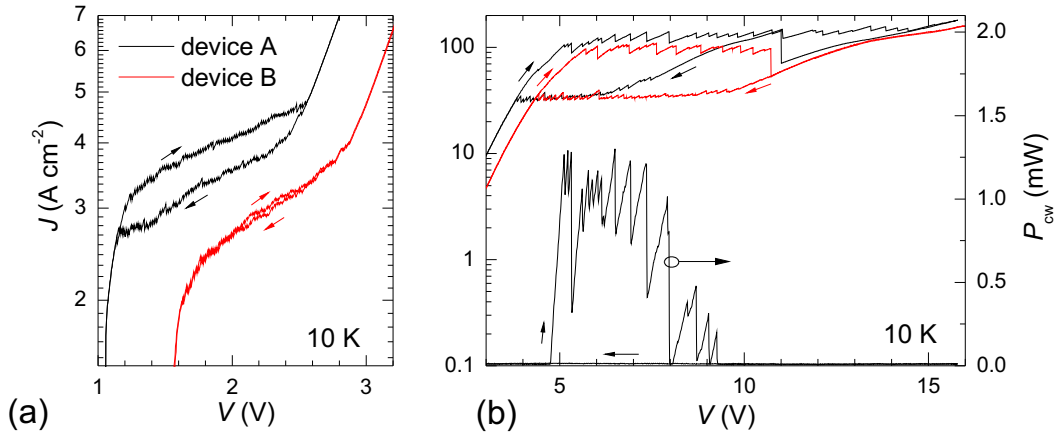


Figure 8.4: Continuous-wave $L-I-V$ characteristic of device A and $I-V$ characteristics of device B (logarithmic current scale) for voltage biasing at 10 K for (a) 0–3 V with a stepwidth of $\Delta V=3 \text{ mV}$ and (b) 3–16 V with $\Delta V=10 \text{ mV}$.

Above threshold of device A, a smooth dependence of the cw output power on the applied bias is found for voltages below 5 V, independent of using a current or voltage source. In the second regime above 5 V, the output power-voltage ($L-V$) characteristics follows a sawtooth pattern if a voltage source is used. The discontinuities in this pattern are correlated with the jumps in the $I-V$ characteristics. The peak amplitudes tend to decrease with increasing voltage, and no emission occurs for voltages above 9.3 V. A similar behavior is found for current biasing [cf. Fig. 8.3(a)]. However, the $I-V$ characteristics follows a plateau-step pattern rather than a sawtooth pattern. The up-sweeps in Figs. 8.3(a) and 8.4 are performed up to a bias at which the QCL already turned off. In such a case, the QCL remains also turned off during a subsequent down-sweep.

8.1.2 Modeling of QCLs in the presence of stationary EFDs

To simulate the QCL transport characteristics beyond the limits of the PVD condition, the set of spatially discrete equations which describes the nonlinear dynamics of weakly coupled superlattices is applied [96, 97]:

$$F_i - F_{i-1} = \frac{e}{\varepsilon\varepsilon_0}(n_{2D}^{(i)} - n_{\text{dop}}), \quad (8.1)$$

$$e \frac{dn_{2D}^{(i)}}{dt} = J_{i-1 \rightarrow i} - J_{i \rightarrow i+1}, \quad (8.2)$$

$$\sum_{i=0}^N F_i = \frac{V}{d}. \quad (8.3)$$

Here F_i denotes the average field strength in period i , $n_{2D}^{(i)}$ the sheet carrier concentration in period i , V the applied voltage, and N the number of periods. The current density, which enters Eq. (8.2), is given by:

$$J_{i \rightarrow i+1} = \frac{v(F_i)}{d} \left[n_{2D}^{(i)} - n_{2D}^{(i+1)} \exp\left(-\frac{eF_i d}{k_B T}\right) \right] \quad (8.4)$$

with v denoting the forward drift velocity [97]. Ohmic boundary conditions are applied with $J_{0 \rightarrow 1} = \sigma_c F_0$ and $J_{N \rightarrow N+1} = \sigma_c F_N$ with σ_c denoting the contact conductance. For simulating a voltage bias, F_0 is determined by the values of V and F_1, \dots, F_N via Eq. (8.3), while for simulating a current bias the condition is $J_{0 \rightarrow 1} = J_{N \rightarrow N+1} = \text{const.}$ The Euler method has been used to find the stationary solutions by iterating Eqs. (8.1)–(8.3) in time until the current densities $J_{i \rightarrow i+1}$ converge to a single value.

In contrast to $v_D(F)$, we assume that $v(F)$ does not depend on the carrier density nor on the initial conditions of the system. With this assumption, the QCL is treated as a superlattice with a particular drift velocity-field relation, i.e. the carrier dynamics within each QCL period becomes decoupled from the dynamics of the macroscopic system. As a consequence, a microscopic description of the charge accumulation process is not covered by this approach. In analogy to superlattice transport models with multiple subband resonances, a sum of Esaki-Tsu terms [101] is used to approximate the data obtained from the PVD calculations:

$$v(F) = \sum_{j=1}^{n_{\text{max}}} \frac{a_j F}{(F - F^{(j)})^2 + b_j^2}. \quad (8.5)$$

Here n_{max} is the number of intersubband resonances, $F^{(j)}$ are the field strengths at the resonances, and a_j and b_j are parameters describing their height and width, respectively. Equation (8.5) automatically fulfills the condition $v(F) \rightarrow 0$ for $F \rightarrow 0$ without having to assume a field dependence of the parameters a_j and b_j . In contrast, the microscopic treatment of superlattice transport in Ref. [97] results in a formal sum of Lorentzians, but with partly field-dependent parameters.

The results of a transport simulation for the voltage biased QCL structure are shown in Figs. 8.5(a) and 8.5(b). The used $v(F)$ relation is shown in the inset of Fig. 8.5(a). Based

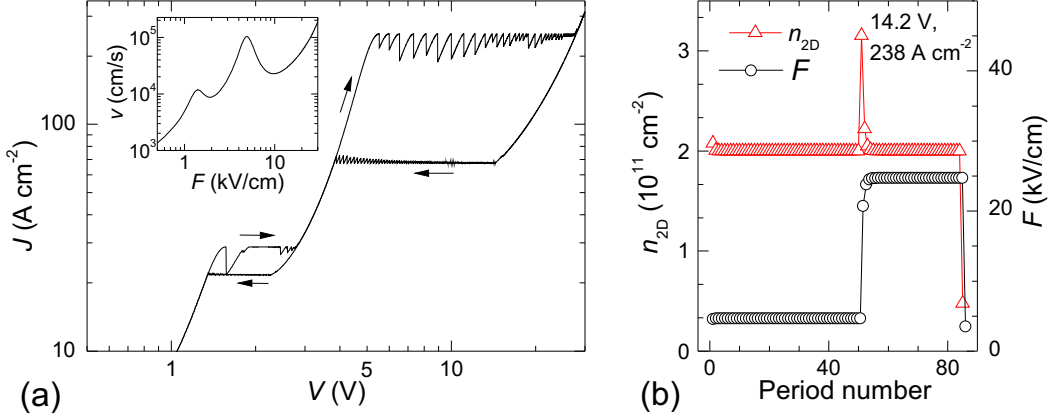


Figure 8.5: (a) Calculated I - V characteristics (logarithmic voltage and current scales) for Ohmic boundary conditions and voltage biasing ($\sigma_c = 0.075 (\Omega \text{ cm})^{-1}$, $n_{\text{dop}} = 2 \times 10^{11} \text{ cm}^{-2}$, $N = 85$, $\Delta V = 5 \text{ mV}$, $T = 30 \text{ K}$). Inset: $v(F)$ relation used in the simulation. (b) Calculated spatial distribution of the carrier density n_{2D} and electric field F at 14.2 V during a voltage up-sweep.

on Eq. (8.5), it fits the $v_D(F)$ data shown in Fig. 8.2 ($n_{\text{dop}} = 2 \times 10^{11} \text{ cm}^{-2}$, averaged over up- and down-sweep). Two regions of hysteresis are observed in the I - V characteristics shown in Fig. 8.5(a), which are related to the NDR regions in the $v(F)$ relation. The jumps in the I - V characteristics are due to the discontinuous motion of a charge accumulation layer, which moves from the collector toward the emitter for an up-sweep and from the emitter toward the collector for a down-sweep of the voltage. The jumps can occur across one or several periods at a time, leading to different jump heights. The distribution of the carriers and the electric field at a point within the second hysteresis loop is exemplarily shown in Fig. 8.5(b). A single charge accumulation layer extending across one period divides a low- and a high-field domain. Scenarios involving also charge depletion layers are obtained, if σ_c is reduced below a value $\sigma_{\text{crit}} = en_{\text{dop}}v_M/(dF_M) = 0.05 (\Omega \text{ cm})^{-1}$, which is determined by the second local maximum (F_M, v_M) in the $v(F)$ relation. Due to a better agreement with the experimental data, we assume that $\sigma_c > \sigma_{\text{crit}}$. It has been further found that the stationary I - V characteristics does not depend significantly on the particular value of σ_c for $\sigma_c \geq 1.5 \sigma_{\text{crit}}$. Note that the use of Ohmic boundary conditions is quite a simplification and that a particular value of σ_c cannot be easily determined by experimental means. In fact, the properties of the contacts are also determined by the quantum wells in the vicinity of the contact interfaces and are very likely non-Ohmic. By changing the parameter a_1 , which affects the height of the first local maximum at 1.3 kV cm^{-1} in the $v(F)$ relation, the area enclosed by the low-voltage hysteresis loop is changed. If set to zero, the domain/hysteresis region at low voltages disappears, while the domain/hysteresis region at higher voltages is not affected. Since the corresponding feature in the effective drift velocity of the single period can be ascribed to a finite doping density (cf. Fig. 8.2), the hysteresis loop at low voltages is a macroscopic signature of the local screening of the electric field within the QCL period.

In the following, a basic model is described to calculate the output power characteristics of the QCL in the presence of EFDs. For simplicity, the influence of stimulated emission on the transport characteristics is not taken into account, which is strictly valid only for a vanishing internal quantum efficiency. A well known effect of stimulated emission is the discontinuity of the differential resistance at threshold [49]. In addition to that, stimulated emission could in principle affect the onset of NDR and domain formation. However, for a sample similar to the present one (M4-2473), it has been found that this effect is rather small [47] and can be neglected to a first approximation.

The output power-current characteristics for a semiconductor laser is given by $P_{\text{out}}(J) = SA(J - J_{\text{th}})$ with S denoting the slope efficiency and A the area of the laser ridge. In case of EFDs, the slope efficiency and the confinement factor depend on the number of periods in the low-field domain, since typically only they contribute to gain. To account for this, the threshold current density is written as:

$$J_{th,\bar{N}} = \frac{\alpha_w + \alpha_m}{\tilde{g}\Gamma_{\bar{N}}} = \frac{N}{\bar{N}} J_{th,N}, \quad (8.6)$$

where \bar{N} denotes the number of periods contributing to gain. $\Gamma_{\bar{N}}$ is the confinement factor for \bar{N} periods: $\Gamma_{\bar{N}} = (\bar{N}/N)\Gamma_N$. Here, it is assumed that the differential gain \tilde{g} is independent of the threshold current density. The slope efficiency is proportional to the number of periods contributing to gain, $S(\bar{N}) \equiv S_{\bar{N}} = (\bar{N}/N) S_N$, where S_N is further assumed to be constant. The output power can now be written as:

$$P(J, \bar{N}) = S_N A \left(\frac{\bar{N}}{N} J - J_{th,N} \right) \quad \text{for } J > J_{th,\bar{N}}, \quad (8.7a)$$

$$P(J, \bar{N}) = 0 \quad \text{for } J < J_{th,\bar{N}}. \quad (8.7b)$$

Since \bar{N} is determined by the nonlinear transport characteristics, Eqs. (8.7a) and (8.7b) cover also cases, for which the QCL turns off above a certain bias and turns on again at an even higher bias, while it stays completely turned off during a down-sweep such as found in the experimental data shown in Figs. 8.3 and 8.4.

To practically determine \bar{N} , the values F_i and the gain-field characteristics of a single period are used. A positive gain occurs only within a small range of the field strength around the gain maximum in the PDR regime, and \bar{N} is identified by the number of periods within this range. The relevant field strength range is obtained from a frequency-independent gain-field characteristics $g(F)$, which is deduced from the frequency-dependent gain-field characteristics for a single period [as shown in Fig. 6.1(b)] via $g(F) = \max_{\omega}[g(\omega, F)]$. The gain-field characteristics is subsequently approximated by a Gaussian profile, and periods within three times the standard deviation σ_s are considered to contribute to the gain. The resulting $g(F)$ characteristics for two different values γ_{IB} for the inhomogeneous broadening (in addition to the lifetime broadening) and the corresponding fits to Gaussian profiles are shown in Fig. 8.6(a).

In this model, $J_{th,N}$ is an input parameter, which is taken from the experiment or from the simulated $J(F)$ characteristics using the value of F , for which $\Gamma_N g(F) = \alpha_w + \alpha_m$ holds. Figure 8.6(b) shows calculated L - V characteristics based on the I - V characteristics

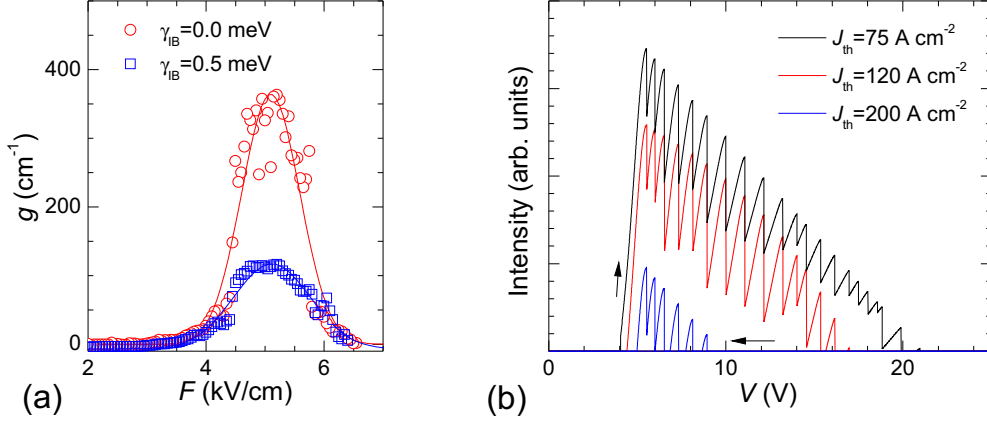


Figure 8.6: (a) Calculated gain-field characteristics for a single period and two different values for the inhomogeneous broadening parameter (symbols). The corresponding fits to Gaussian profiles are shown as lines. (b) Calculated L - V characteristics for three different values of $J_{th,N}$ ($F_{\text{peak}} = 5.1$ kV/cm, $2\sigma_s = 0.98$). No emission occurs during the down-sweeps.

of Fig. 8.5(a). The three values of $J_{th,N}$ correspond to the measured value of J_{th} of device A (75 A cm^{-2}) and the numerical values obtained from the simulations for $\gamma_{IB} = 0$ and 0.5 meV (120 and 200 A cm^{-2} , respectively).¹ Similar to the experimental observation, the output power follows a saw-tooth pattern for an up-sweep of the voltage, while no emission occurs during a down-sweep. The characteristics is mainly affected by the value of $J_{th,N}$. For higher values of $J_{th,N}$, the intensity decreases, eventually resulting in a series of disconnected emission spikes. The temperature increase in the active region, which is due to Ohmic heating in the low- and high-field domain, is not considered in the calculation and is likely to explain the smaller maximum operating voltage of about 9 V in the experimental characteristics of device A as compared to 20 V in the calculation for $J_{th,N} = 75 \text{ A cm}^{-2}$.

8.1.3 Discussion

The simulated and measured characteristics follow basically the same pattern. The discontinuities in the J - V and the L - V characteristics are correlated and explained by a switching of more and more periods into the high-field domain. Hence, a decreasing number of periods in the low-field domain contribute to gain, and the confinement factor and output power are discontinuously reduced. However, up to the point of maximum output, the increasing output power per period with increasing current overcompensates the reduction of the output power due to a decreased confinement factor. By a further increase of the bias, the laser eventually turns off due to the reduced confinement factor and the Ohmic heating, which is enhanced by the additional voltage drop in the high-field domain. Due to the nonlinearity of the system, the exact number, position, and height of the jumps

¹The numerical values have been determined using $\Gamma_N = 0.35$ and $\alpha_w + \alpha_m = 32 \text{ cm}^{-1}$.

8.2 Self-oscillations due to non-stationary electric-field domains

in the I - V and the L - V characteristics depend sensitively on the parameters used in the simulations. Experimentally, these quantities cannot be well reproduced.

The area enclosed by the hysteresis loop at low voltages is significantly smaller for the lower doped sample B. The simulations show that this hysteresis loop can be ascribed to a finite doping level, causing a screening of the electric field in front of the injection barrier. Hence, the occurrence of this loop and the quantitative difference between the differently doped samples A and B can be seen as an experimental fingerprint for the screening of the electric field by mobile carriers within a QCL period.

An obvious relation between jumps in the J - V characteristics and the lasing frequency has not been found. However, frequency jumps may occur below the resolution of the used Fourier transform spectrometer of 0.12 cm^{-1} (3.6 GHz), having consequences for the fine tuning of the cw laser frequency. Such a fine tuning in the sub-GHz range is required for applications such as heterodyne detection [9, 10, 11, 12]. It is usually obtained by changing the cw driving current, exploiting the temperature dependence of the complex refractive index of the laser cavity. For a continuous frequency tuning, the I - V characteristics has to be smooth, which is not the case in the presence of EFDs. Hence, for applications requiring a frequency stabilization, the laser should be operated in a regime without EFDs. Therefore, it would be sufficient if the gain of the QCL period occurs in non-N-shaped parts of the $v_D(F)$ characteristics, i.e. parts which are uniquely invertible.

For the sake of clarity, only experimental results for two samples have been discussed. However, similar results have been obtained for two other samples based on the same active-region design with doping densities of 4 and $5 \times 10^{11} \text{ cm}^{-2}$ (samples M4-2421 and M4-2429, respectively). Due to the higher doping densities and consistent with the previous discussion, the area enclosed by the low-voltage hysteresis loop in the I - V characteristics is larger for these samples. Otherwise, no qualitative differences are observed in the sawtooth patterns of the voltage-driven I - V characteristics. However, the sawtooth patterns in the L - V characteristics tend to have a more complex envelope as compared to sample A.

8.2 Self-oscillations due to non-stationary electric-field domains

Current self-oscillations in systems exhibiting NDR are known since the discovery of the Gunn effect [102]. Their occurrence is also observed for weakly and strongly coupled superlattices [97] and is related to traveling space charge monopoles or dipoles. In weakly coupled superlattices, i.e. systems with an N-shaped NDR, the presence of either stationary EFDs or current self-oscillations depend on the doping density as a critical parameter. The nonlinear transport simulations for THz QCLs described in the previous section result usually only in the formation of stationary EFDs. However, the experiments reveal self-oscillations instead of stationary EFDs for certain THz QCLs. One example is sample M4-2340, for which the lasing characteristics in the usual PDR operation regime have already been discussed in Chapter 5.

Figures 8.7(a) and 8.7(b) depict the results of a dc L - I - V characterization under voltage bias for a laser ridge of sample M4-2340. Current self-oscillations in the NDR regime have been detected by a digital storage oscilloscope using a coaxial cable as a probe. The oscillations are anharmonic [cf. inset of Fig. 8.7(a)] with an oscillation duty cycle, which

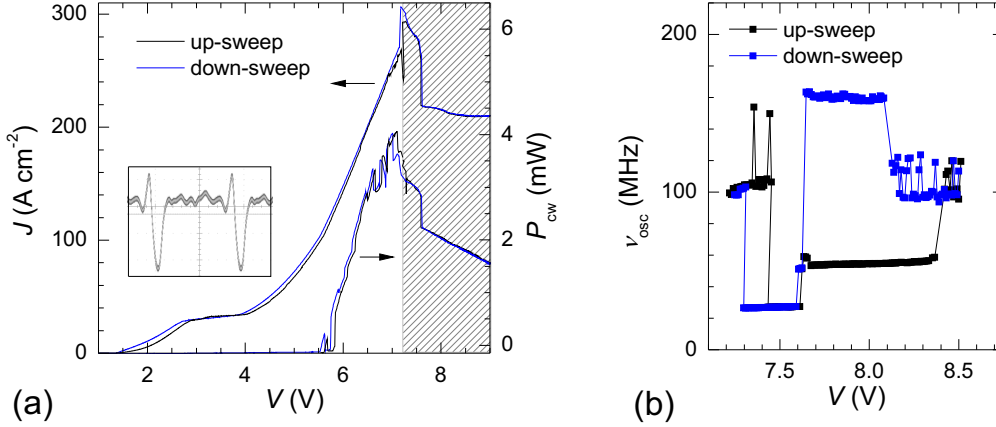


Figure 8.7: (a) L - I - V characteristics under dc voltage bias conditions for sample M4-2340 (0.1×1.7 mm² laser ridge). The voltage region of current self-oscillations is hatched. Inset: oscilloscope trace for a bias above the onset of oscillations. (b) Fundamental frequency of the oscillation vs. voltage.

ranges typically between 10% and 50%. Interestingly, a rather large lasing power of more than 2 mW is still present above the onset of self-oscillations. In contrast to the stationary EFDs for the previously discussed samples, hysteresis loops are practically absent in the dc characteristics [cf. Fig. 8.7(a)]. The fundamental oscillation frequency (i.e. the inverse of the oscillation period) is a discontinuous function of the voltage and ranges between 20 and 160 MHz, which is different for up- and down-sweep [Fig. 8.7(b)]. Note that in the used measurement configuration the oscilloscope monitors the voltage across the QCL. Due to the series resistance of the QCL (mainly caused by the GaAs bottom contact layer), current self-oscillations of the active region are detected as an oscillating voltage. Using a voltage source, the observation of voltage oscillations appears counter-intuitive and is indeed related to the particular experimental situation. For the applied dc source (Keithley, 2635A), the voltage settling time is about 100 μ s [103]. This is much larger than the observed oscillation periods of the order of 5–100 ns and prevents a damping of the oscillations by the voltage control loop, i.e. the dc source acts as a voltage source only on an average time scale.

Since a substantial average lasing output power is observed in the oscillation regime, the question arises whether the current self-oscillations are causing oscillations of the output power and by that additional spectral sidebands. Therefore, the lasing intensity of another laser ridge of this sample has been directly measured using a fast hot-electron bolometer with a bandwidth of about 200 MHz (limited by the used preamplifier). The setup of this measurement is basically the same as for the pulsed-mode characterization of QCLs, where in addition the amplified bolometer signal is measured by the oscilloscope. In Figs. 8.8(a) and 8.8(b), the results for an applied 700 ns driving pulse are shown. After a transient time of 100 ns, the signals of the current monitor and the intensity signal become modulated with the same frequency of 175 MHz (and higher harmonics). By using different pulse sources and driving pulse amplitudes, self-oscillation frequencies in the range of 100–

8.2 Self-oscillations due to non-stationary electric-field domains

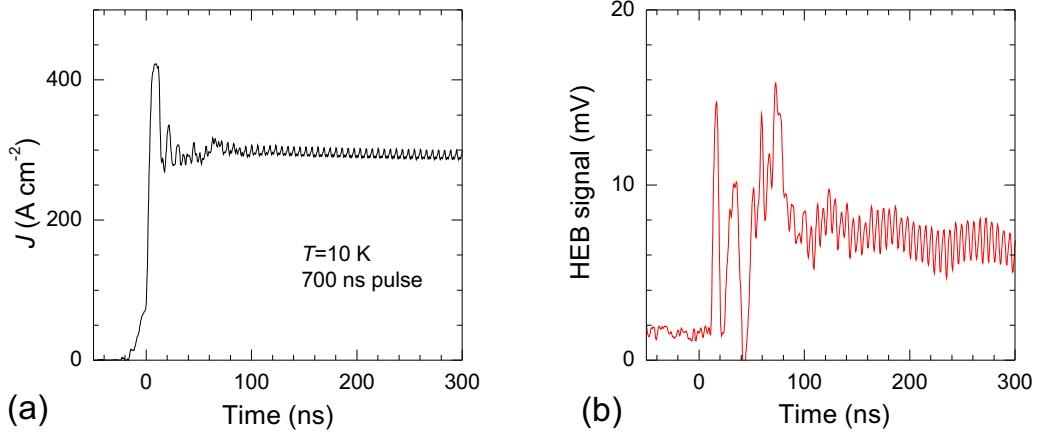


Figure 8.8: Time-resolved measurements for a $0.2 \times 0.94 \text{ mm}^2$ laser ridge of sample M4-2340 operated in pulsed mode above the onset of current self-oscillations. (a) Amplitude of the current pulse. (b) Laser signal as detected with a hot-electron bolometer.

180 MHz have been observed for this device with a discontinuous dependence on the nominal bias value. Spectrally, such modulations cause sideband frequencies of the laser line, which would eventually limit the resolution of heterodyne experiments if the QCL is operated in a self-oscillation regime. While the observed self-oscillations are qualitatively similar for different driving sources and different laser ridges, parameters such as the oscillation frequency and duty cycle depend sensitively on the particular sample and are usually not well reproducible. To confirm that the oscillations are indeed related to internal nonlinear processes of the sample, the lengths of the used coaxial cables have been changed, which revealed that the oscillation frequency is not a function of the cable length.

The nonlinear transport simulations described above usually result in the formation of stationary EFDs if the nominal QCL doping densities are used as a parameter. A lower bound for the critical doping level for the formation of stationary EFDs is given by [97]

$$n_{\text{dop}} > \frac{\varepsilon(F_m - F_M)}{e} \frac{v_m}{v_M - v_m}, \quad (8.8)$$

which is determined by the local minimum (F_m, v_m) and maximum (F_M, v_M) of the drift velocity as a function of the field strength. For the present sample M4-2340, a theoretical value of $2.1 \times 10^{10} \text{ cm}^{-2}$ is obtained, while the experimental doping density is $9 \times 10^{10} \text{ cm}^{-2}$. Using a doping parameter below $2.1 \times 10^{10} \text{ cm}^{-2}$, the simulations reveal self-oscillations instead of stationary EFDs.²

In Fig. 8.9(a), the calculated current-voltage characteristics is shown for a doping level of $2.0 \times 10^{10} \text{ cm}^{-2}$, where the oscillating regime is depicted as a red line. Due to the small doping level, no hysteresis loop is found outside the oscillation regime. To confirm that the oscillations are indeed a property of the system and not an artefact of the numerical iteration loop, different time steps have been used for the Euler iteration (identical results

²To account for a depletion region in the highly doped bottom contact layer, the applied boundary condition for the anode is $J_{N \rightarrow N+1} = \sigma_c n_N F_N$ [96].

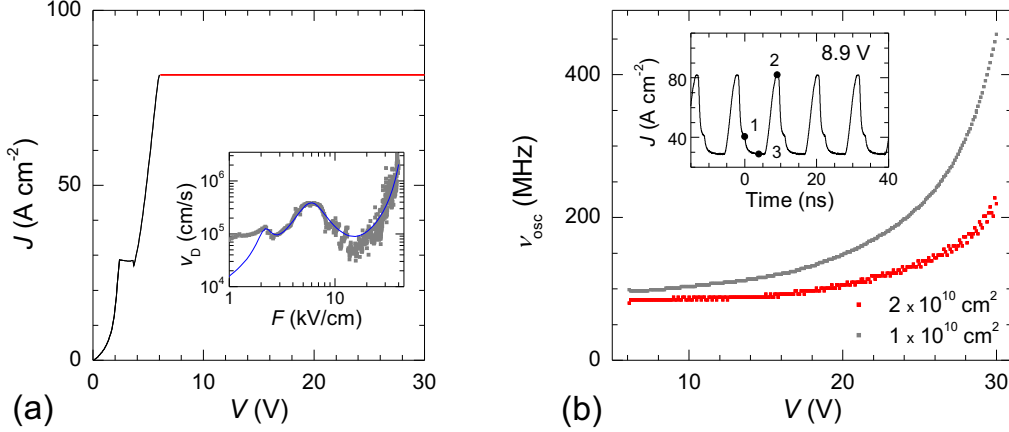


Figure 8.9: (a) Simulated I - V characteristics for sample M4-2340 (up- and down-sweep) and a doping parameter of $2 \times 10^{10} \text{ cm}^{-2}$. The oscillation regime is indicated by the red line. Inset: Drift velocity-field relation. Dots refer to the result of a PVD simulation and the blue line to the Esaki-Tsu approximation used for the nonlinear transport simulations. (b) Fundamental frequency vs. voltage within the oscillation regime. Inset: current oscillation in the time domain for 8.9 V ($2 \times 10^{10} \text{ cm}^{-2}$). Used parameters for the simulation are $\sigma_c = 0.075 (\Omega \text{ cm})^{-1}$, $N = 85$, $\Delta V = 100 \text{ mV}$, $T = 30 \text{ K}$, 15 ps time steps, 240 ns total time.

are obtained for time steps of 7.5 and 15 ps).

For doping levels of $2.0 \times 10^{10} \text{ cm}^{-2}$, the self-oscillation frequencies range between 90–240 MHz for a bias between 6 and 30 V exhibiting a nonlinear increase with voltage [cf. Fig. 8.9(b)]. Decreasing the doping density to $1.0 \times 10^{10} \text{ cm}^{-2}$, the frequency-voltage characteristics remains qualitatively similar, but exhibits a steeper slope. The inset of Fig. 8.9(b) depicts the current oscillations in the time domain for a voltage of 8.9 V ($n_{\text{dop}} = 2.0 \times 10^{10} \text{ cm}^{-2}$). As in the experiment, anharmonic oscillations are found. In the simulations, these oscillations are caused by traveling space charge dipoles. The charge and electric-field distribution in the active region are illustrated in Fig. 8.10 for the three points labeled 1, 2, and 3 in the inset of Fig. 8.9(b). A charge depletion layer followed by a charge accumulation layer travels from the cathode (the top metal contact) toward the anode (the highly doped bottom contact layer). The traveling dipole is related to a traveling high-field domain. During that process, most of the periods remain in the low-field domain. Such dipole oscillations could explain the experimental observation of output-power oscillations over an extended voltage range, since the optical gain would be provided by a large number of periods in the low-field domain.

Just below the critical doping density, the oscillation frequencies are of the same order of magnitude as the experimentally observed frequencies. While for dc biasing the simulations show a continuous voltage dependence of the oscillation frequency, which is independent of the sweep direction, the discontinuous experimental characteristics appear significantly more complex. The different behavior might be in part a consequence of the much larger charge densities in the experimental case, but could be also a consequence of the more complex experimental situation such as the presence of an additional series

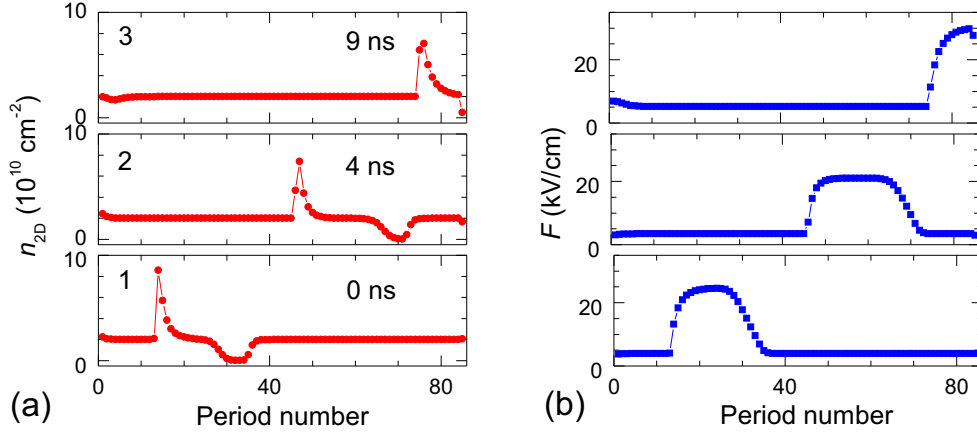


Figure 8.10: (a) Calculated carrier distribution and (b) calculated distribution of the electric field for the three points labeled 1, 2, and 3 in the inset of Fig. 8.9(b).

resistance. An additional experimental problem is the fact that the applied sources are neither true voltage nor current sources on the time scale of the oscillations.

To obtain control of the dipole oscillation frequency, Gunn diodes are operated within a resonant circuit. Recently, similar devices based on current self-oscillations in strongly coupled superlattices have been demonstrated [104, 105, 106]. In analogy, operation within a resonant circuit might represent an additional well-controlled operation mode for THz QCLs in the presence of self-oscillations.

Obviously, the $v_D(F)$ approximation obtained from the microscopic active-region simulation of the present sample results in an incorrect prediction of the critical doping density for the occurrence of current self-oscillations. A more accurate model might be obtained by including the microscopic dynamics of the charge accumulation processes, which is beyond the effective-drift-velocity approach. Note that the critical doping density becomes larger in the presence of additional parasitic current channels, which can be taken into account by considering a shunt conductance σ_{sh} : $v_D(F) \rightarrow v_D(F) + \sigma_{sh}/(en_{3D})F$. For example, for a value of $\sigma_{sh} = 4 \times 10^{-2} (\Omega \text{ cm})^{-1}$, simulations using the nominal doping density of $9 \times 10^{10} \text{ cm}^{-2}$ reveal self-oscillations in the range of 7.2–10.6 V. However, the calculated current densities and oscillation frequencies in the range of 0.5–1.6 GHz are larger by more than a factor of two as compared to the experimental values. In contrast to the simulations based on the original v_D relation, the oscillations are related to the oscillating width of a high-field domain located at the anode.

8.3 Conclusions

The presence of NDR causes several nonlinear transport effects in THz QCLs such as the formation of stationary EFDs and current self-oscillations. Two samples have been presented, for which a coexistence of lasing and either stationary EFDs or current self-oscillations is observed. To simulate such nonlinear transport effects, the macroscopic transport equations for weakly coupled superlattices have been adopted for QCLs by us-

ing an effective drift velocity-field relation. In the case of stationary EFDs, a reasonable agreement between experimental results and simulations is found. The experimentally observed discontinuities and the hysteresis in the L - I - V characteristics are related to the step-wise movement of a single charge accumulation layer from the collector toward the emitter contact for an up-sweep of the bias and from the emitter toward the collector contact for a down-sweep of the bias. In the case of self-oscillations, the situation appears to be more complex. It is found experimentally that current self-oscillations and output power oscillations are correlated. However, particular oscillation parameters such as the frequency depend sensitively on the experimental conditions and are difficult to be reproduced in the calculations. The simulations for this sample fail to predict self-oscillations if the nominal doping density is used as a parameter. By using a doping parameter below the critical doping density for self-oscillations, the simulations result in dipole oscillations related to a high-field domain, which travels from the emitter toward the collector and which is formed by a preceding depletion layer and a following accumulation layer. Similar oscillation frequencies are observed experimentally, which suggests the presence of dipole oscillations in the investigated THz QCLs. In the present model, a static drift velocity-field relation is assumed, i.e. the dynamics of the charge redistribution within the active-region period is neglected. While this approach reproduces many of the observed effects, quantitative and qualitative improvements might be obtained for models, which include stimulated emission as well as the interaction of space charge and electronic transport on the scale of the wavefunctions.

It remains an open question how to avoid dynamic space charge formation in THz QCLs. One general problem for designs including LO phonon-assisted transitions are the large differences between scattering rates below and above the LO phonon energy. Since the photon energy of THz QCLs is below the LO phonon energy, the lasing transition itself presents a strong bottleneck for electrons. This allows for a large population inversion in *resonant phonon* designs, but also generates a large NDR. This problem is partly avoided, if all transitions are designed to be below the LO phonon energy such as in original *bound-to-continuum* designs [68, 69], but with the drawback of a more limited operating temperature range.

9 Summary and outlook

The main focus of this work has been on the development of THz QCLs for spectroscopic applications such as THz heterodyne detectors. A particular interest has been the development of THz QCLs for the use as a local oscillator in heterodyne receivers for the important astronomic OI line at 4.75 THz. Another focus is the investigation of nonlinear transport effects related to the presence of negative differential resistance, which plays an important role regarding the stable operation of THz QCLs.

The development of QCLs for a local oscillator source included several aspects. On the one hand, the active region of the QCL has to provide gain around the desired frequency and has to allow for continuous-wave operation in small-size cryocoolers, which requires low threshold current densities and low operating voltages. On the other hand, a cavity is needed, which allows for controlled single-mode emission. Due to their application-friendly properties such as a suitable emission profile, the investigated lasers use *so-called* single-plasmon waveguides. THz QCLs with high output powers and low operating voltages emitting around 3 THz are obtained for an active-region design based on LO phonon-assisted intersubband transitions. While these lasers rely on a GaAs/Al_xGa_{1-x}As heterostructure with $x = 0.15$, the same heterostructures with an Al content of $x = 0.25$ resulted in very low threshold current densities. By readjusting the barrier thicknesses in order to account for the larger barrier height, QCLs with similar properties for $x = 0.15$ and $x = 0.25$ have been obtained. Due to the higher barriers, $x = 0.25$ has been used for the development of THz QCLs above 4 THz, for which the subband energies are in general increased. Due to the many involved parameters, the realization of an active region which combines suitable continuous-wave operating parameters with emission at 4.75 THz has proven to be challenging. Successive modifications of an active-region design are examined in order to obtain optimized THz QCLs for the desired frequency range. The results indicate a general trend toward a smaller maximum operating temperature at higher frequencies.

For the required single-mode emission, THz QCLs with first-order lateral DFB gratings are investigated. THz QCLs which operate in continuous-wave mode with single-mode emission and high output powers are demonstrated. In conjunction with a general method to calculate the coupling coefficients of the gratings, the lasers are well described by the coupled-mode theory of DFB lasers with two reflective end facets. The emission frequency is determined by the grating period and the positions of the laser facets with respect to the grating comb. One challenge is the inaccuracy of the cleaving process, which causes a frequency uncertainty of the order of the spacing of the Fabry-Pérot modes. This uncertainty can be compensated to a certain extent by a proper combination of ridges with different grating periods on each cleaved die. Eventually, single-mode operation within the frequency specifications for the local oscillator at 4.75 THz has been obtained by examining a small number of laser ridges with slightly different grating periods.

A significant feature of THz QCLs is the occurrence of a negative differential resis-

9 Summary and outlook

tance regime at elevated field strengths, which causes various nonlinear transport effects related to the formation of stationary and non-stationary electric-field domains. For certain THz QCLs, we observed such effects in coexistence with lasing. The presence of stationary electric-field domains is related to discontinuities in the static light-current and current-voltage characteristics, while non-stationary electric-field domains are related to current self-oscillations and a temporal modulation of the output power. To model these effects, the equations describing the nonlinear transport in weakly coupled superlattices are adopted for QCLs by introducing an effective drift velocity-field relation. In the case of stationary domains, a reasonable agreement between measurements and simulations is obtained. However, the simple model fails to explain the observed complex experimental behavior in case of current self-oscillations. Besides an improvement of the nonlinear-transport model, further experimental and theoretical research might focus on the operation of THz QCLs in resonant circuits, which could allow for well-controlled operation modes in the presence of current self-oscillations similar to recently reported superlattice devices.

In terms of the operation as local oscillators at 4.75 THz, one remaining challenge is the combined high-output power, single-mode, and continuous-wave operation of a THz QCL within the frequency specifications, which requires a wafer with gain at the target frequency and sufficiently small threshold current densities. There appears to be no general restriction to obtain this combined goal: single-plasmon waveguides with lateral DFB gratings show to be appropriate cavities for high-output power single-mode emission, and wafers with suitable properties have been obtained already for close-by emission frequencies. While a compact operating system for such THz QCLs can be realized by using small-size Stirling coolers, continuous-wave operation based on liquid nitrogen cooling shows to be challenging. However, for many of the investigated THz QCLs, a better heat management such as episcide-down mounting is likely to result in operating temperatures above 80 K.

Appendix: Nominal layer sequences

All samples are grown at 600 °C on SI GaAs (001). After a 300 nm GaAs buffer layer, a 75 nm $\text{Al}_{0.95}\text{Ga}_{0.05}\text{As}$ layer is grown (used for optical monitoring and as an etch stop, not present for samples marked with *) followed by 700 nm GaAs:Si ($2 \times 10^{18} \text{ cm}^{-3}$), the active-region sequence, and 80 nm GaAs:Si ($5 \times 10^{18} \text{ cm}^{-3}$) as a top contact layer. In the following, only the active-region sequences are given, with the last layer being closest to the substrate. Bold numbers refer to $\text{Al}_x\text{Ga}_{1-x}\text{As}$ barriers, and underlined numbers to doped layers. n_{dop} refer to the nominal volume doping density of the underlined layers.

Wafer No.	M4-2235*, M4-2239*, M4-2243*, M4-2247*, M4-2325, M4-2326
Active region ($x = 0.15$)	$85 \times (10.1/\mathbf{0.5}/16.2/\mathbf{1}/12.9/\mathbf{2}/11.8/\mathbf{3}/9.5/\mathbf{3}/8.6/$ $\mathbf{3}/7.1/\mathbf{3}/\underline{17}/\mathbf{3}/14.5/4)$
n_{dop} (10^{16} cm^{-3})	2.5, 3.0, 2.5, 3.5, 10, 2.5
Wafer No.	M4-2340
Active region ($x = 0.25$)	$85 \times (10.1/\mathbf{0.5}/16.2/\mathbf{1}/12.9/\mathbf{2}/11.8/\mathbf{3}/9.5/\mathbf{3}/8.6/$ $\mathbf{3}/7.1/\mathbf{3}/\underline{17}/\mathbf{3}/14.5/4)$
n_{dop} (10^{16} cm^{-3})	5.0
Wafer No.	M4-2342
Active region ($x = 0.25$)	$85 \times (10.1/\mathbf{0.4}/16.2/\mathbf{0.8}/12.9/\mathbf{1.55}/11.8/\mathbf{2.3}/9.5/\mathbf{2.3}/8.6/$ $\mathbf{2.3}/7.1/\mathbf{2.3}/\underline{17}/\mathbf{2.3}/14.5/\mathbf{3.1})$
n_{dop} (10^{16} cm^{-3})	5.0
Wafer No.	M4-2397*, M4-2404, M4-2421, M4-2429
Active region ($x = 0.25$)	$85 \times (3.7/\mathbf{1}/23/\mathbf{1}/13.5/\mathbf{2}/11.5/\mathbf{3}/9.4/\mathbf{3}/8.5/$ $\mathbf{3}/7.5/\mathbf{3}/\underline{16.8}/\mathbf{3.3}/14.4/4)$
n_{dop} (10^{16} cm^{-3})	6.0, 12, 24, 24
Wafer No.	M4-2435
Active region ($x = 0.25$)	$85 \times (3.7/\mathbf{1}/23/\mathbf{1}/13.5/\mathbf{2}/11.5/\mathbf{1.5}/8.7/\mathbf{1.5}/7.7/$ $\mathbf{1.5}/6.8/\mathbf{1.5}/\underline{16.8}/\mathbf{2.8}/14.4/\mathbf{3})$
n_{dop} (10^{16} cm^{-3})	12

Appendix: Nominal layer sequences

Wafer No.	M4-2454
Active region ($x = 0.25$)	$85 \times (3.7/1/23/1/13.5/2/11.5/3/9.4/3/8.5/$ $3/7.5/3/16.8/2.8/14.4/3)$
n_{dop} (10^{16} cm^{-3})	12
Wafer No.	M4-2455
Active region ($x = 0.25$)	$85 \times (3.7/1/23/1/13.5/2/11.5/1.5/8.7/1.5/7.7/$ $1.5/6.8/1.5/16.8/3.3/14.4/4)$
n_{dop} (10^{16} cm^{-3})	12
Wafer No.	M4-2473, M4-2478
Active region ($x = 0.25$)	$85 \times (3.1/1.3/24.4/1.5/14.5/2/11.6/3/9.4/3/7.8/$ $2.2/7.0/2.2/16.2/3.8/14.8/1.7)$
n_{dop} (10^{16} cm^{-3})	8.0, 12
Wafer No.	M4-2491, M4-2540
Active region ($x = 0.25$)	$85 \times (3.5/1.5/24.4/1.8/14.5/2.5/11.8/3/9.4/3/7.8/$ $2.2/7.0/1.8/15.7/3.8/14.3/1.5)$
n_{dop} (10^{16} cm^{-3})	12, 12
Wafer No.	M4-2535
Active region ($x = 0.25$)	$88 \times (25.4/1.7/16.6/0.8/10.3/1.2/9.4/1.6/7.8/1.9/7.0/$ $1.9/17.2/3.8/15.5/3.0)$
n_{dop} (10^{16} cm^{-3})	8.0
Wafer No.	M4-2548
Active region ($x = 0.25$)	$88 \times (24.1/1.6/15.8/0.8/9.8/1.1/8.9/1.5/7.4/1.8/6.7/$ $1.8/16.3/3.6/14.7/2.8)$
n_{dop} (10^{16} cm^{-3})	8.0
Wafer No.	M4-2561
Active region ($x = 0.25$)	$88 \times (24.9/1.9/16.3/0.9/10.1/1.3/9.2/1.8/7.6/2.1/6.9/$ $1.85/16.9/3.8/15.2/3.3)$
n_{dop} (10^{16} cm^{-3})	8.0

Bibliography

- [1] R. Kazarinov and R. A. Suris. Amplification of electromagnetic waves in a semiconductor superlattice. *Sov. Phys. Semicond.*, 5:707–709, 1971.
- [2] J. Faist, F. Capasso, D. L. Sivco, C. Sirtori, A. L. Hutchinson, and A. Y. Cho. Quantum cascade laser. *Science*, 264:553–556, 1994.
- [3] R. Köhler, A. Tredicucci, F. Beltram, H. E. Beere, E. H. Linfield, A. G. Davies, D. A. Ritchie, R. C. Iotti, and F. Rossi. Terahertz semiconductor-heterostructure laser. *Nature (London)*, 417:156–159, 2002.
- [4] S. Kumar, Q. Hu, and J. L. Reno. 186 K operation of terahertz quantum-cascade lasers based on a diagonal design. *Appl. Phys. Lett.*, 94:131105, 2009.
- [5] B. S. Williams, S. Kumar, Q. Hu, and J. L. Reno. High-power terahertz quantum-cascade lasers. *Electron. Lett.*, 42:89–90, 2006.
- [6] G. Scalari, C. Walther, M. Fischer, R. Terazzi, H. Beere, D. Ritchie, and J. Faist. THz and sub-THz quantum cascade lasers. *Laser & Photon. Rev.*, 3:45–66, 2009.
- [7] H.-W. Hübers, S. G. Pavlov, A. D. Semenov, R. Köhler, L. Mahler, A. Tredicucci, H. E. Beere, D. A. Ritchie, and E. H. Linfield. Terahertz quantum cascade laser as local oscillator in a heterodyne receiver. *Opt. Express*, 13:5890–5896, 2005.
- [8] J. R. Gao, J. N. Hovenier, Z. Q. Yang, J. J. Baselmans, A. Baryshev, M. Hajenius, T. M. Klapwijk, A. J. L. Adam, T. O. Klaassen, B. S. Williams, S. Kumar, Q. Hu, and J. L. Reno. Terahertz heterodyne receiver based on a quantum cascade laser and a superconducting bolometer. *Appl. Phys. Lett.*, 86:244104, 2005.
- [9] H. Richter, A. D. Semenov, S. G. Pavlov, L. Mahler, A. Tredicucci, H. E. Beere, D. A. Ritchie, K. S. Il'in, M. Siegel, and H.-W. Hübers. Terahertz heterodyne receiver with quantum cascade laser and hot electron bolometer mixer in a pulse tube cooler. *Appl. Phys. Lett.*, 93:141108, 2008.
- [10] P. Khosropanah, W. Zhang, J. N. Hovenier, J. R. Gao, T. M. Klapwijk, M. I. Amanti, G. Scalari, and J. Faist. 3.4 THz heterodyne receiver using a hot electron bolometer and a distributed feedback quantum cascade laser. *J. Appl. Phys.*, 104:113106, 2008.
- [11] D. Rabanus, U. U. Graf, M. Philipp, O. Ricken, J. Stutzki, B. Vowinkel, M. C. Wiedner, C. Walther, M. Fischer, and J. Faist. Phase locking of a 1.5 Terahertz quantum cascade laser and use as a local oscillator in a heterodyne HEB receiver. *Opt. Express*, 17:1159–1168, 2009.

Bibliography

- [12] Y. Ren, J. N. Hovenier, R. Higgins, J. R. Gao, T. M. Klapwijk, S. C. Shi, B. Klein, T.-Y. Kao, Q. Hu, and J. L. Reno. High-resolution heterodyne spectroscopy using a tunable quantum cascade laser around 3.5 THz. *Appl. Phys. Lett.*, 98:231109, 2011.
- [13] L. Ajili, G. Scalari, N. Hoyler, M. Giovannini, and J. Faist. InGaAs-AlInAs/InP terahertz quantum cascade laser. *Appl. Phys. Lett.*, 87:141107, 2005.
- [14] M. Fischer, G. Scalari, K. Celebi, M. Amanti, Ch. Walther, M. Beck, and J. Faist. Scattering processes in terahertz InGaAs/InAlAs quantum cascade lasers. *Appl. Phys. Lett.*, 97:221114, 2010.
- [15] Ch. Deutsch, A. Benz, H. Detz, P. Klang, M. Nobile, A. M. Andrews, W. Schrenk, T. Kubis, P. Vogl, G. Strasser, and K. Unterrainer. Terahertz quantum cascade lasers based on type II InGaAs/GaAsSb/InP. *Appl. Phys. Lett.*, 97:261110, 2010.
- [16] I. Vurgaftman, J. R. Meyer, and L. R. Ram-Mohan. Band parameters for III-V compound semiconductors and their alloys. *J. Appl. Phys.*, 89:5815, 2001.
- [17] J. W. Matthews and A. E. Blakeslee. Defects in epitaxial multilayers. *J. Cryst. Growth*, 27:118 – 125, 1974.
- [18] I. Waldmueller, M. C. Wanke, and W. W. Chow. Circumventing the Manley-Rowe quantum efficiency limit in an optically pumped terahertz quantum-cascade amplifier. *Phys. Rev. Lett.*, 99:117401, 2007.
- [19] M. Giehler, M. Wienold, L. Schrottke, R. Hey, H. T. Grahn, S. G. Pavlov, H.-W. Hübers, S. Winnerl, and H. Schneider. Mid-infrared pump-related electric-field domains in GaAs/(Al,Ga)As quantum-cascade structures for terahertz lasing without population inversion. *J. Appl. Phys.*, 110:103104, 2011.
- [20] G. Bastard. Superlattice band structure in the envelope-function approximation. *Phys. Rev. B*, 24:5693–5697, 1981.
- [21] G. Bastard. *Wave mechanics applied to semiconductor heterostructures*. Les Éditions de Physique, Les Ulis Cedex, France, 1988.
- [22] L. Schrottke, M. Giehler, M. Wienold, R. Hey, and H. T. Grahn. Compact model for the efficient simulation of the optical gain and transport properties in THz quantum-cascade lasers. *Semicond. Sci. Technol.*, 25:045025, 2010.
- [23] H. Schneider and H. C. Liu. *Quantum well infrared photodetectors - physics and applications*. Springer-Verlag, Berlin, 2007.
- [24] W. Schäfer and M. Wegener. *Semiconductor Optics and transport phenomena*. Springer-Verlag, Berlin, 2002.
- [25] S. L. Chuang. *Physics of Photonic Devices*. Wiley, New York, 2nd edition, 2009.
- [26] P. Harrison. *Quantum Wells, Wires and Dots: Theoretical and Computational Physics of Semiconductor Nanostructures*. John Wiley & Sons, Chichester, England, 2005.

- [27] H. Callebaut and Q. Hu. Importance of coherence for electron transport in terahertz quantum cascade lasers. *J. Appl. Phys.*, 98:104505, 2005.
- [28] H. Willenberg, G. H. Döhler, and J. Faist. Intersubband gain in a Bloch oscillator and quantum cascade laser. *Phys. Rev. B*, 67:085315, 2003.
- [29] T. Kubis, C. Yeh, P. Vogl, A. Benz, G. Fasching, and C. Deutsch. Theory of nonequilibrium quantum transport and energy dissipation in terahertz quantum cascade lasers. *Phys. Rev. B*, 79:195323, 2009.
- [30] S.-C. Lee and A. Wacker. Nonequilibrium Green's function theory for transport and gain properties of quantum cascade structures. *Phys. Rev. B*, 66:245314, 2002.
- [31] P. Kleinert and V. V. Bryksin. Theoretical study of carrier transport in two-band semiconductor superlattices. *Physica B*, 304:60–66, 2001.
- [32] A. Wacker. Gain in quantum cascade lasers and superlattices: A quantum transport theory. *Phys. Rev. B*, 66:085326, 2002.
- [33] P. Y. Yu and M. Cardona. *Fundamentals of Semiconductors*. Springer-Verlag, Berlin, 3rd edition, 2005.
- [34] E. D. Palik, editor. *Handbook of Optical Constants of Solids*. Academic Press, Orlando, Florida, 1985.
- [35] E. D. Palik, editor. *Handbook of Optical Constants of Solids II*. Academic Press, San Diego, 1991.
- [36] M. Levinshtein, S. Rumyantsev, and M. Shur, editors. *Handbook series on semiconductor parameters*, volume 1. World Scientific, Singapore, 1996.
- [37] H. A. Macleod. *Thin-Film Optical Filters*. Institute of Physics, Bristol, 3rd edition, 2001.
- [38] S. Kohen, B. S. Williams, and Q. Hu. Electromagnetic modeling of terahertz quantum cascade laser waveguides and resonators. *J. Appl. Phys.*, 97:053106, 2005.
- [39] J. Lloyd-Hughes, Y. L. Delley, G. Scalari, M. Fischer, V. Liverini, M. Beck, and J. Faist. Spectroscopic determination of the doping and mobility of terahertz quantum cascade structures. *J. Appl. Phys.*, 106:093104, 2009.
- [40] V.M. Agranovich and V.E. Kravtsov. Notes on crystal optics of superlattices. *Solid State Commun.*, 55:85–90, 1985.
- [41] M. Rochat, A. Lassaad, H. Willenberg, J. Faist, H. Beere, G. Davies, E. Linfield, and D. Ritchie. Low-threshold terahertz quantum-cascade lasers. *Appl. Phys. Lett.*, 81:1381–1383, 2002.
- [42] B. S. Williams. Terahertz quantum-cascade lasers. *Nature Photon.*, 1:517–525, 2007.

Bibliography

- [43] P. Gellie, W. Maineult, A. Andronico, G. Leo, C. Sirtori, S. Barbieri, Y. Chassagneux, J. R. Coudevylle, R. Colombelli, S. P. Khanna, E. H. Linfield, and A. G. Davies. Effect of transverse mode structure on the far field pattern of metal-metal terahertz quantum cascade lasers. *J. Appl. Phys.*, 104:124513, 2008.
- [44] S. Kumar, B. S. Williams, Q. Qin, A. W. M. Lee, and Q. Hu. Surface-emitting distributed feedback terahertz quantum-cascade lasers in metal-metal waveguides. *Opt. Express*, 15:113–128, 2006.
- [45] M. I. Amanti, G. Scalari, F. Castellano, M. Beck, and J. Faist. Low divergence Terahertz photonic-wire laser. *Opt. Express*, 18:6390–6395, 2010.
- [46] JCMwave GmbH. URL <http://www.jcmwave.com>.
- [47] R. Sharma, L. Schrottke, M. Wienold, K. Biermann, R. Hey, and H. T. Grahn. Effect of stimulated emission on the transport characteristics of terahertz quantum-cascade lasers. *Appl. Phys. Lett.*, 99:151116, 2011.
- [48] R. Eichholz, H. Richter, S. G. Pavlov, M. Wienold, L. Schrottke, R. Hey, H. T. Grahn, and H.-W. Hübers. Multi-channel terahertz grating spectrometer with quantum-cascade laser and microbolometer array. *Appl. Phys. Lett.*, 99:141112, 2011.
- [49] C. Sirtori, F. Capasso, J. Faist, A. L. Hutchinson, D. L. Sivco, and A. Y. Cho. Resonant tunneling in quantum cascade lasers. *IEEE J. Quantum Electron.*, 34:1722–1729, 1998.
- [50] J. Faist, M. Beck, T. Aellen, and E. Gini. Quantum-cascade lasers based on a bound-to-continuum transition. *Appl. Phys. Lett.*, 78:147–149, 2001.
- [51] S. Kumar, C. W. I. Chan, Q. Hu, and J. L. Reno. Two-well terahertz quantum-cascade laser with direct intrawell-phonon depopulation. *Appl. Phys. Lett.*, 95:141110, 2009.
- [52] A. Barkan, F. K. Tittel, D. M. Mittleman, R. Dengler, P. H. Siegel, G. Scalari, L. Ajili, J. Faist, H. E. Beere, E. H. Linfield, A. G. Davies, and D. A. Ritchie. Linewidth and tuning characteristics of terahertz quantum cascade lasers. *Opt. Lett.*, 29:575–577, 2004.
- [53] C. H. Henry. Theory of the linewidth of semiconductor lasers. *IEEE J. Quantum Electron.*, 18:259–264, 1982.
- [54] M. Yamanishi, T. Edamura, K. Fujita, N. Akikusa, and H. Kan. Theory of the intrinsic linewidth of quantum-cascade lasers: Hidden reason for the narrow linewidth and line-broadening by thermal photons. *IEEE J. Quantum Electron.*, 44:12–29, 2008.
- [55] S. Bartalini, S. Borri, P. Cancio, A. Castrillo, I. Galli, G. Giusfredi, D. Mazzotti, L. Gianfrani, and P. De Natale. Observing the intrinsic linewidth of a quantum-cascade laser: Beyond the Schawlow-Townes limit. *Phys. Rev. Lett.*, 104:083904, 2010.

- [56] C. Jirauschek. Monte Carlo study of intrinsic linewidths in terahertz quantum cascade lasers. *Opt. Express*, 18:25922–25927, 2010.
- [57] L. Schrottke, M. Giehler, M. Wienold, R. Hey, and H.T. Grahn. Simulation of the interplay between stimulated emission and carrier distribution in quantum-cascade lasers. *Physica E*, 42:2632–2635, 2010.
- [58] L. Schrottke, M. Wienold, M. Giehler, R. Hey, and H. T. Grahn. Analysis of the slope efficiency for terahertz quantum-cascade lasers. *J. Appl. Phys.*, 108:103108, 2010.
- [59] K. Biermann, E. A. Cerda-Méndez, M. Höricke, P. V. Santos, and R. Hey. Controlled growth of exciton-polariton microcavities using in situ spectral reflectivity measurements. *J. Cryst. Growth*, 323:56–59, 2011.
- [60] D. Goren, N. Amir, and Y. Nemirovsky. Determination of the interface charge between an epilayer and a substrate using capacitance-voltage measurements. *J. Appl. Phys.*, 71:318–325, 1992.
- [61] A. Lops, V. Spagnolo, and G. Scamarcio. Thermal modeling of GaInAs/AlInAs quantum cascade lasers. *J. Appl. Phys.*, 100:043109, 2006.
- [62] Technical data sheet for Epo-Tek H20E-175, Epoxy Technology, Inc., 2011. URL <http://www.epotek.com>.
- [63] L. Werner, H.-W. Hübers, P. Meindl, R. Müller, H. Richter, and A. Steiger. Towards traceable radiometry in the terahertz region. *Metrologia*, 46:S160–S164, 2009.
- [64] J. Carroll, J. Whiteaway, and D. Plumb. *Distributed feedback semiconductor lasers*. The institution of electrical engineers, London, 1998.
- [65] S. Kumar, C. W. I. Chan, Q. Hu, and J. L. Reno. A 1.8-THz quantum cascade laser operating significantly above the temperature of $\hbar\omega/k_B$. *Nature Phys.*, 7:166–171, 2011.
- [66] H. Richter, M. Greiner-Bär, S. G. Pavlov, A. D. Semenov, M. Wienold, L. Schrottke, M. Giehler, R. Hey, H. T. Grahn, and H.-W. Hübers. A compact, continuous-wave terahertz source based on a quantum-cascade laser and a miniature cryocooler. *Opt. Express*, 18:10177–10187, 2010.
- [67] G. Scalari, N. Hoyler, M. Giovannini, and J. Faist. Terahertz bound-to-continuum quantum-cascade lasers based on opticalphonon scattering extraction. *Appl. Phys. Lett.*, 86:181101, 2005.
- [68] S. Barbieri, J. Alton, H. E. Beere, J. Fowler, E. H. Linfield, and D. A. Ritchie. 2.9 THz quantum cascade lasers operating up to 70 K in continuous wave. *Appl. Phys. Lett.*, 85:1674, 2004.
- [69] L. Ajili, G. Scalari, J. Faist, H. Beere, E. Linfield, D. Ritchie, and G. Davies. High power quantum cascade lasers operating at $\lambda = 87 \mu\text{m}$ and $130 \mu\text{m}$. *Appl. Phys. Lett.*, 85:3986–3988, 2004.

Bibliography

- [70] S. Kumar. Recent progress in terahertz quantum cascade lasers. *IEEE J. Sel. Topics Quantum Electron.*, 17:38–47, 2011.
- [71] H. Page, C. Becker, A. Robertson, G. Glastre, V. Ortiz, and C. Sirtori. 300 K operation of a GaAs-based quantum-cascade laser at $\lambda = 9 \mu\text{m}$. *Appl. Phys. Lett.*, 78:3529–3531, 2001.
- [72] C. Becker, C. Sirtori, H. Page, G. Glastre, V. Ortiz, X. Marcadet, M. Stellmacher, and J. Nagle. AlAs/GaAs quantum cascade lasers based on large direct conduction band discontinuity. *Appl. Phys. Lett.*, 77:463–465, 2000.
- [73] A. G. G. M. Tielens and D. Hollenbach. Photodissociation regions. I. Basic model. *Astrophys. J.*, 291:722–746, 1985.
- [74] L. R. Zink, K. M. Evenson, F. Matsuhima, T. Nelis, and R. L. Robinson. Atomic oxygen fine-structure splitting with tunable far-infrared spectroscopy. *Astrophys. J.*, 371:L85–L86, 1991.
- [75] H. Callebaut, S. Kumar, B. S. Williams, Q. Hu, and J. L. Reno. Importance of electron-impurity scattering for electron transport in terahertz quantum-cascade lasers. *Appl. Phys. Lett.*, 84:645–647, 2004.
- [76] H. C. Liu, M. Wächter, D. Ban, Z. R. Wasilewski, M. Buchanan, G. C. Aers, J. C. Cao, S. L. Feng, B. S. Williams, and Q. Hu. Effect of doping concentration on the performance of terahertz quantum-cascade lasers. *Appl. Phys. Lett.*, 87:141102, 2005.
- [77] L. Ajili, G. Scalari, M. Giovannini, N. Hoyler, and J. Faist. Doping in quantum cascade lasers. II. GaAs/Al_{0.15}Ga_{0.85}As terahertz devices. *J. Appl. Phys.*, 100:043102, 2006.
- [78] A. Benz, G. Fasching, A. M. Andrews, M. Martl, K. Unterrainer, T. Roch, W. Schrenk, S. Golka, and G. Strasser. Influence of doping on the performance of terahertz quantum-cascade lasers. *Appl. Phys. Lett.*, 90:101107, 2007.
- [79] G. Scalari, R. Terazzi, M. Giovannini, N. Hoyler, and J. Faist. Population inversion by resonant tunneling in quantum wells. *Appl. Phys. Lett.*, 91:032103, 2007.
- [80] H. Callebaut, S. Kumar, B. S. Williams, Qing Hu, and J. L. Reno. Analysis of transport properties of terahertz quantum cascade lasers. *Appl. Phys. Lett.*, 83:207–209, 2003.
- [81] B. Jenichen, R. Hey, M. Wassermeier, and K. Ploog. Investigation of the interface roughness of GaAs single quantum wells by X-ray diffractometry, reflectivity and diffuse scattering. *Il Nuovo Cimento*, 19D:429–437, 1997.
- [82] J. Faist, C. Gmachl, F. Capasso, C. Sirtori, D. L. Sivco, J. N. Baillargeon, and A. Y. Cho. Distributed feedback quantum cascade lasers. *Appl. Phys. Lett.*, 70:2670–2672, 1997.

- [83] G. P. Luo, C. Peng, H. Q. Le, S. S. Pei, W.-Y. Hwang, B. Ishaug, J. Um, J. N. Baillargeon, and C.-H. Lin. Grating-tuned external-cavity quantum-cascade semiconductor lasers. *Appl. Phys. Lett.*, 78:2834–2636, 2001.
- [84] J. Xu, J. M. Hensley, D. B. Fenner, R. P. Green, L. Mahler, A. Tredicucci, M. G. Allen, F. Beltram, H. E. Beere, and D. A. Ritchie. Tunable terahertz quantum cascade lasers with an external cavity. *Appl. Phys. Lett.*, 91:121104, 2007.
- [85] L. Mahler, A. Tredicucci, R. Köhler, F. Beltram, H. E. Beere, E. H. Linfield, and D. A. Ritchie. High-performance operation of single-mode terahertz quantum cascade lasers with metallic gratings. *Appl. Phys. Lett.*, 87:181101, 2005.
- [86] M. I. Amanti, M. Fischer, G. Scalari, M. Beck, and J. Faist. Low-divergence single-mode terahertz quantum cascade laser. *Nature Photon.*, 3:586–590, 2009.
- [87] L. Mahler, A. Tredicucci, F. Beltram, C. Walther, J. Faist, H. E. Beere, and D. A. Ritchie. High-power surface emission from terahertz distributed feedback lasers with a dual-slit unit cell. *Appl. Phys. Lett.*, 96:191109, 2010.
- [88] D. G. Allen, T. Hargett, J. L. Reno, A. A. Zinn, and M. C. Wanke. Index tuning for precise frequency selection of terahertz quantum cascade lasers. *Photon. Technol. Lett.*, 23:30–32, 2011.
- [89] S. Golka, C. Pflügl, W. Schrenk, and G. Strasser. Quantum cascade lasers with lateral double-sided distributed feedback grating. *Appl. Phys. Lett.*, 86:111103, 2005.
- [90] B. S. Williams, S. Kumar, Q. Hu, and J. L. Reno. Distributed-feedback terahertz quantum-cascade lasers with laterally corrugated metal waveguides. *Opt. Lett.*, 30:2909–2911, 2005.
- [91] H. Kogelnik and C. V. Shank. Coupled-wave theory of distributed feedback lasers. *J. Appl. Phys.*, 43:2327–2335, 1972.
- [92] L. A. Coldren and S. W. Corzine. *Diode lasers and photonic integrated circuits*. Wiley, New York, 1995.
- [93] A. Laakso, M. Dumitrescu, J. Viheriälä, J. Karinen, M. Suominen, and M. Pessa. Optical modeling of laterally-corrugated ridge-waveguide gratings. *Opt. Quant. Electron.*, 40:907–920, 2008.
- [94] J. Pomplun, S. Burger, L. Zschiedrich, and F. Schmidt. Adaptive finite element method for simulation of optical nano structures. *Phys. Stat. Sol. (b)*, 10:3419–3434, 2007.
- [95] P. Berini. Plasmon-polariton waves guided by thin lossy metal films of finite width: Bound modes of symmetric structures. *Phys. Rev. B*, 61:10484–10503, 2000.
- [96] A. Wacker. Semiconductor superlattices: a model system for nonlinear transport. *Phys. Rep.*, 357:1–111, 2002.

Bibliography

- [97] L. L. Bonilla and H. T. Grahn. Non-linear dynamics of semiconductor superlattices. *Rep. Prog. Phys.*, 68:577–683, 2005.
- [98] H. Xu and S. W. Teitworth. Dependence of electric field domain relocation dynamics on contact conductivity in semiconductor superlattices. *Phys. Rev. B*, 76:235302, 2007.
- [99] S. L. Lu, L. Schrottke, S. W. Teitworth, R. Hey, and H. T. Grahn. Formation of electric-field domains in GaAs/Al_xGa_{1-x}As quantum cascade laser structures. *Phys. Rev. B*, 73:033311, 2006.
- [100] J. Ulrich, G. Strasser, and K. Unterrainer. Terahertz quantum cascade emitters based on AlAs/GaAs. *Physica E*, 13:900–903, 2002.
- [101] L. Esaki and R. Tsu. Superlattice and negative differential conductivity in semiconductors. *IBM J. Res. Dev.*, 14:61, 1970.
- [102] J. B. Gunn. Microwave oscillations of current in III-V semiconductors. *Solid State Commun.*, 1:88–91, 1963.
- [103] *Series 2600A system SourceMeter instruments reference manual*. Keithley Instruments, Inc., Cleveland, Ohio, 2008.
- [104] R. Scheuerer, E. Schomburg, K. F. Renk, A. Wacker, and E. Schöll. Feasibility of a semiconductor superlattice oscillator based on quenched domains for the generation of submillimeter waves. *Appl. Phys. Lett.*, 81:1515, 2002.
- [105] H. Eisele, I. Farrer, E. H. Linfield, and D. A. Ritchie. High-performance millimeter-wave superlattice electronic devices. *Appl. Phys. Lett.*, 93:182105, 2008.
- [106] H. Eisele, S. P. Khanna, and E. H. Linfield. Superlattice electronic devices as high-performance oscillators between 60-220 GHz. *Appl. Phys. Lett.*, 96:072101, 2010.

List of Figures

2.1	Dependence of the critical thickness on the Al content	4
2.2	Far-infrared transmittance spectra of semi-insulating GaAs	11
2.3	Absorption coefficient of GaAs for different doping densities	12
2.4	Dielectric function and refractive index for highly doped GaAs	12
2.5	Schematic illustration of single-plasmon and metal-metal THz waveguide . .	14
2.6	Intensity distribution in a single-plasmon waveguide	16
2.7	Frequency dependence of characterizing waveguide parameters	17
3.1	$\gamma_E(E)$ relation used for the rate equation-based transport simulations . . .	22
3.2	Variation of the relative period length across different wafers	23
3.3	25
3.4	Schematic diagram of the setup for power measurements	26
4.1	Result of a bandstructure calculation for sample M4-2243	30
4.2	Calculated gain characteristics and current density-field relation	31
4.3	Light-current-voltage characteristics for sample M4-2243	31
4.4	Lasing spectra for sample M4-2243	32
4.5	Temperature dependence of the threshold current density	33
5.1	Result of bandstructure calculations for samples A and B	39
5.2	Lasing spectra of samples A and B	40
5.3	Temperature dependence of threshold current and L - I - V characteristics . .	41
5.4	Central frequency vs. operating voltage for various samples	43
6.1	Simulation results for the basic 4.7 THz design	46
6.2	Calculated doping dependence of gain	47
6.3	Pulsed L - I - V characteristics and lasing spectra of sample M4-2404	48
6.4	Temperature dependence of the threshold current density	49
6.5	Continuous-wave emission spectra of the modified sample m1	52
6.6	Calculated gain and measured lasing spectra for sample m8	54
6.7	Measured I - V characteristics for different locations on a wafer	55
6.8	Threshold current density for different locations on a wafer	56
6.9	Lasing spectra for different locations on a wafer	57
6.10	Frequency trend of the maximum operating temperature	58
7.1	Schematic diagram and SEM image of an IDFB grating	60
7.2	Results of finite-element simulations of the IDFB unit cell	64
7.3	Single-mode lasing characteristics of three IDFB QCLs	66
7.4	Multi-mode characteristics of an IDFB laser	67

List of Figures

7.5	Calculated threshold gain vs. frequency for IDFB cavities	68
7.6	Emission spectra of an IDFB laser around 4.75 THz	70
8.1	Change of the band structure below and above the onset of NDR	74
8.2	Calculated drift velocity-field characteristics	75
8.3	Lasing characteristics for current biasing in the presence of static EFDs . .	76
8.4	Lasing characteristics for voltage biasing in the presence of static EFDs . .	76
8.5	Calculated I - V characteristics and spatial carrier- and field distributions . .	78
8.6	Calculated L - V characteristics in the presence of static EFDs	80
8.7	L - I - V characteristics in the presence of current self-oscillations	82
8.8	Time-resolved laser signal in the presence of current self-oscillations	83
8.9	Simulated I - V characteristics exhibiting current self-oscillations	84
8.10	Carrier and electric field distribution in the case of self-oscillations	85

List of Tables

2.1	Parameters used for the dielectric function of GaAs and $\text{Al}_x\text{Ga}_{1-x}\text{As}$	10
2.2	Vertical scheme of single-plasmon waveguide as used for simulations	15
3.1	Calculated far-field divergence angles for the fundamental waveguide mode	27
4.1	Characterization results for a doping series	34
6.1	Sample properties for the basic 4.7 THz active-region design	48
6.2	Barrier modifications and operating parameters of samples m1 to m3	51
6.3	Injector modifications and operating parameters of samples m4 to m7	53
6.4	Basic operating parameters for samples m8 to m10	54
7.1	Eigenfrequencies and coupling coefficients for different waveguide modes . .	63

Publications

M. Wienold, L. Schrottke, M. Giehler, R. Hey, W. Anders, and H. T. Grahn. *Low-voltage terahertz quantum-cascade lasers based on LO-phonon-assisted interminiband transitions*, Electron. Lett. **45**, 1030 (2009)

L. Schrottke, M. Giehler, M. Wienold, R. Hey, and H. T. Grahn. *Simulation of the interplay between stimulated emission and carrier distribution in quantum-cascade lasers*, Physica E **42**, 2632 (2010)

L. Schrottke, M. Giehler, M. Wienold, R. Hey, and H. T. Grahn. *Compact model for the efficient simulation of the optical gain and transport properties in THz quantum-cascade lasers*, Semicond. Sci. Technol. **25**, 045025 (2010)

M. Wienold, L. Schrottke, M. Giehler, R. Hey, W. Anders, and H. T. Grahn. *Low-threshold terahertz quantum-cascade lasers based on GaAs/Al_{0.25}Ga_{0.75}As heterostructures*, Appl. Phys. Lett. **97**, 071113 (2010)

L. Schrottke, M. Wienold, M. Giehler, R. Hey, and H. T. Grahn. *Analysis of the slope efficiency for terahertz quantum-cascade lasers*, J. Appl. Phys. **108**, 103108 (2010)

H. Richter, M. Greiner-Bär, S. G. Pavlov, A. D. Semenov, M. Wienold, L. Schrottke, M. Giehler, R. Hey, H. T. Grahn, and H. W. Hübers. *A compact, continuous-wave terahertz source based on a quantum-cascade laser and a miniature cryocooler*, Opt. Express **18**, 10177 (2010)

M. Wienold, L. Schrottke, M. Giehler, R. Hey, and H. T. Grahn. *Nonlinear transport in quantum-cascade lasers: The role of electric-field domain formation for the laser characteristics*, J. Appl. Phys. **109**, 073112 (2011)

R. Eichholz, H. Richter, S. G. Pavlov, M. Wienold, L. Schrottke, R. Hey, H. T. Grahn, and H. W. Hübers. *Multi-channel terahertz grating spectrometer with quantum-cascade laser and microbolometer array*, Appl. Phys. Lett **99**, 141112 (2011)

R. Sharma, L. Schrottke, M. Wienold, R. Hey, and H. T. Grahn. *Effect of stimulated emission on the transport characteristics of terahertz quantum-cascade lasers*, Appl. Phys. Lett. **99**, 151116 (2011)

Publications

M. Giehler, M. Wienold, L. Schrottke, R. Hey, H. T. Grahn, S. G. Pavlov, H.-W. Hübers, S. Winnerl, and H. Schneider. *Mid-infrared pump-related electric-field domains in GaAs/(Al,Ga)As quantum-cascade structures for terahertz lasing without population inversion*, J. Appl. Phys. **110**, 103104 (2011)

M. Wienold, A. Tahraoui, L. Schrottke, R. Sharma, X. Lü, K. Biermann, R. Hey, and H. T. Grahn. *Lateral distributed-feedback gratings for single-mode, high-power terahertz quantum-cascade lasers*, submitted to Opt. Express

Conference presentations

M. Wienold, L. Schrottke, M. Giehler, R. Hey, and H. T. Grahn. *Development of low-threshold terahertz quantum-cascade lasers with high output power*, Laser Optics Berlin (LOB), Berlin, Germany, Mar. 2010

M. Wienold, L. Schrottke, M. Giehler, R. Hey, and H. T. Grahn. *Influence of barrier composition, doping density, and layer thickness variations on the performance of THz quantum-cascade lasers*, Heraeus seminar "THz radiation: generation, detection and applications", Bad Honnef, Germany, Apr. 2010

M. Wienold, M. Giehler, L. Schrottke, R. Hey, S. Winnerl, H. Schneider, S. G. Pavlov, and H. T. Grahn. *Investigation of MIR-pumped quantum-cascade structures as emitters of THz radiation*, Workshop "Terahertz spectroscopy and its high-field applications", Rossendorf, Germany, Jun. 2010

M. Wienold, L. Schrottke, M. Giehler, R. Hey, A. D. Semenov, H. Richter, S. G. Pavlov, H.-W. Hübers, and H. T. Grahn. *Electric-field domains in terahertz quantum-cascade lasers*, Intersubband transitions in quantum wells (ITQW), Badesi, Italy, Sep. 2011

Acknowledgement

My deep gratitude goes to all the people, who supported me during this thesis. In the first place, I would like to thank Prof. H. Riechert and Prof. H. T. Grahn, who gave me the opportunity to work at the *Paul-Drude-Institut* in Berlin in an inspiring atmosphere. I am grateful to Prof. H. T. Grahn for supervising the thesis in practice. My thanks go to L. Schrottke for the good and intensive collaboration and, in particular, for performing the active-region simulations. The active-region designs are based in large part on his ideas and numerical simulations. I appreciated the collaboration with M. Giehler, whom I thank for sharing his knowledge on infrared spectroscopy as well as for many fierce and fruitful discussions. I am in debt to R. Hey, K. Biermann, and M. HÖricke for the sample growth and to R. Hey also for performing x-ray and C - V measurements. My thanks go to W. Anders and A. Tahraoui for sample processing, and to A. Riedel for her help with wire-bonding and sample preparation. I thank H. Richter, S. G. Pavlov, A. D. Semenov, and H.-W. Hübers for sharing their experience and experimental equipment, such as the fast hot-electron bolometer. I am grateful to H. Wenzel for his theoretical support with distributed-feedback lasers, in particular for providing the numerical tool for solving the coupled-mode equations. I acknowledge the assistance of R. Sharma and X. Lü in the infrared spectroscopy lab, which has been a big relieve during the time of writing. I thank P. Kleinert for theoretical support, K. J. Friedland for support with C - V and Hall measurements, and Y. Takagaki and A.-K. Bluhm for their assistance with scanning electron microscopy. I'm grateful to D. Dormeyer and S. Räther for organizing any article and book, which I requested during my time at the PDI. I thank J. Pomplun, and S. Burger from *JCMwave* for their support with the *JCMsuite* software. For proofreading, my thanks go to Prof. H. T. Grahn, L. Schrottke, K. Biermann, H. Wenzel, R. Sharma, and Prof. L. L. Bonilla.

Not all of the work of the recent years has become part of this thesis. My thanks go to many people, who supported me during my time at the *Paul-Drude-Institut* in the one or other way: D. Steffen and H. Kiedrowski for crystal preparation, W. Seidel for fabrication of the lithographic masks, B. Drescher for sputtering and e-beam evaporation, and G. Paris for help with electronic problems. I am grateful to the mechanical workshop team of T. Ferber, F. Henschke, J. Pfeiffer, M. Sieg, and J. Weiss for fabrication of the QCL submounts and for various sample holders and adapters.

At the end, I would like to thank my wife for her support and her patience during all the time.

Selbständigkeitserklärung

Ich erkläre, dass ich die vorliegende Arbeit selbständig und nur unter Verwendung der angegebenen Literatur und Hilfsmittel angefertigt habe.

Berlin, den 29.12.2011

Martin Wienold